DISTRIBUTED-PARAMETER VIBRATION CONTROL OF A CANTILEVER BEAM USING A DISTRIBUTED-PARAMETER ACTUATOR

by

Thomas Lee Bailey

SUBMITTED TO THE DEPARTMENT OF
MECHANICAL ENGINEERING
IN PARTIAL FULFILLMENT OF THE REQUIREMENTS
FOR THE DEGREES OF

BACHELOR OF SCIENCE IN MECHANICAL ENGINEERING

and

MASTER OF SCIENCE IN MECHANICAL ENGINEERING

at the

MASSACHUSETTS INSTITUTE OF TECHNOLOGY

September 1984

Copyright © 1984 Massachusetts Institute of Technology

Signature of Author _____
Department of Mechanical Engineering
September, 1984

Certified by _____
James E. Hubbard, Jr.
Thesis Supervisor

Accepted by _____
Warren M. Rohsenow
Chairman, Department Thesis Committee

ARCHIVES
MASSACHUSETTS INSTITUTE
OF TECHNOLOGY

OCT 0 2 1984

LIBRARIES

Distributed-Parameter Vibration Control
of a Cantilever Beam using a
Distributed-Parameter Actuator

by

Thomas Lee Bailey

Submitted to the Department of Mechanical Engineering on September 7, 1984 in partial fulfillment of the requirements for the degrees of Bachelor of Science and Master of Science in Mechanical Engineering.

Abstract

An active vibration damper for a cantilever beam was designed using a distributed-parameter actuator and distributed-parameter control theory. The distributed-parameter actuator was a piezoelectric polymer, poly(vinylidene fluoride). Lyapunov's second method for distributed-parameter systems was used to design a control algorithm for the damper. If the angular velocity of the tip of the beam is known, all modes of the beam can be controlled simultaneously. However, only the linear acceleration at the tip was measured, so the remaining analysis and the testing was done on a single mode at a time, up to the third mode. A simulation algorithm was developed to predict the effect of the active damper on the free decay of a single mode of vibration. A parameter study for the first mode was performed using varying control voltage limits and passive damping values.

Testing of the active damper was performed on the free decay of the first mode and with continuous excitation of both the first and second modes of the cantilever beam. A linear, constant-gain controller and a nonlinear constant-amplitude controller were compared in the free decay tests. The baseline damping of the first mode was η=0.003 for large amplitude vibrations ($\pm$2 cm tip displacement) decreasing to η=0.001 for small vibrations ($\pm$0.5 mm tip displacement). The constant-gain controller provided more than a factor of 2 increase in the modal damping with a feedback voltage limit of V_{max}=200 V rms. With the same voltage limit, the constant-amplitude controller achieved the same damping as the constant gain controller for large vibrations, but increased the damping by a factor of 40 to at least η=0.040 for small vibration levels.

For the continuous excitation testing, the clamping fixture for the beam was mounted on a shaker. The beam was excited by bandlimited random noise that was

centered on the resonant frequency of interest so that only one mode of vibration would be present. Only the constant-gain controller was implemented for the continuous excitation tests. For the first mode, with the highest rms level of base acceleration and a control voltage limit of V_{max}=130 V rms, the loss factor was increased from a baseline damping of η_p=0.0040 to η_{eff}=0.0054. With the lowest rms level of base acceleration and a control voltage limit of V_{max}=100 V rms, the damping was increased from η_p=0.0026 to η_{eff}=0.020 . This corresponds to a 15 db reduction in the magnitude of the resonance. For the second mode, with the highest rms base acceleration and V_{max}=25 V rms, the damping was increased from η_p=0.0016 to η_{eff}=0.0023 . For the lowest rms base acceleration and V_{max}=30 V rms, the damping increased from η_p=0.0014 to η_{eff}=0.0039 . This is a 10 db reduction in the magnitude of the resonance.

Thesis Supervisor: James E. Hubbard, Jr.
Title: Assistant Professor of Mechanical Engineering

Acknowledgements

I would like to thank my parents, Phillip and Darlene, for their unending physical and spiritual support. I would especially like to thank them for helping me to develop a very inquisitive nature and for passing along a good deal of 'common sense'. Little did they know that taking the time to deal with the multitude of questions from a young boy would someday lead to a degree from MIT.

I would also like to thank my wife, Beth. Her love and support have never waivered during the past three years, even through the writing of this thesis. By providing a calm oasis away from the problems of school and research, she has helped to make MIT a much more enjoyable experience. I only hope that I can repay her for all the late evenings and weekends (weeks) of neglect.

Thanks to the others that have helped to make my stay here more enjoyable: Mr. Excitement and the other members of the Old Farts Club, Steve, Jon, Andrei, and all the rest. Where would we be without friends?

Thanks to Shawn Burke for his technical help and analytical insight that often seemed to come at the most opportune moments.

I must also thank Jim Hubbard for his guidance and support throughout the past year. I greatly appreciate his faith in me and his friendship. My only regret from this thesis is that I didn't meet Jim sooner in my academic career.

Table of Contents

List of Figures

List of Tables

Chapter 1
Introduction

1.1 Background

Satellites and other large spacecraft structures are generally lightly damped due to low structural damping in the materials used and the lack of other forms of damping, such as air drag. In large structures, these vibrations have long decay times which can lead to fatigue, instability, or other problems with the operation of the structure [1, 3]. Flexible structures such as these are distributed-parameter systems having a theoretically infinite number of vibrational modes. Current design practice often is to model the system with a finite number of modes and to design a control system using lumped-parameter control theory. 'Truncating' the model may lead to performance tradeoffs when designing a control system for distributed-parameter systems [4].

Using distributed-parameter control theory to design the control system will avoid these tradeoffs by including all the vibrational modes in the design process and gives the potential for controlling all modes of vibration. There exists a wealth of distributed-parameter control theory in the literature, including the extension of many aspects of lumped-parameter control theory to distributed parameter systems. References [5] through [14] are a small sampling of the work being done. However, there are relatively few applications in the literature, especially for flexible mechanical systems. One reason may be the difficulty of using distributed-parameter control theory with spatially discrete, or lumped-parameter, sensors and actuators which introduce spatial non-linearities into the system. Distributed-parameter sensors and actuators would significantly ease the use of distributed-parameter control theory for flexible structures.

1.2 Objective of Research

The goal of this study is to design and evaluate an active vibration damper for distributed-parameter systems using a distributed-parameter actuator and to show some advantages of distributed-parameter control theory. The distributed-parameter actuator is a piezoelectric polymer, poly(vinylidene fluoride), or PVF_2. At the Charles Stark Draper Laboratory, a scale model of a flexible satellite has been designed and built as a test structure for active vibration control schemes [1, 3]. This test structure consists of a hub mounted on an air bearing table with four perpendicular arms extending radially from the hub. The arms rotate in a horizontal plane and are flexible laterally while being very stiff vertically. The active damper developed in this study will eventually be tested using the Draper structure. The damper is to be applied to the flexible arms. This thesis reports the development and preliminary testing of the active damper for the Draper test structure.

For the development work, an arm of the test structure was modeled as a cantilever beam with a tip mass and tip inertia. A smaller dynamically scaled model of one of the arms (including the use of a tip accelerometer) was used for the preliminary testing. Chapter 2 presents an overview of the system. The distributed-parameter actuator (PVF_2), the Draper test structure and the dynamic scaling of the arm, and the active damper configuration are discussed. The theoretical analysis is presented in Chapter 3. The modeling of the active damper and the derivation of a distributed-parameter control algorithm are presented. Also a simulation algorithm is developed and a parameter study is performed. Chapter 4 presents the experimental work performed for the preliminary testing of the active damper. The construction of the test fixtures and the cantilever beam is discussed. The active damper was tested with the beam in a stationary fixture and in a vibrating fixture. The results from these tests are also presented and discussed. The final chapter summarizes the results of this study and presents some recommendations for further research.

Chapter 2
Overview of the System

2.1 The Distributed Actuator

The active element being used in this damper is a piezoelectric polymer film, poly(vinylidene fluoride), or PVF_2. PVF_2 is a polymer that can be polarized, or made piezoelectrically active, by exposing it to intense electrical fields. In its non-polarized form, PVF_2 is used as an electrical insulator, a capacitor dielectric material, and as a chemically inert coating, among many other uses. In its polarized form, PVF_2 is essentially a tough, flexible piezoelectric crystal. Polarized PVF_2 has been used in many applications ranging from ventilation fans [15, 16] to electroacoustic transducers (speaker and microphone elements) [17] to ultrasonic transducers for medical use [18]. More information on PVF_2, other piezoelectric polymers, and their applications can be found in References [19] through [25].

A sketch of a piece of PVF_2 film is shown in Figure 2-1. A layer of nickel or aluminum is generally deposited on each face to conduct the applied field or voltage, V(x), along the surface of the PVF_2.

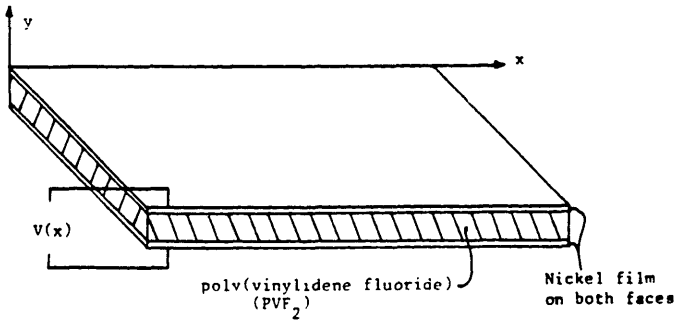

Figure 2-1: Coordinate system for the PVF_2.

For uniaxially polarized PVF_2, a voltage or field applied across its faces (y-direction) results in a longitudinal (x-direction) strain. This is the d_{31} component of the piezoelectric activity. (Biaxially polarized PVF_2 would strain in both the x- and z-directions.) The strain occurs over the entire area of the PVF_2 making it a distributed-parameter actuator. Note that if the voltage, V(x), is varied spatially, the strain will also vary spatially. This allows the added possibility of varying the control spatially as well as with time. The sign convention used in this study is that a positive voltage, as shown in Figure 2-1, results in a positive longitudinal strain.

The PVF_2 used in this study was obtained from the Pennwalt Corporation, King of Prussia, PA. It is commercially available as a thin polymeric film with a coating of nickel or aluminum on its faces. Table 2-I gives some typical properties for Pennwalt's Kynar^{TM} brand PVF_2 film [2].

2.2 The Flexible Structure

At the Charles Stark Draper Laboratory, a scale model of a flexible satellite has been designed and built as a test structure for active vibration control schemes [1, 3]. A sketch of the test structure is shown in Figure 2-2. This test structure consists of a hub mounted on an air bearing table with four perpendicular arms extending radially from the hub. The arms rotate in a horizontal plane and are flexible laterally while being very stiff vertically. This minimizes the effect of gravity on the motion of the structure. The arms are 1.2 m long and have either thrusters or weights for tip mass. The thrusters are mounted on one pair of opposing arms and are used to control the vibrations of the structure as well as perform attitude manuevers. Accelerometers at the tip of the arms are used to monitor the vibrations of the structure during and after the attitude manuevers. The damper developed in this study is to be applied to the flexible arms of the test structure to demonstrate the use of a distributed-parameter actuator for active control of a distributed-parameter system.

For the development work, an arm of the test structure was modeled as a cantilevered Bernoulli-Euler beam with both a tip mass and tip inertia (rotary inertia). A sketch of the top view of the cantilever beam model is shown in Figure 2-3. The nomenclature is as follows:

Portions of the text
on the following page(s)
are not legible in the
original.

Table 2-I: Typical PVF_2 film properties [2].

PROPERTY		VALUE	UNITS
Thickness		6-125	μm
Surface Conductivity of Metallized Film	Al	1-4	$\Omega\square^{-1}$
	Ni	10-25	
Static Piezoelectric Strain Constant	d_{31}	20-25	pCN^{-1} (pmV^{-1})
	d_{33}*	20-22	
Static Voltage Output Coefficient	g_{31}	0.230	VmN^{-1}
	g_{33}	0.210	
Electromechanical Coupling Factor	k_{31}	9-15	% at 100 Hz
Pyroelectric Coefficient	p	23-27	$\mu Cm^{-2}{}^{\circ}K^{-1}$
Shrinkage in Machine Direction	60°C	2	% after annealing 100 hrs.
	80°C	4	
Relative Dielectric Permittivity	$\varepsilon/\varepsilon_0$	12 ± 1	at 1000 Hz
Dielectric Loss Factor	tan δ	0.015-0.02	at 1000 Hz
Volume Resistivity	ρ	$10^{}$	Ωm
Tensile Strength at Yield	MD**	–	$10^{6}Nm^{-2}$
	TD**	40-110	
Tensile Strength at Break	MD	160-330	$10^{6}Nm^{-2}$
	TD	30-55	
Elongation at Break	MD	25-40	%
	TD	380-430	
Young's Modulus of Elasticity = Elastic Stiffness = $c^{}$	MD	1.5-3	$10^{9}Nm^{-2}$
	TD	1.1-2.4	
Melting Point		165-180	°C
Flammability, LOI		44	$\%O_2$
Thermal Conductivity		0.13	$Wm^{-1}{}^{\circ}K^{-1}$
Specific Heat		2.5	$MJm^{-3}{}^{\circ}K^{-1}$
Density		1.8	g/cm^{3}
Thermal Expansion Coefficient		1-4	$10^{-5}{}^{\circ}K^{-1}$
Sound Velocity***		1.5-2.2	kms^{-1}

*measurements were made in hydraulic press (e_{33}/ε_0) **MD = Machine Direction (1) and TD = Transverse Direction to film orientation (2)
***longitudinal and thickness modes

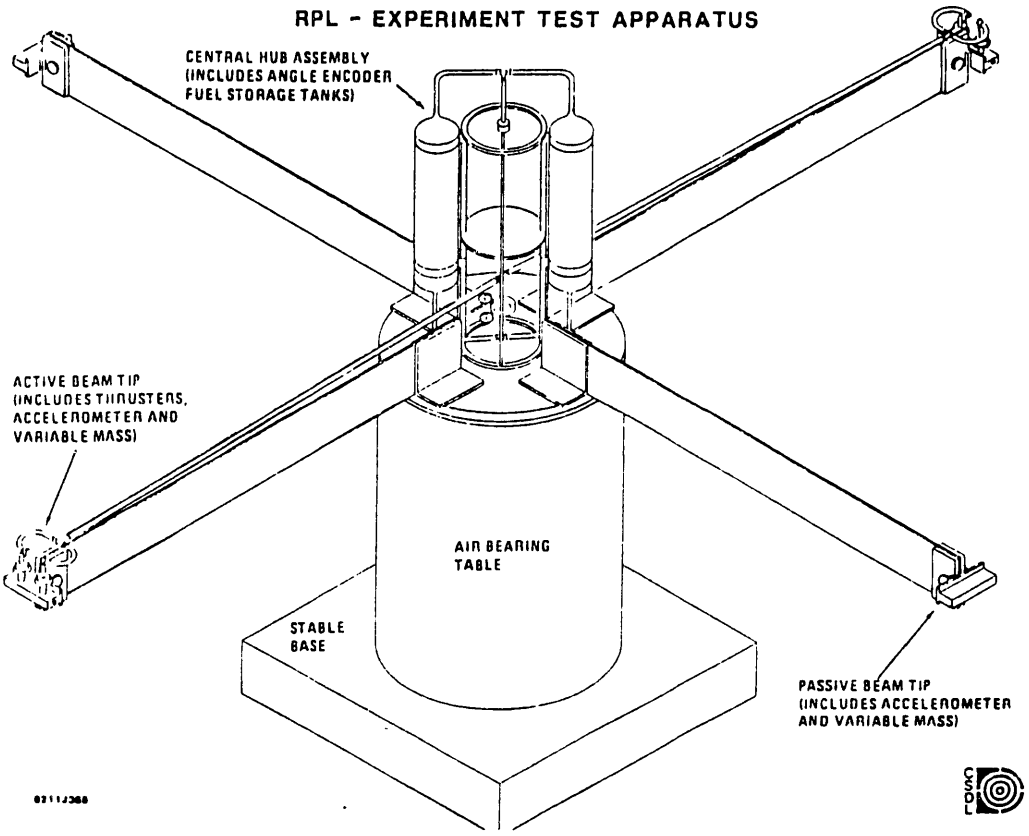

Figure 2-2: Flexible test structure at the Charles Stark Draper Laboratory [1].

- ρ is the density (mass per volume) of the beam
- E is the Young's modulus
- I is the area moment of inertia of the cross-section about the neutral axis of the beam
- l is the flexible length of the beam (x-direction)
- h is the thickness of the beam (y-direction)
- b is the depth of the beam (z-direction)
- M_t is the tip mass, and
- I_t is the tip inertia taken about the z-axis at the end of the beam.

Note that the end of the beam is not necessarily the center of gravity of the tip mass. This study will only look at w(x,t), the transverse motion of the beam. The first step in the development of the damper was to dyamically scale an arm of the Draper structure to a more manageable size using the same techniques as Kelly used to design the structure

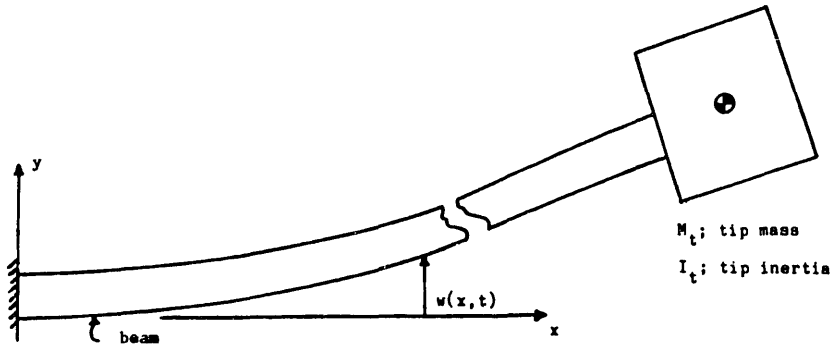

Figure 2-3: Cantilever beam model of an arm of the Draper structure.

originally [1, 3]. The scale model would also use an accelerometer at the tip of the beam to monitor the vibrations. The procedure used to scale the arm is given in Appendix C. The basic idea is to determine the dimensionless parameters that are used to describe the motion of the structure and then choose the physical parameters of the model so that the dimensionless parameters are preserved [26]. There are many possible combinations of physical parameters that will satisfy this criteria so some criteria other than just dynamic scaling must be used to chose a final design.

Other considerations in choosing the final design parameters for the scaled beam were:

1. The model size should be chosen so that the PVF_2 film thickness would not be excessive when it is scaled and applied to the Draper test structure,

2. The scaled tip mass must be large enough to allow an accelerometer to be used as part of the tip mass, and

3. The beam should be easy to make and not have tight tolerances on the dimensions that are determined during construction.

The final design dimensions for the scaled beam are listed in Table 2-II along with the corresponding dimensions for an arm of the Draper structure. The beam material was chosen because it was found that steel feeler gauge stock was readily available in a wide range of

Table 2-II: Comparison of final design parameters for the scaled beam vs. the Draper structure.

	Draper structure [1]	Scaled model
material	Al	steel
modulus, E (Nm^{-2})	$76x10^9$	$210x10^9$
density, ρ (kgm^{-3})	2840	7800
length, l (m)	1.22	0.146
thickness, h (mm)	3.18	0.381
depth, b (cm)	15.2	1.27
tip mass, M_t (kg)	2.04	$6.73x10^{-3}$
tip inertia, I_t (kgm^2)	$1.1x10^{-2}$	$5.0x10^{-7}$

thicknesses, 1.27 cm depth (width), and up to 30 cm in length. Since the thickness of feeler gauge stock is held to a relatively tight dimensional tolerance, the most critical dimension of the scaled beam is already controlled. A thickness of 0.381 mm (0.015") was chosen. For this beam thickness dynamic scaling calls for a flexible length of 14.6 cm (5.76") and a tip mass of 6.73 g, more than adequate to include a 2 g accelerometer as part of the tip mass. Section 4.1 will discuss the actual construction of the scaled beam and the clamping fixtures.

2.3 The Active Damper Configuration

The simplest possible damper configuration was used for this study; a layer of PVF_2 bonded to one side of the cantilver beam. Figure 2-4 shows a top view of the resulting composite beam. The PVF_2 is oriented as shown in Figure 2-1 so that a positive voltage across the film leads to a positive piezoelectric strain in the x-direction. It will be shown in Section 3.1 that this gives rise to a spatially distributed torque along the length of the beam. The resulting behavior is similar to that of bimetallic springs which coil and uncoil due to

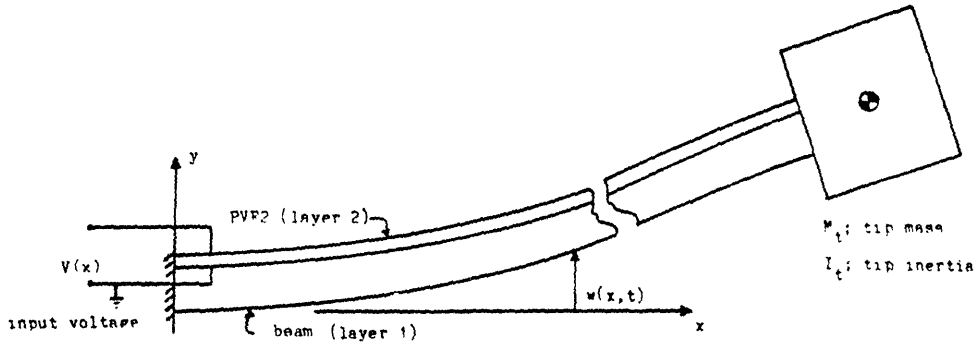

Figure 2-4: Active damper configuration.

differential thermal expansion as the temperature changes. The basic understanding gained from this simple damper configuration can easily be applied to more complicated damper configurations such as PVF_2 on both on both sides of the beam and/or multi-layer dampers that may include viscoelastic materials for added passive damping.

Chapter 3
Theoretical Analysis

This chapter describes the theoretical analysis performed to provide insight to the physical behaviour of the active damper. Section 3.1 describes the modeling of the active damper and the derivation and non-dimensionalization of the equations of motion. Section 3.2 presents the derivation of a distributed-parameter control law and Section 3.3 presents two additional control laws. Section 3.4 develops a simulation algorithm to predict the effectiveness of the active damper. Section 3.5 presents the results of a parameter study that was performed using the simulation algorithm. After the equations of motion have been non-dimensionalized in Section 3.1, the remaining analysis in this chapter is performed using dimensionless variables, unless otherwise stated. The results of the parameter study are presented in dimensionless form, although some representative plots also have dimensional axes that correspond to the scaled beam.

3.1 Modeling the Active Damper

The configuration of the active damper is shown in Figure 3-1. This is essentially a two layer cantilever beam. A subscript $(\cdot)_1$ refers to the original cantilever beam while a subscript $(\cdot)_2$ refers to the PVF_2 layer. Only transverse vibrations of the beam, w(x,t), will be analyzed. The full equations of motion are derived in Appendix A. The derivation presented here is a summary and focuses on the effect of a voltage applied to the PVF_2.

The effect of a voltage, V(x), applied an unbonded piece of PVF_2 is to cause a strain, ϵ_p, in the PVF_2 which is given by

$$\epsilon_p(x,t) = V(x,t) \cdot \frac{d_{31}}{h_2} \tag{3.1}$$

where d_{31} is the appropriate static piezoelectric constant, h_2 is the thickness (y-direction) of the PVF_2 layer, and both are assumed to be uniform along the length of the PVF_2. The PVF_2 is assumed to be oriented so that a positive voltage yields a positive strain. When the PVF_2 is bonded to the cantilever beam, this would be the equivalent of introducing a

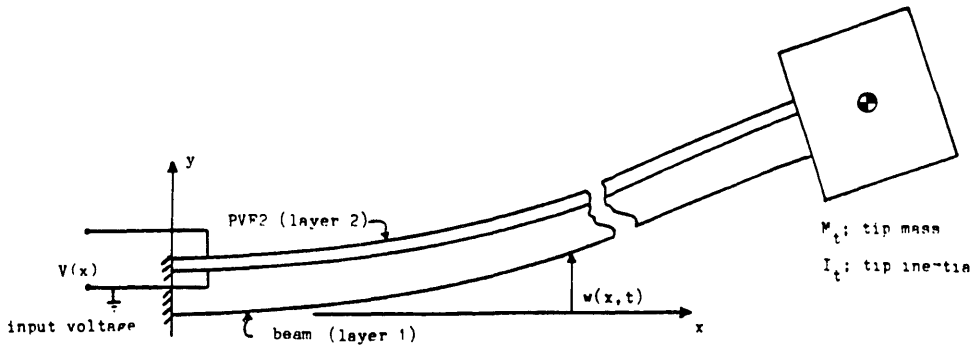

Figure 3-1: Active damper configuration.

negative prestrain, $-\epsilon_p$, in the PVF_2 layer. The prestrain is negative because the PVF_2 would strain ϵ_p if it weren't bonded to the beam and it would take a prestrain of $-\epsilon_p$ to move the PVF_2 back into place to be bonded. This is shown in Figure 3-2.

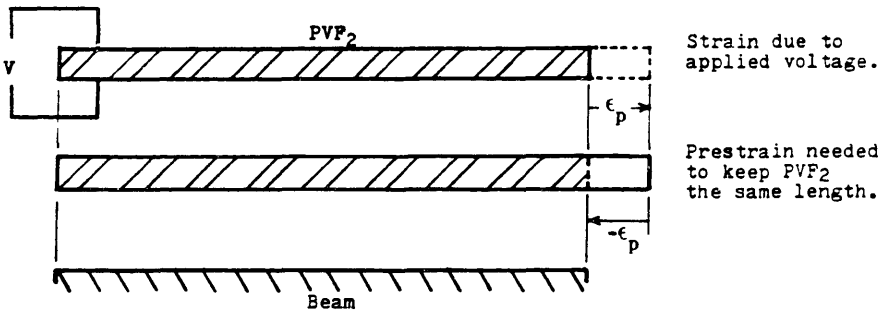

Figure 3-2: The applied voltage produces a negative prestrain.

This prestrain has two effects on the beam. One effect is a longitudinal strain, ϵ_l, to keep a force equillibrium in the axial (x) direction. The value of ϵ_l can be found by solving the force equillibrium and is given by

$$\epsilon_l(x,t) = \frac{E_2h_2}{E_1h_1+E_2h_2} \cdot \epsilon_p(x,t) \tag{3.2}$$

where E is the modulus of elasticity and h is the thickness of the layers, again assumed to be uniform along the length of the active damper. The result of the prestrain and the longitudinal strain is a net force in each beam layer due to the applied voltage.

The other effect of the prestrain is that the net force in each layer acts through the moment arm from the midplane of the layer to the neutral axis of the composite beam, producing a torque, T(x,t), given by

$$T(x,t) = E_1h_1b\epsilon_l\left(\frac{h_1}{2} - D\right) + E_2h_2b(\epsilon_l - \epsilon_p)\left(\frac{h_2}{2} + h_1 - D\right) \tag{3.3}$$

where b is the depth of the beam (assuming that $b_1=b_2$) and D is the location of the neutral axis of the composite beam, given by

$$D = \frac{E_1h_1^2 + E_2h_2^2 + 2h_1h_2E_2}{2(E_1h_1 + E_2h_2)} \quad . \tag{3.4}$$

Figure 3-3 shows a detail of the cross-section of the composite beam. Substituting for the neutral axis in Eqn. (3.3) and reducing yields

$$T(x,t) = -\frac{E_1h_1E_2h_2b}{(E_1h_1 + E_2h_2)}\left(\frac{h_1 + h_2}{2}\right)\epsilon_p \quad . \tag{3.5}$$

Notice that all the terms involving ϵ_l have been eliminated. This means that the torque depends only on the prestrain, not the longitudinal strain. Combining Eqns. (3.1) and (3.5) gives

$$\begin{aligned} T(x,t) &= -\frac{E_1h_1E_2b}{(E_1h_1 + E_2h_2)}\left(\frac{h_1 + h_2}{2}\right)d_{31} \cdot V(x,t) \\ &= c \cdot V(x,t) \end{aligned} \tag{3.6}$$

where c is a constant, for given beam materials and geometry, expressing the torque per volt. It is assumed that the material properties and geometry of the composite beam do not change along its length.

Combining Eqn. (3.6) with a conventional Bernoulli-Euler beam analysis yields the equations of motion for the transverse vibrations, w(x,t), for the composite beam. (See Appendix A for the derivation.) Assuming the longitudinal strain is negligible, the governing

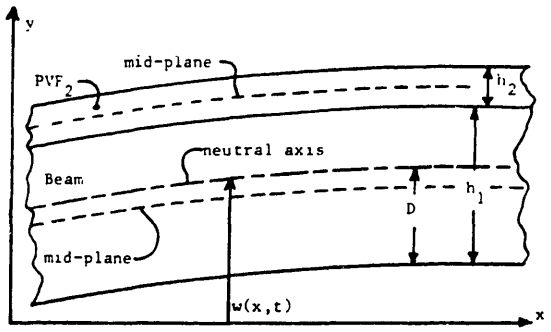

Figure 3-3: Detail of composite beam cross section.

equation is

$$EI\frac{\partial^4 w}{\partial x^4} + \rho A\frac{\partial^2 w}{\partial t^2} = c\cdot\frac{\partial^2 V(x,t)}{\partial x^2} \qquad \text{for x: } 0<x<l \tag{3.7}$$

with boundary conditions

$$\left.\begin{aligned} w = \frac{\partial w}{\partial x} &= 0 && \text{for } x=0 \\ EI\frac{\partial^2 w}{\partial x^2} &= -I_t\frac{\partial^3 w}{\partial t^2 \partial x} + c\cdot V(x,t) \\ EI\frac{\partial^3 w}{\partial x^3} &= M_t\frac{\partial^2 w}{\partial t^2} + c\cdot\frac{\partial V(x,t)}{\partial x} \end{aligned}\right\} \text{for } x=l \tag{3.8}$$

where $EI=E_1I_1+E_2I_2$, I is the area moment of inertia of the crosssection of the layer about the neutral axis, $\rho A=\rho_1A_1+\rho_2A_2$, ρ is the density of the layer, A is the cross-sectional area of the layer, l is the flexible length of the beam, and M_t and I_t are the tip mass and tip inertia, respectively.

These equations of motion can be non-dimensionalized to aid in scaling the analytical results from the scale model to the test structure and to provide insight into the important parameters of the system. The derivation in Appendix A suggests the following dimensionless variables.

$$x = \frac{x}{l} \quad ,$$

$$w = \frac{w}{l} \quad ,$$

$$t = t \cdot \sqrt{\frac{EI}{\rho A l^4}} \quad ,$$

$$V = V \cdot \frac{cl}{EI} \quad , \tag{3.9}$$

$$M_t = \frac{M_t}{\rho A l} \quad ,$$

$$I_t = \frac{I_t}{\rho A l^3} \quad .$$

Using these dimensionless variables in Eqns. (3.7) and (3.8) gives the dimensionless equations of motion, which are

$$\frac{\partial^4 w}{\partial x^4} + \frac{\partial^2 w}{\partial t^2} = \frac{\partial^2 V(x,t)}{\partial x^2} \qquad \text{for } x: \ 0<x<1 \tag{3.10}$$

with boundary conditions

$$\left.\begin{aligned} w &= \frac{\partial w}{\partial x} = 0 \qquad\qquad \text{for } x=0 \\ \frac{\partial^2 w}{\partial x^2} &= -I_t \frac{\partial^3 w}{\partial t^2 \partial x} + V(x,t) \\ \frac{\partial^3 w}{\partial x^3} &= M_t \frac{\partial^2 w}{\partial t^2} + \frac{\partial V(x,t)}{\partial x} \end{aligned}\right\} \quad \text{for } x=1 \quad . \tag{3.11}$$

For the development work, the simplest damper would have a uniform geometry and have a spatially uniform voltage applied along its length. For this configuration, the spatial derivatives of the input voltage are zero for the system described in Eqns. (3.10) and (3.11), leaving

$$\frac{\partial^4 w}{\partial x^4} + \frac{\partial^2 w}{\partial t^2} = 0 \qquad \text{for } x: \ 0<x<1 \tag{3.12}$$

with boundary conditions

$$
\begin{aligned}
w \;=\; \frac{\partial w}{\partial x} \;&=\; 0 && \text{for } x=0 \\
\frac{\partial^2 w}{\partial x^2} \;&=\; -\,I_t \frac{\partial^3 w}{\partial t^2 \partial x} \;+\; V(t) \\
\frac{\partial^3 w}{\partial x^3} \;&=\; M_t \frac{\partial^2 w}{\partial t^2} && \text{for } x=1 \quad .
\end{aligned}
\tag{3.13}
$$

Notice that the control voltage only appears in one of the boundary conditions. Therefore, Eqns. (3.12) and (3.13) describe a linear distributed-parameter system that has only boundary control. Since the actuator is a distributed-parameter actuator, the control was easily included in the equations of motion without nonlinear terms (e.g., spatial delta functions). This allows one to keep a linear distributed-parameter model throughout the analysis, avoiding any problems that may be caused by 'truncating' the model.

3.2 Deriving a Distributed-Parameter Control Algorithm

Distributed-parameter control theory was used to design a control algorithm for the active damper. This allows one the possibility of controlling all the modes of vibration at once, provided that the system is controllable through the actuator. Hence one may avoid problems with the spillover of the uncontrolled modes [4].

The control problem is to actively damp the vibrations of the system described by Eqns. (3.12) and (3.13) using the dimensionless input voltage, $V(t)$, as the control variable. This dimensionless derivation can easily be converted to a dimensional formulation by substituting from the definitions of the dimensionless variables given in Eqn. (3.9). Assuming that there is some practical limit on the magnitude of V, i.e.,

$$
\left| V(t) \right| \;\leq\; V_{max} \quad . \tag{3.14}
$$

For the moment, assume there is no restriction on the type of sensors available.

Lyapunov's second or direct method can be used as a design method for control systems that can easily deal with bounded inputs and can be extended to distributed-parameter systems [6, 27]. With this method, one defines a functional that may resemble the energy of the system and chooses the control to minimize (or make as negative as possible) the time rate of change of the functional at every point in time. An appropriate functional for the system described by Eqns. (3.12) and (3.13) is the sum of the squares of the displacement

and velocity, integrated along the length of the beam, or

$$F = \frac{1}{2}\int_0^1 \left(w^2 + \left(\frac{\partial w}{\partial t}\right)^2 \right) dx \quad . \tag{3.15}$$

Taking the time derivative of the functional yields

$$\frac{\partial F}{\partial t} = \int_0^1 \left(w \cdot \frac{\partial w}{\partial t} - \frac{\partial w}{\partial t} \cdot \frac{\partial^2 w}{\partial t^2} \right) dx \quad . \tag{3.16}$$

Substituting from the governing equation, Eqn. (3.12), gives

$$\frac{\partial F}{\partial t} = \int_0^1 \left(w \cdot \frac{\partial w}{\partial t} - \frac{\partial^4 w}{\partial x^4} \cdot \frac{\partial w}{\partial t} \right) dx \quad . \tag{3.17}$$

Integrating the second term by parts twice to introduce the boundary conditions yields

$$\begin{aligned} \frac{\partial F}{\partial t} = & \int_0^1 \left(w \cdot \frac{\partial w}{\partial t} - \frac{\partial^3 w}{\partial t \partial x^2} \cdot \frac{\partial^2 w}{\partial x^2} \right) dx \\ & - M_t \cdot \frac{\partial^2 w}{\partial t^2} \cdot \frac{\partial w}{\partial t}\bigg|_{x=1} - I_t \cdot \frac{\partial^3 w}{\partial t^2 \partial x} \cdot \frac{\partial^2 w}{\partial t \partial x}\bigg|_{x=1} \\ & + V(t) \cdot \frac{\partial^2 w}{\partial t \partial x}\bigg|_{x=1} \quad . \end{aligned} \tag{3.18}$$

The input voltage, vprime, only appears in one term. Therefore, to minimize Eqn. (3.18), the control voltage should be chosen so that the term it appears in is always as negative as possible, or

$$V(t) = - \operatorname{sgn}\left(\frac{\partial^2 w}{\partial t \partial x}\bigg|_{x=1} \right) \cdot V_{max} \tag{3.19}$$

where $\left.\frac{\partial^2 w}{\partial t \partial x}\right|_{x=1}$ is the dimensionless angular velocity at the tip of the beam. The control voltage should be chosen with as large a magnitude as possible and should generate a torque that always opposes the angular motion of the tip of the beam. In this manner, the maximum amount of work is being done against the beam at all times, taking as much energy as possible out of the system at every point in time. Since the Lyapunov functional used was related to the energy of the system, this was the goal of the design method. The torque produced using this control law would be similar to the torque produced by angular coulomb friction at the tip of the beam.

The Lyapunov control law, Eqn. (3.19), has several desireable characteristics. First, no

modes have been truncated. This control law will (theoretically) work on any and all modes of vibration of a cantilever since every mode has some angular motion at the tip of the beam. Secondly, the control law depends only on the angular velocity at the tip of the beam, not an integral along its length. This means that only one *discrete* sensor is needed to implement this distributed-parameter contol law.

There are also several disadvantages with this control law. The sgn(·) function is nonlinear and discontinuous when its arguement is zero. This nonlinear control law could lead to problems such as limit-cycling and/or sliding modes [6]. A practical drawback for this study is that the angular velocity of the tip of the beam is not readily available[1]. However, the accelerometer at the tip of the beam measures the linear acceleration which can be integrated to find the linear velocity of the tip. Also, for any given mode of vibration, the linear velocity is directly proportional to the angular velocity at the tip of the beam, although this relation does not hold if more than one mode of vibration is present. Therefore, it was decided to perform the preliminary testing of the damper on only one mode of vibration at a time. The first mode was chosen for the free decay tests because it was the easiest mode to isolate. The Lyapunov control law will be revised in Section 3.3 to use the linear velocity rather than the angular velocity of the tip of the beam. Note that the analysis has been broken into separate modes due to sensor limitations, not analytical or computational, and that the limitation has nothing to do with having a distributed-parameter system.

There also exists distributed-parameter optimal control theory where a cost function involving the states and control of the system is minimized. An extension of the classical variational approach to lumped-parameter optimal control for distributed-parameter systems is described by Tzafestas [13]. Appendix E describes an attempt to apply this method of optimal control to a cantilever beam without tip mass or tip inertia. A state vector is chosen and the equations of motion are written in matrix form. The system matrices are similar to those found in lumped-parameter control theory, but may include spatial operators such as differentials or integrals. A general cost function is described which would allow spatial crossweighting of elements in the state and control vectors as well as weighting between elements. This cost function is augmented with Lagrange multipliers to include the constraints imposed by the equations of motion.

---

[1] An angular accelerometer is currently on order.

Following the approach described by Tzafestas [13], the canonical equations needed to minimize the augmented cost function are derived using distributed-parameter calculus of variations. There are some difficulties in following Tzafestas' formulation directly due to singular matrices in the system boundary operator, but these can be avoided by expanding the matrix notation, performing the desired operation (e.g., applying Green's theorem) on each equation, and recombining the results back into matrix notation as needed. After finding the canonical equations, one assumes a feedback solution for the adjoint states and proceeds to derive a distributed-parameter Riccati equation from the canonical equations. The solution to this Riccati equation could then be used to determine the optimal control torque. No dedicated attempt was made to solve this equation.

This approach is very analogous to lumped-parameter optimal control theory, but having both space and time as continuous dimensions adds a good deal of mathematical complexity. Questions as to the validity of certain operations during the optimization were raised. More information about the properties of certain matrices is necessary to answer these questions. The reader is referred to Appendix E for the derivation of the Riccati equation and discussion of the questions.

3.3 Alternative Control Laws

The Lyapunov control law could not be implemented because the angular velocity of the tip of the beam is not available, but if only one mode of vibration is present the linear velocity is proportional to the angular velocity at the tip of the beam. Rewriting the Lyapunov control, Eqn. (3.19), in terms of the linear velocity at the tip of the beam gives

$$V(t) \;=\; -\,\mathrm{sgn}\left(\mathrm{f}\cdot\left.\frac{\partial w}{\partial t}\right|_{z=1}\right)\cdot V_{max} \tag{3.20}$$

where f is a constant which expresses the ratio between the dimensionless angular velocity and the dimensionless linear velocity at the tip of the beam. This constant, f, is needed as an arquement in the sgn(·) function because the sign of f affects the phase of angular velocity relative to the linear velocity. If f were negative and were not included in Eqn. (3.20), the resulting control would drive the vibrations of the beam, not damp them. This control law will work for any given mode of vibration as long as only that mode is present.

Two other control laws were developed to compare against the modified Lyapunov

control law, Eqn. (3.20). Written in terms of the linear velocity at the tip of the beam, they are

Constant-gain negative velocity feedback;

$$V(t) = -k \cdot \left(f \left. \frac{\partial w}{\partial t} \right|_{x=1} \right), \qquad \left| V(t) \right| \leq V_{max} , \tag{3.21}$$

Constant-amplitude negative velocity feedback;

$$V(t) = -k(t) \cdot \left(f \left. \frac{\partial w}{\partial t} \right|_{x=1} \right), \qquad \left| V(t) \right| \leq V_{max} , \tag{3.22}$$

where k is a feedback gain. As with the Lyapunov control law, the modified Lyapunov controller is nonlinear and discontinuous. The constant-gain controller is both linear and continuous. It can be derived from physical insight (negative velocity feedback tends to stabilize the system) or more rigorously from a modal control viewpoint. The drawback to this controller is that as the amplitude of the velocity decays, so does the feedback voltage amplitude. This will reduce the effectiveness of the damper at low vibration levels, for a given voltage limit. The constant-amplitude controller compensates for the decaying velocity amplitude by adjusting the feedback gain, $k(t)$, to keep the amplitude of the feedback voltage constant. This controller is continuous but nonlinear, and will be less effective (approximately 20%) than the modified Lyapunov controller because a square wave has more area than a sine wave if they have equal amplitude. However, the constant-amplitude controller may be more practical since the control circuitry will not have to produce high voltage step changes. The constant-gain and constant-amplitude controllers were evaluated experimentally (Section 4.2.3).

3.4 Simulation of the Lyapunov Control Law for a Single Mode

This section develops a simulation algorithm to predict the effect of the active damper on the free decay of a single mode of the cantilever beam. Section 3.4.1 presents the simulation algorithm. The next three sections develop equations that are needed for the simulation algorithm. Section 3.4.2 describes a method used to determine the strain energy in the beam as a function of the modal displacement. Section 3.4.3 determines the work done on the beam by the active damper. The energy dissapated by passive damping is determined in Section 3.4.4. Section 3.4.5 demonstrates the simulation algorithm on the first mode of

the composite cantilever beam.

3.4.1 The simulation algorithm

The simulation algorithm is as follows:

1. Start with the beam having some initial displacement amplitude (only one mode shape may be present) and an initial velocity of zero.

2. For each half-cycle of vibration, determine the amount of work done on the beam by the active damper and the energy dissapated by any passive damping in the system.

3. Subtract the amount of energy lost during the half-cycle from the amount of energy in the system at the beginning of the half-cycle. Use the remaining energy to determine the corresponding displacement amplitude of the beam.

4. Repeat steps 2 and 3 until the displacement amplitude reaches zero.

This algorithm assumes that the control will not significantly change the mode of vibration. The first mode of vibration and the modified Lyapunov control law were chosen to demonstrate the simulation. The tip displacement was chosen to represent the modal displacement. This simulation algorithm essentially gives the decay envelope of the vibration since the displacement amplitudes are found every half-cycle. Figure 3-4 shows the first few half-cycles of a simulation.

3.4.2 Bending strain energy as a function of tip displacement

To implement the simulation algorithm, one must know the potential energy in the mode as a function of the modal displacement (for this case, the tip displacement). One way to find this relation is to determine the mode shape and then integrate to find the total strain energy in the composite beam as a function of the tip displacement. Since it has been assumed that the control does not change the mode shapes, this study will use the mode shapes of the uncontrolled (homogeneous) system. The procedure used to find the mode shapes is given in Appendix B.

Assuming separation of variables, the transverse motion can be separated into two parts, one that depends on space, x and another that depends on time, t, or

$$w(x,t) = \Phi(x)\cdot\Psi(t) \tag{3.23}$$

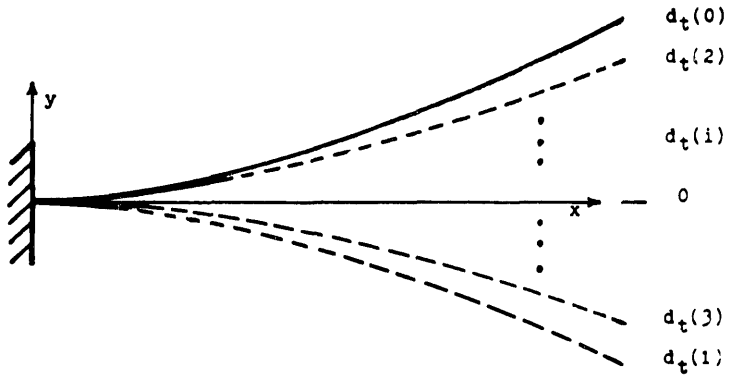

Figure 3-4: Several steps of a simulation.

where $\Phi(x)$ is the mode shape and $\Psi(t)$ is the modal amplitude. The dimensionless shape of the first mode, Φ_1, is given by (see Appendix B)

$$\Phi_1(x) = \cos(1.20x) - \cosh(1.20x) - 0.887(\sin(1.20x) - \sinh(1.20x)) \quad . \tag{3.24}$$

Next, the equation relating the modal amplitude and the tip displacement is found so that the tip displacement can be used to represent the modal displacement. The dimensionless tip displacement, d_t, is given by (for the first mode)

$$\begin{aligned} d_t(t) &= w(1,t) = \Phi_1(1)\cdot\Psi(t) \\ &= 0.936 \cdot \Psi(t) \quad . \end{aligned} \tag{3.25}$$

Using this equation, the transverse motion of the first mode can be described by

$$w(x,t) = 1.07 \cdot \Phi_1(x) \cdot d_t(t) \tag{3.26}$$

where the tip displacement, d_t, represents the modal displacement.

The dimensional strain energy due to bending of the composite beam is given by (from Eqn. (A.20))

$$E_b = \frac{1}{2}\int_0^l EI \left(\frac{\partial^2 w}{\partial x^2}\right)^2 \, dx \tag{3.27}$$

where EI is the total bending stiffness of the composite beam. To find the equivalent non-dimensional energy equation, divide this equation by EI/l and substitute the dimensionless variables defined in Eqn. (3.9). This yields

$$E_b = \frac{1}{2}\int_0^1 \left(\frac{\partial^2 w}{\partial x^2}\right)^2 \, dx \quad . \tag{3.28}$$

where E_b is the dimensionless bending strain energy. Substituting for the transverse motion, w, from Eqn. (3.26), using the first mode shape given in Eqn. (3.21), performing the differentiation and integration yields

$$\begin{aligned} E_b &= g \cdot (d_t)^2 \\ &= 1.08 \cdot (d_t)^2 \end{aligned} \tag{3.29}$$

where g is a constant (for a given mode) that expresses the dimensionless energy in the beam per unit dimensionless tip displacement squared. This is the equation relating the strain energy in the beam and tip displacement for the first mode.

3.4.3 Work done by the active damper

Another equation that is needed to implement the simulation algorithm is the work done on the beam by the active damper every half-cycle. The active damping works on the beam through the dimensionless control voltage, V, at the tip of the beam (see equations of motion, Eqns. (3.12) and (3.13)). The dimensionless work done on the system by the control voltage is given by

$$E_c = \int_{t_i}^{t_f} V(t) \cdot \left.\frac{\partial^2 w}{\partial x \partial t}\right|_{x=1} \, dt \tag{3.30}$$

where times t_i and t_f are the beginning and end of each half-cycle, respectively. Because the angular velocity (and hence the linear velocity) does not change sign during a given half-cycle (see Figure 3-4), the modified Lyapunov control law, Eqn. (3.20), calls for a constant control voltage over this time interval. This means that the integral in Eqn. (3.30) reduces to

$$E_c = \pm V_{max}(\theta(t_f) - \theta(t_i)) \tag{3.31}$$

where θ is the tip angle, and the sign of the control voltage is determined by the modified Lyapunov control law.

Since the tip displacement is being used to represent the modal displacement, next find the relationship between the tip angle and tip displacement. The tip angle, θ, is defined by

$$\theta = \left.\frac{\partial w}{\partial x}\right|_{x=1} \tag{3.32}$$

and substituting for w from Eqn. (3.26) and performing the differentiation, the equation relating tip angle to dimensionless tip displacement for the first mode is

$$\begin{aligned} \theta(t) &= 1.48 \cdot d_t \\ &= \mathrm{f} \cdot d_t \end{aligned} \tag{3.33}$$

where f is a constant (for a given mode) that relates the tip angle to the dimensionless tip displacement. This is the constant that is used in the modified Lyapunov control law. Substituting this equation into Eqn. (3.31) gives the work done by the control voltage in terms of the tip displacement,

$$E_c = \pm V_{max}\, \mathrm{f}\, (\, d_t(t_f) - d_t(t_i)\,) \tag{3.34}$$

or

$$E_c = \pm V_{max} \cdot 1.48 \cdot (\, d_t(t_f) - d_t(t_i)\,) \tag{3.35}$$

for the first mode.

Using the modified Lyapunov control law (Eqn. (3.20)), the sign of the control voltage depends only on the sign of f times the linear velocity at the tip of the beam. When $d_t(t_i)$ is positive, $d_t(t_f)$ is negative and the linear velocity during the half-cycle is negative. For this half-cycle, the control voltage will be opposite the sign of f times the linear velocity, or positive for the first mode. When $d_t(ti)$ is negative, then the other parameters also switch signs. Generalizing from these relations, and using Eqn. (3.33) in Eqn. (3.31), the work done by the control voltage is

$$E_c = -\, V_{max} \cdot \left|\mathrm{f}(\, d_t(t_f) - d_t(t_i)\,)\right| \tag{3.36}$$

or, for the first mode,

$$E_c = -\, 1.48 \cdot V_{max} \cdot \left|d_t(t_f) - d_t(t_i)\right| \tag{3.37}$$

for each half-cycle of vibration of the first mode.

3.4.4 Energy dissapated by passive damping

The next step is to find the energy dissapated by passive damping per half-cycle for a given mode. The structural loss factor, eta, is defined by [28]

$$\eta = \frac{E_{dis}}{E_{sys}} \cdot \frac{1}{2\pi} \tag{3.38}$$

where E_{dis} is the energy dissapated during one cycle of vibration, and E_{sys} is the total energy in the system at the beginning of the cycle. Each mode has a loss factor associated with it so the loss factor is sometimes referred to as the modal loss factor. Note that the loss factor is a dimensionless parameter and will be the same for any dynamically scaled system. For small values of η, the loss factor is related to the damping ratio, ς, of the system by $\eta = 2 \cdot \varsigma$. The decay envelope for the vibrations of a system with very little damping can then be written as

$$\psi(t) = \psi(0) \cdot \exp\left(\frac{-\eta w t}{2} \right) \tag{3.39}$$

where ψ is the amplitude of the decay envelope and w is the dimensionless natural frequency. The natural frequency is found while determining the mode shape. The predicted dimensionless natural frequencies for the first four modes of the cantilever beam are listed in Table B-I. For the cantilever beam, the tip displacement at the end of the half-cycle, $d_t(t_f)$, is given by

$$d_t(t_f) = d_t(t_i) \exp\left(\frac{-\eta\pi}{2} \right) \tag{3.40}$$

since $wt = \pi$ for a half-cycle of vibration.

From the equation for bending energy in the beam Eqn. (3.29), the energy in the beam at the end of the half-cycle is given by

$$\begin{aligned} E_b(t_f) &= g \cdot d_t(t_f)^2 \\ &= g \cdot d_t(t_i)^2 \exp(-\eta\pi) \\ &= E_b(t_i) \exp(-\eta\pi) \end{aligned} \tag{3.41}$$

where g represents the bending energy per unit tip displacement squared. The dimensionless energy dissapated during the half-cycle is the diffference, or

$$E_d = -(E_b(t_f) - E_b(t_i))$$
$$= (1 - \exp(-\eta\pi)) E_b(t_i)$$
$$= g \cdot (1 - \exp(-\eta\pi)) d_t(t_i)^2 \qquad (3.42)$$

or, using the value of g for the first mode (from Eqn. (3.29), the energy dissapated per half-cycle for the first mode is

$$E_d = 1.08 \cdot (1 - \exp(-\eta\pi)) d_t(t_i)^2 \quad . \qquad (3.43)$$

Note that E_d is assumed to be positive for work taken out of the system.

3.4.5 Demonstrating the simulation algorithm

The simulation algorithm described in Section 3.4.1 can be implemented using the results of Sections 3.4.2, 3.4.3, and 3.4.4. The energy in the beam after the half-cycle is the energy that was in the beam at the beginning of the half-cycle minus the energy dissapated by passive damping (Eqn. (3.42)), and the work done by the control voltage (Eqn. (3.34)), or

$$E_b(t_f) = E_b(t_i) - E_d + E_c \quad . \qquad (3.44)$$

Substituting the equations for the energies yields

$$g \cdot d_t^2(t_f) = g \cdot \exp(-\eta\pi)\ d_t^2(t_i) \ \pm\ V_{max} \cdot f\ (\ d_t(t_f) - d_t(t_i)\ ) \quad . \qquad (3.45)$$

This is a quadratic equation in $d_t(t_f)$ which can be solved using the quadratic formula. The quadratic formula gives

$$d_t(t_f) = \frac{\pm V_{max} f}{2 \cdot g} \pm \sqrt{\left(\frac{V_{max} f}{2 \cdot g}\right)^2 - \left(\frac{\pm V_{max} f}{2\ g}\ d_t(t_i)\right) + \exp(-\eta\pi)\ d_t^2(t_i)} \quad . \qquad (3.46)$$

Using the modified Lyapunov control law, Eqn. (3.20), to determine the sign on the control voltage, and choosing the sign on the radical so that the magnitude of the tip displacement is always decreasing, one can generalize a solution to the quadratic formula as was obtained for the work done by the control voltage (see Eqn. (3.36)). The general solution is

$$d_t(t_f) = -\frac{V_{max}f}{2\cdot g} + \sqrt{\left(\frac{V_{max}f}{2\cdot g}\right)^2 - \frac{V_{max}f}{2\cdot g}\left|d_t(t_i)\right| + \exp(-\eta\pi)\, d_t^2(t_i)} \quad . \quad (3.47)$$

This equation is used to perform the simulation and because the absolute value of the tip displacement is found, this is essentially the decay envelope. The simulation, in terms of number of time steps, only depends on the passive damping, η, and a term that includes the bending energy per tip displacement, g, the tip angle per unit tip displacement, f, and the control voltage limit, V_{max}. This means that beams with the same passive damping and the same dimensionless terms (g, f, V_{max}) will have the same simulation results in terms of number of time steps (not necessarily t). It also means that beams with the same passive damping and the same value for the term $\frac{V_{max}f}{2\,g}$ will also have the same simulation results because the simulation depends on this term, not the individual values. The time interval between time steps is determined from $t=\pi/w$ because the time step spans one half-cycle of vibration.

For the parameter study, both the control voltage and the passive loss factor were varied. The symbol η_p will be used to denote the passive loss factor to distinguish from the active damping. Note that since the simulation depends only on the passive damping (which is directly varied for the parameter study) and the voltage term, $\frac{V_{max}f}{2\,g}$ (which is varied through V_{max}), the simulation results for any mode of a particular beam can be scaled to give the corresponding results for any mode of any other beam. The only criteria is that these two terms be the same. Since the passive loss factor is one term, the loss factor must be the same for both beams. The control voltage term would be scaled by choosing the control voltage limit so the voltage term would be the same for both beams. For instance, the simulation results for a beam with V_{max}=g=f=10 would be the same as for a beam with V_{max}=g=1 and f=10, for a given passive loss factor. The dimensionless time would then be scaled by the ratio of the natural frequencies or eigenvalues for the given mode of the beams. The dimensional results would then be found as usual by using the definitions of the dimensionless variables given in Eqn. (3.9).

There are several cases when certain parameters would not have to be rescaled to find the results for one mode of a beam from those of another. Since the dimensionless frequency, w, depends only on the eigenvalue of the mode (see Appendix B), when two beams have the same eigenvalue their dimensionless time scales, t, will also be the same. This means the results from the dimensionless simulation of one mode of a beam can be scaled to correspond to those of a different beam (a mode that has the same eigenvalue) without rescaling the time axis (i.e., only change the control voltage). This does not mean that the

mode shapes are also the same (i.e., the dimensionless tip masses and tip inertias are different, but the eigenvalues happen to be the same). If the dimensionless tip masses and tip inertias are the same, then the eigenvalues and the mode shapes will both be the same for the two beams (see Appendix B). Since the dimensionless terms g and f depend only on the eigenvalue and mode shape, the beams will have the same simulation results (in terms of the number of time steps) for a given control voltage, V_{maz}, and passive loss factor, η_p. This means the dimensionless simulation results for a mode of one beam are the same as those for any other beam with the same dimensionless tip mass and tip inertia.

For the first mode of the scaled cantilever beam, the simulation equation is

$$d_t(t_f) = -0.687 \cdot V_{maz} + \sqrt{(0.687 \cdot V_{maz})^2 - 1.37 \cdot V_{maz} \left| d_t(t_i) \right| + \exp(-\eta\pi)\, d_t^2(t_i)} \quad . \tag{3.48}$$

The results of two simulation cases are shown in Figure 3-5 and are labeled with both dimensionless and dimensional axes. The dimensional axes are for the scaled cantilever beam. The initial conditions were chosen as $d_t(0)= 0.146$ (2 cm tip displacement for the scaled beam). Figure 3-5a shows a case with a minimum control voltage limit, $V_{maz}= 4x10^{-6}$ (a dimensional voltage of 1 V for the scaled beam) and a passive loss factor of $\eta_p= 0.010$. Note that the measured torque constant, c, was used to non-dimensionalize the control voltage. (See Section 4.2.1.) The decay envelope for this case is nearly exponential because the control voltage is so low and the passive damping is dissapating most of the energy in the beam. However, the active control does have a noticeable effect at very small displacements. A true exponential decay envelope would approach zero amplitude, but never reach it. In this case, the beam does reach zero near $t= 800$ (t=30 sec. for the scaled beam). Figure 3-5 b shows a case with a moderate control voltage, $V_{maz}= 4x10^{-4}$ (100 V for the scaled beam) and no passive damping, $\eta_p=0.000$. Notice that the decay envelope is linear, not exponential. This indicates nonlinear damping and is the result of the nonlinear modified Lyapunov control law doing all the damping.

In comparing the two simulation cases, one should note several points. First, the slope of the passively damped case is initially much higher than the actively damped slope, indicating the passive damping is taking more energy out of the beam than the active damping. However, the slope of the passively damped case changes because of the exponential decay envelope and soon becomes less than the actively damped slope (which is constant), now indicating the active damping is more effective. This is because the passive

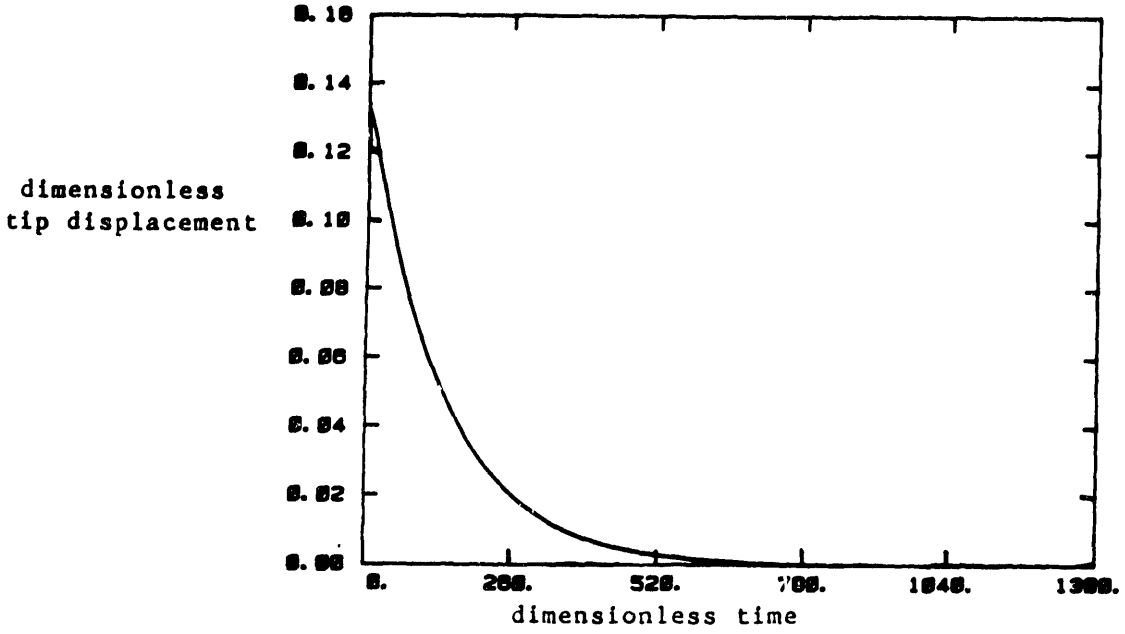

(a). Free decay of first mode simulation. $\eta_p = 0.010$
$V_{max}=4x10^{-6}$.

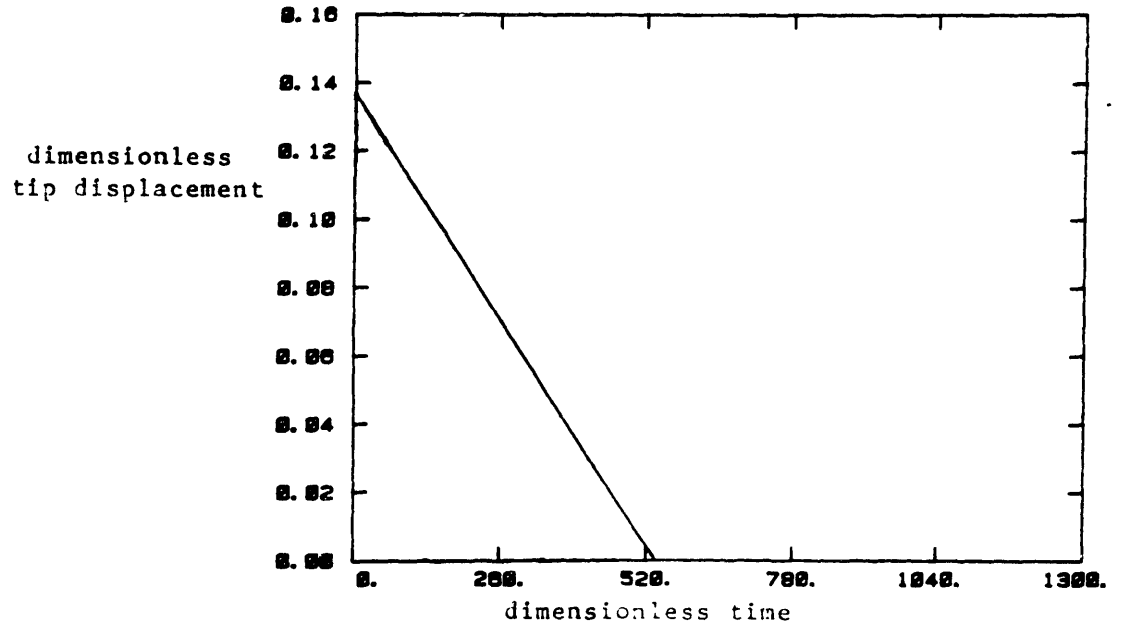

(b). Free decay of first mode simulation. $\eta_p = 0.000$
$V_{max}=4x10^{-4}$.

Figure 3-5: Typical simulation results for free decay of first mode.

damping dissapates a fixed percentage of the energy in the system per half-cycle, by definition. For the active damping, on the other hand, the percentage of energy dissapated per cycle increases until the amplitude of vibration reaches zero. Secondly, since the slope of the passively damped case is changing and the actively damped case has constant slope, there is a distinct tip displacement and time below and after which the active damping becomes more effective. This could be used as a design guide to determine which type of damping would be more effective in a given application.

3.5 Parameter Study Results

This section presents the results of a parameter study that was performed using the simulation algorithm developed in Section 3.4. The simulation was for the first mode of the scaled cantilever beam and the control voltage limit, V_{max}, and the passive loss factor, η_p, are the only parameters that were varied. Six values of V_{max} and eight values of η_p were used. Table 3-I summarizes the simulation parameters in both dimensionless and dimensional form based on the scaled cantilever beam. The measured torque constant, c, was used to non-dimensionalize the control voltages (see Section 4.2.1). The initial tip displacement for the first mode was chosen to be $d_t(0) = 0.146$ (2 cm tip displacement for the scaled beam).

To illustrate the effect of changing the control voltage, V_{max}, and/or the passive loss factor, η_p, the 48 different simulation cases are presented in two different ways. Figures 3-6 through 3-11 each show how the decay envelope changes with the passive loss factor, η_p, for a fixed control voltage. Figures 3-12 through 3-19 each show how the decay envelope changes with the control voltage, V_{max}, for a fixed passive loss factor. All figures are the same scale and are labeled with dimensionless axes. The same axes were used in Figure 3-5 so the dimensional axes presented there may be used for reference to the scaled cantilever beam.

These simulations illustrate several points. Figures 3-6 through 3-11 emphasize the fact that the active damping is more effective than the passive damping below a certain displacement when using the modified Lyapunov control law. As the passive damping increases from $\eta_p = 0.000$ to 0.020, the added damping increases the slope of the decay envelope and makes the decay envelope more like an exponential. This is most noticeable for the lowest control voltage, $V_{max}=4\text{x}10^{-6}$, shown in Figure 3-6. Although the initial slope is much steeper with the passive damping, the slope decreases and approaches the slope of the

Table 3-I: Summary of Conditions for Parameter Study.

Simulation parameters for first mode of scaled beam.

	Dimensionless	Dimensional
Control voltages,	$4x10^{-6}$	1 (V)
	$4x10^{-5}$	10
	$4x10^{-4}$	100
	$8x10^{-4}$	200
	$2x10^{-3}$	500
	$4x10^{-3}$	1000
Passive loss factors,	0.000	
	0.001	
	0.002	
	0.003	
	0.005	
	0.007	
	0.010	
	0.020	
Tip mass	1.20	6.73 (kg)
Tip inertia	$3.71x10^{-3}$	$4.43x10^{-7}$ (kgm^2)
Initial tip displacement	0.14	2.0 (cm)
Bending strain energy per tip displacement squared	1.08	4.21 (Nm^{-1})
Tip angle per tip displacement	1.48	10.2 (rad/m)

case with only active damping, indicating that the active damping is most effective below a certain vibration amplitude. This crossover amplitude level depends on both the passive loss factor and the control voltage; the crossover amplitude increases as the control voltage increases, but decreases as the passive damping increases. This is clearly demonstrated by comparing Figure 3-6 where the control voltage is at its lowest value with Figure 3-11 where the control voltage is at its highest. The slope of the decay envelope with η_p=0.020, the highest passive loss factor, approaches the slope of the zero passive damping case only at very small amplitudes (d_t approx. 0.005) for the lowest control voltage. For the highest control voltage, though, the amplitude level is much higher (d_t approx. 0.06) and the effect of the passive damping is much less.

Figures 3-12 through 3-19 show the same results, but from a different perspective. Figure 3-12 shows the effect of active damping alone and how the slope of the decay envelope is directly related to the control voltage. As the passive loss factor is increased (Figures 3-13 through 3-19) the increase in the slope from the active damping gets smaller, especially for the larger tip displacements. However, even for the highest passive loss factor, η_p= 0.020, the active damping is much more effective when the tip displacement is small. For example, with η_p= 0.020, shown in Figure 3-19, the beam is stopped in 52 dimensionless time units after it reaches a tip displacement of d_t=0.02 for the case with V_{max}=4x10^{-4}. Compare this with 300 dimensionless time units after the tip displacement reaches d_t=0.02 for the case with V_{max}=4x10^{-6}. The increase from very litte control voltage to a moderate control voltage stops the beam nearly 6 times faster. The difference is even more pronounced if a smaller tip displacement or a lower passive loss factor are used.

As mentioned in Section 3.4.5, the reason that the active damping is more effective for small vibration amplitudes is that the passive damping dissapates a fixed percentage of the energy in the system each cycle. When the vibration amplitudes are relatively large, the system will contain large amounts of energy and the passive damping dissapates a relatively large amount of energy. When the vibrations are small, the system energy is small, and the passive damping will only dissapate a small amount of energy because only a fixed percentage of the system energy is dissapated. On the other hand, an actuator with a nonlinear control law such as the modified Lyapunov control law dissapates an increasing percentage of the system energy as the vibration amplitude decays. Since the decay envelope for the case with no passive damping has constant slope, the change in amplitude is the same from one time step to the next. For large amplitude vibrations, the ratio of amplitude from one time step to the next is near unity. As the amplitude decays, the ratio of amplitudes decreases also.

The ratio of energy in the system from one time step to the next is the square of the displacement amplitude ratio, so energy ratio decreases as the amplitude decays as well. Because the percentage of energy remaining in the system decreases, this means that the percentage of energy dissapated by the active damper increases as the vibration amplitude decreases. Another way of stating this is that the *effective* loss factor, η_{eff}, of the active damping increases as the vibration amplitude decreases, as opposed to the passive damping which has a constant loss factor. Note that this discussion only applies to the modified Lyapunov control law and similar nonlinear control laws. A linear, time invariant control law would have a constant loss factor while a control law with a time varying feedback gain would have a loss factor that depends on the time history of the gain. The constant-amplitude control law to be tested experimentally has a time varying feedback gain that increases as the amplitude of the vibrations decays so that η_{eff} increases also. (Linear systems that have a feedback gain as a control variable are called bi-linear systems [6].)

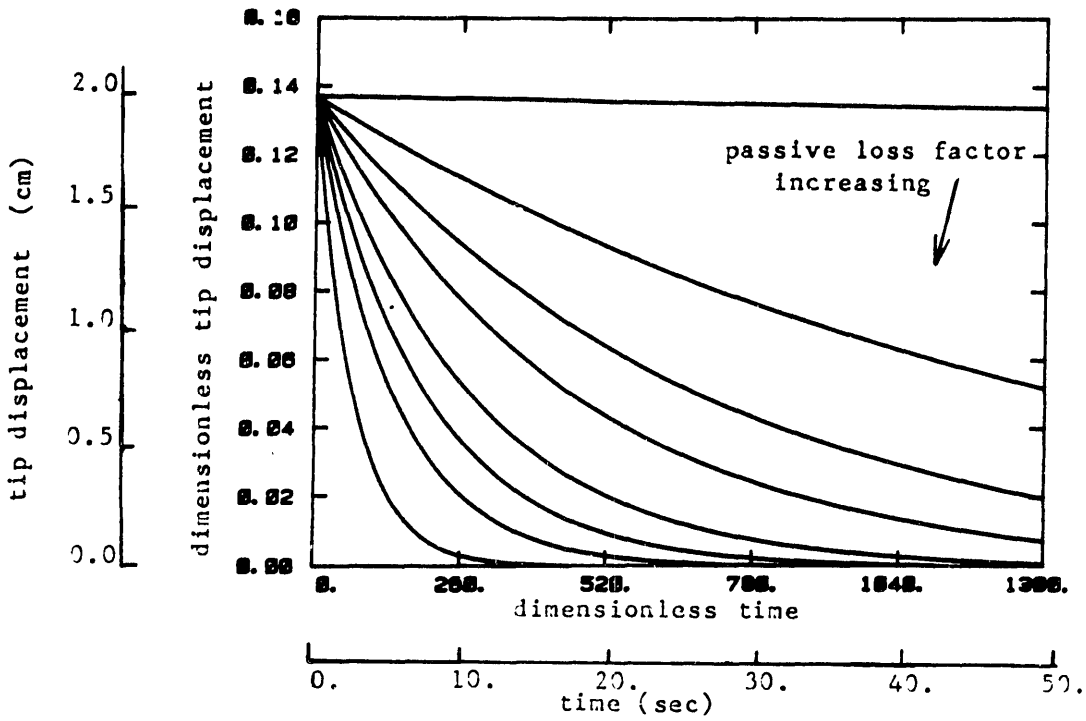

Figure 3-6: Tip displacement vs. time, decay envelope.
V_{max}=4x10^{-6}. Passive loss factor varied.

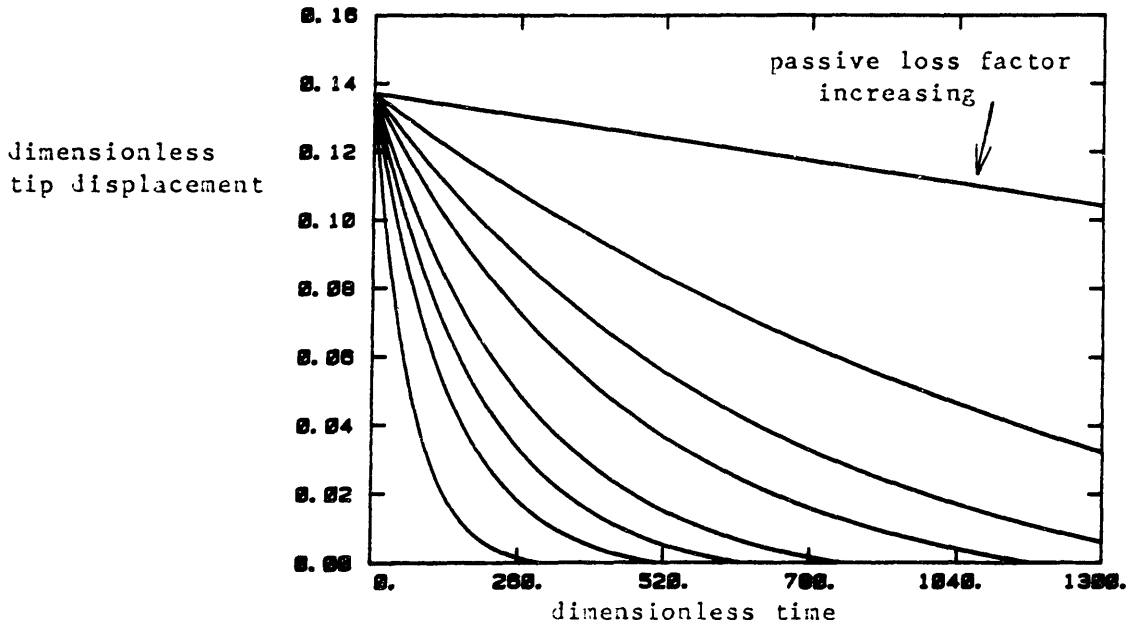

Figure 3-7: Tip displacement vs. time, decay envelope.
V_{max}=4x10^{-5}. Passive loss factor varied.

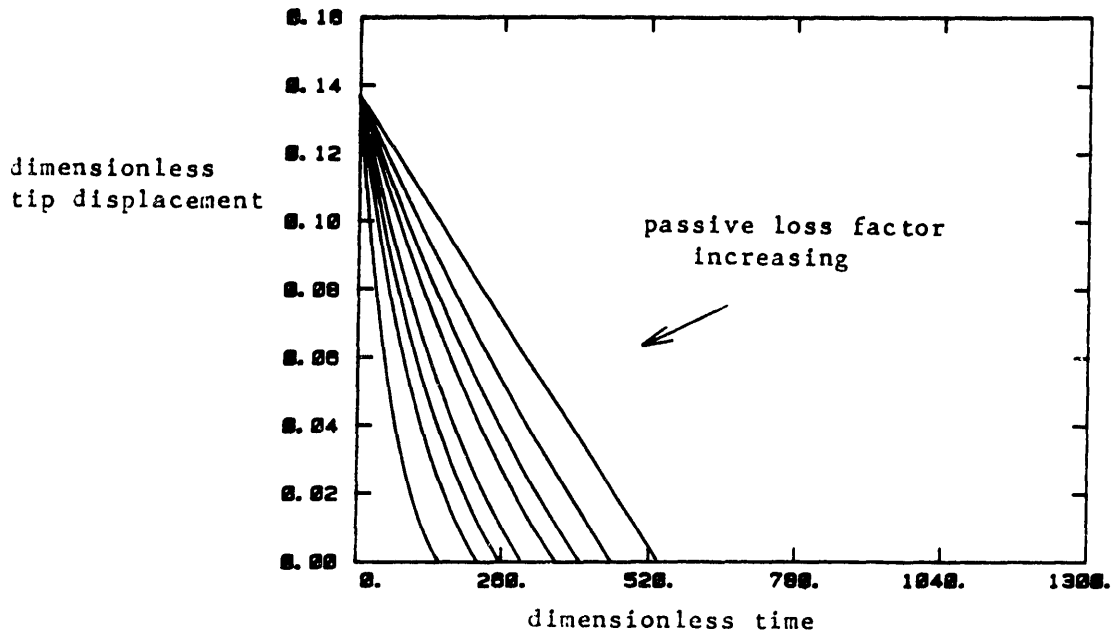

Figure 3-8: Tip displacement vs. time, decay envelope.
V_{max}=4x10^{-4}. Passive loss factor varied.

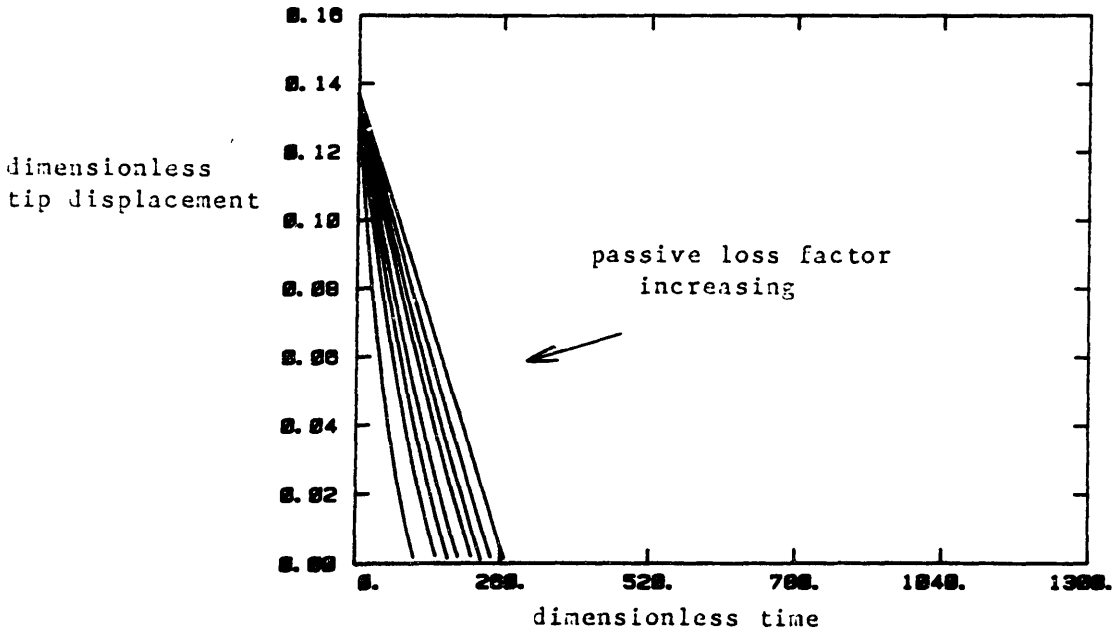

Figure 3-9: Tip displacement vs. time, decay envelope.
V_{max}=8x10^{-4}. Passive loss factor varied.

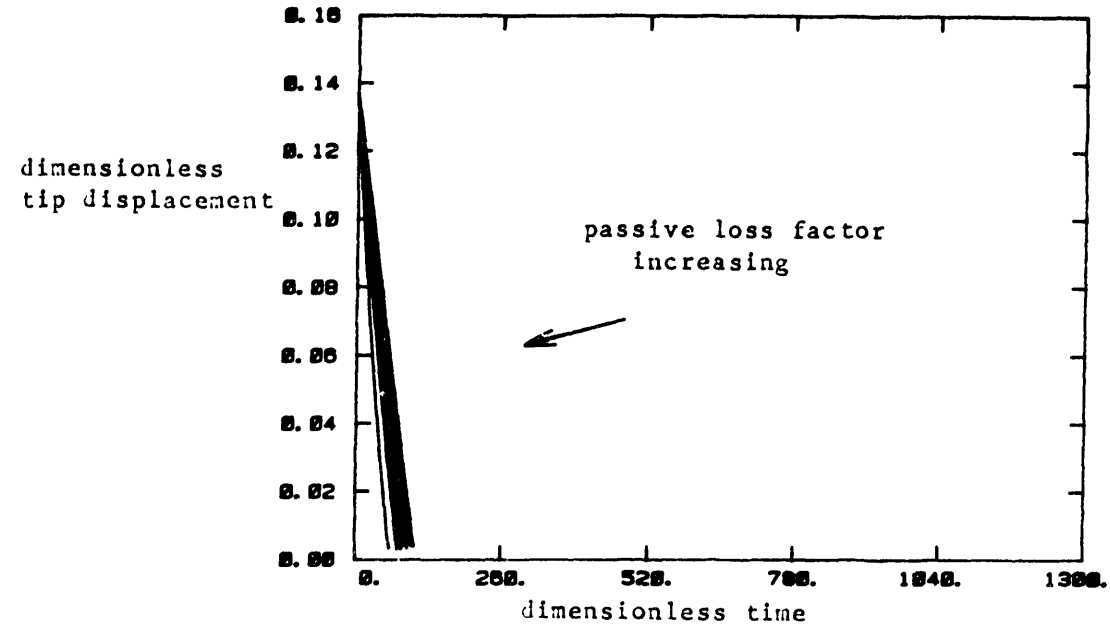

Figure 3-10: Tip displacement vs. time, decay envelope. V_{max}=2x10^{-3}. Passive loss factor varied.

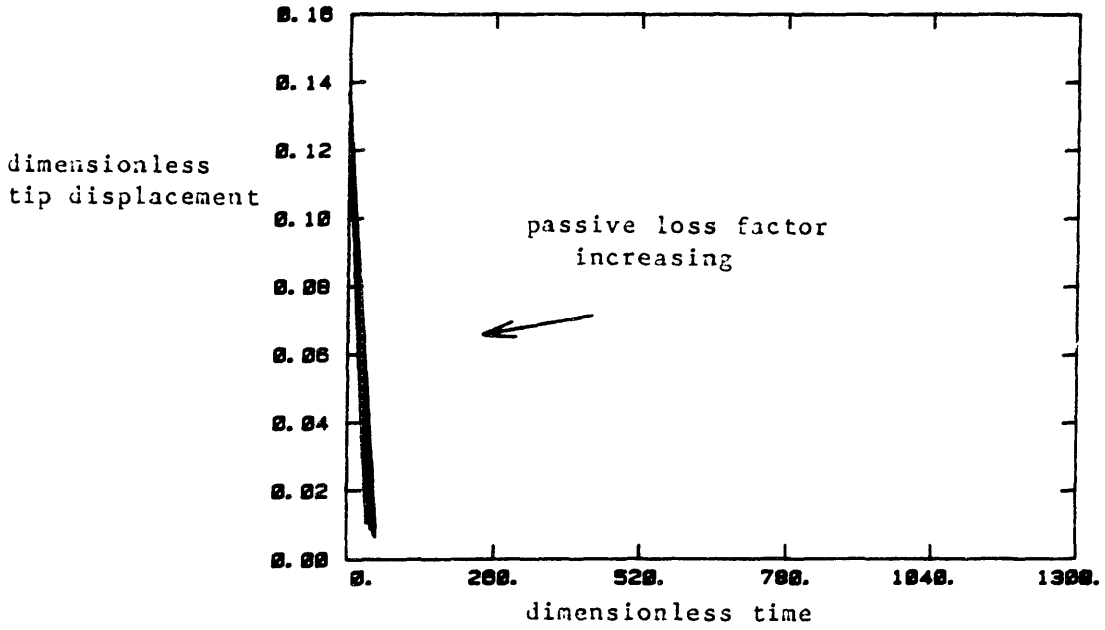

Figure 3-11: Tip displacement vs. time, decay envelope. V_{max}=4x10^{-3}. Passive loss factor varied.

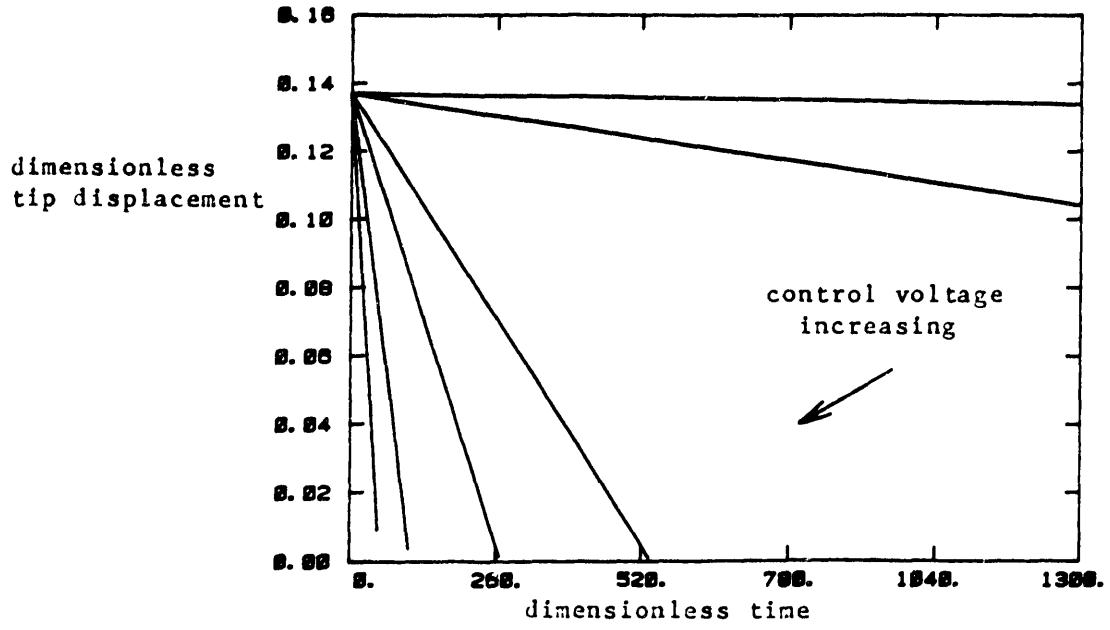

Figure 3-12: Tip displacement vs. time, decay envelope.
η_p=0.000 . Control voltage varied.

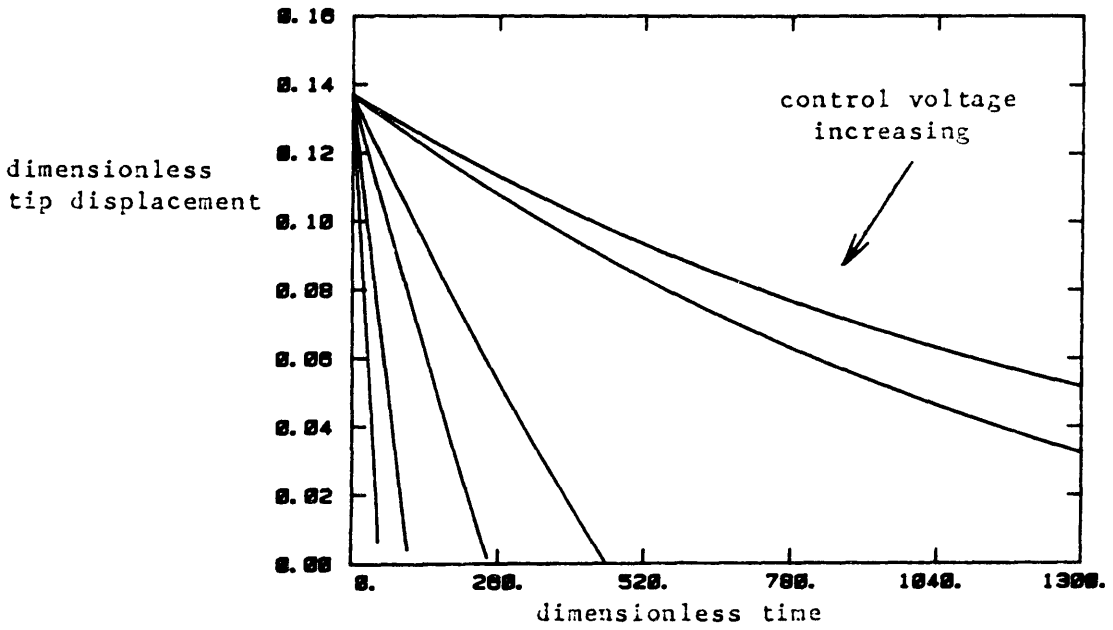

Figure 3-13: Tip displacement vs. time, decay envelope.
η_p=0.001 . Control voltage varied.

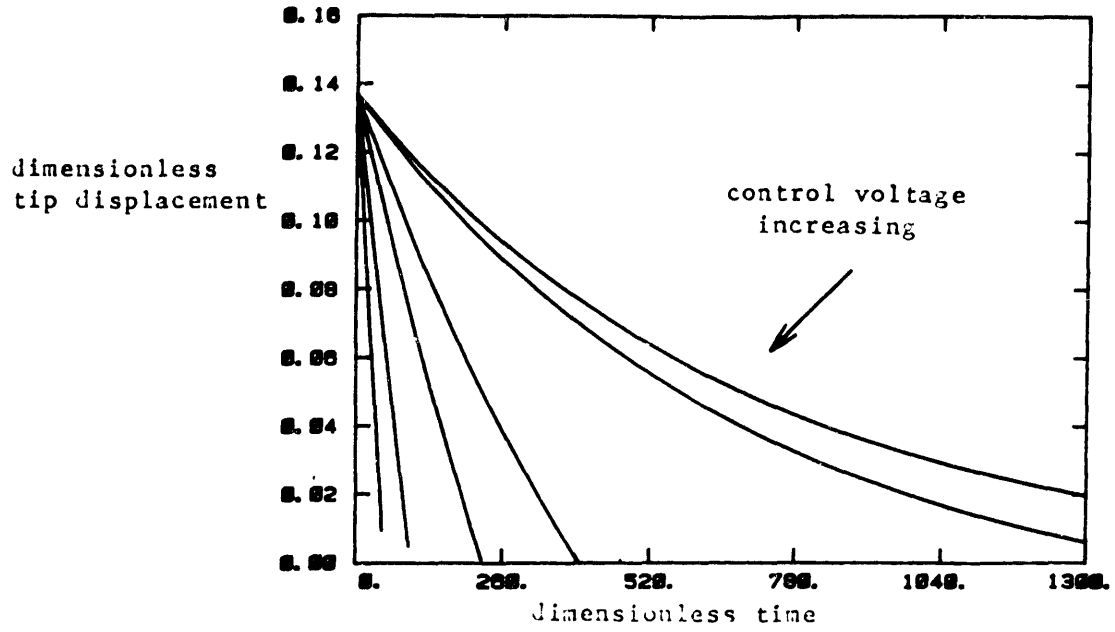

Figure 3-14: Tip displacement vs. time, decay envelope.
η_p=0.002 . Control voltage varied.

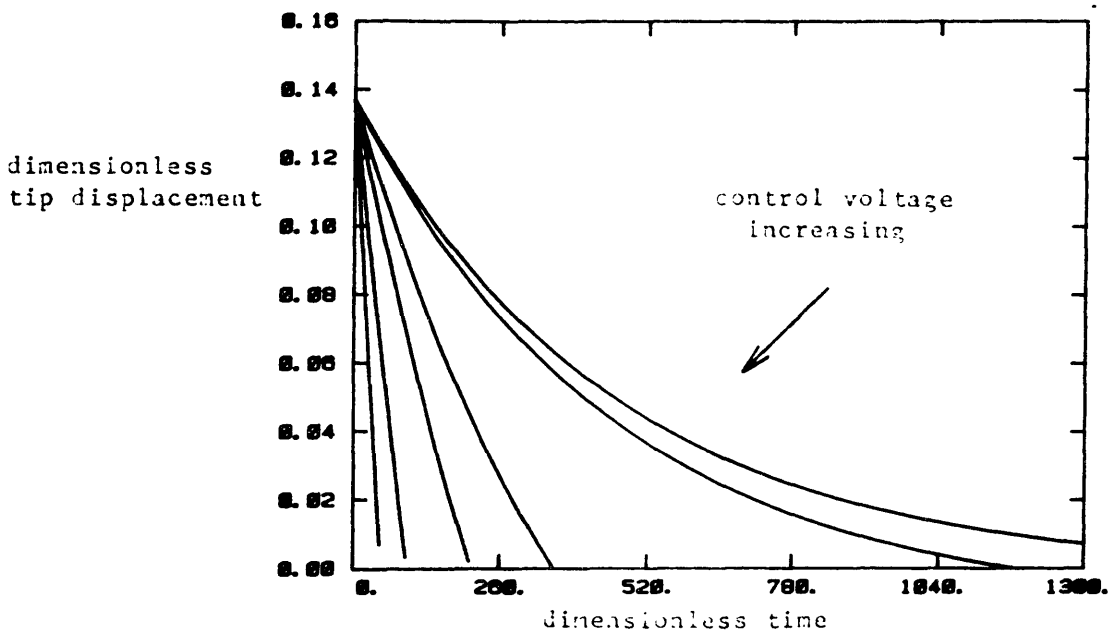

Figure 3-15: Tip displacement vs. time, decay envelope.
η_p=0.003 . Control voltage varied.

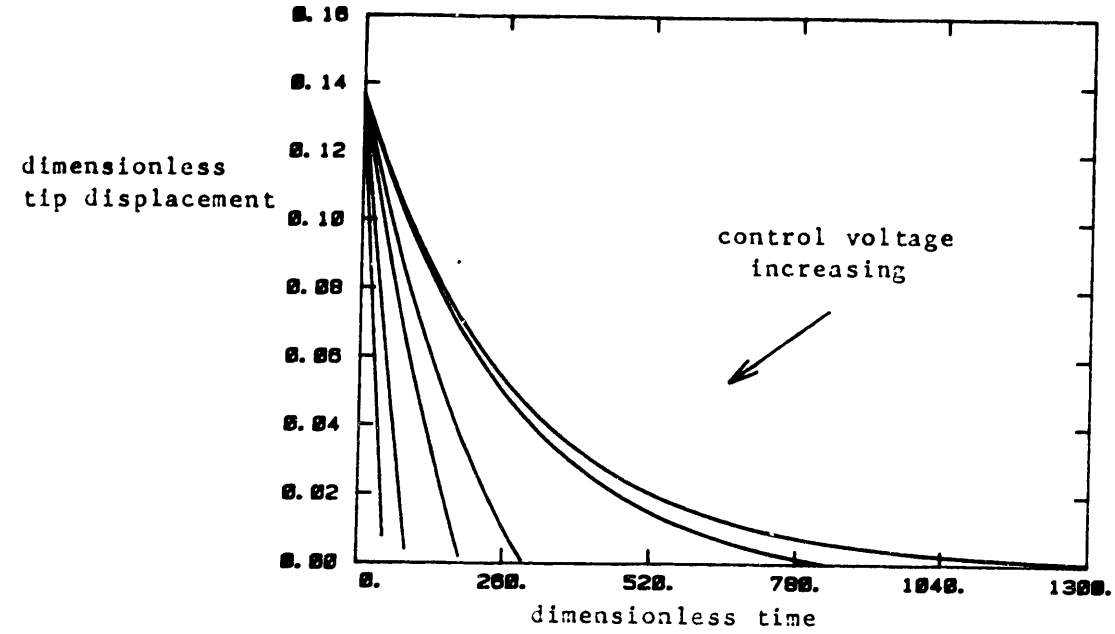

Figure 3-16: Tip displacement vs. time, decay envelope. η_p=0.005 . Control voltage varied.

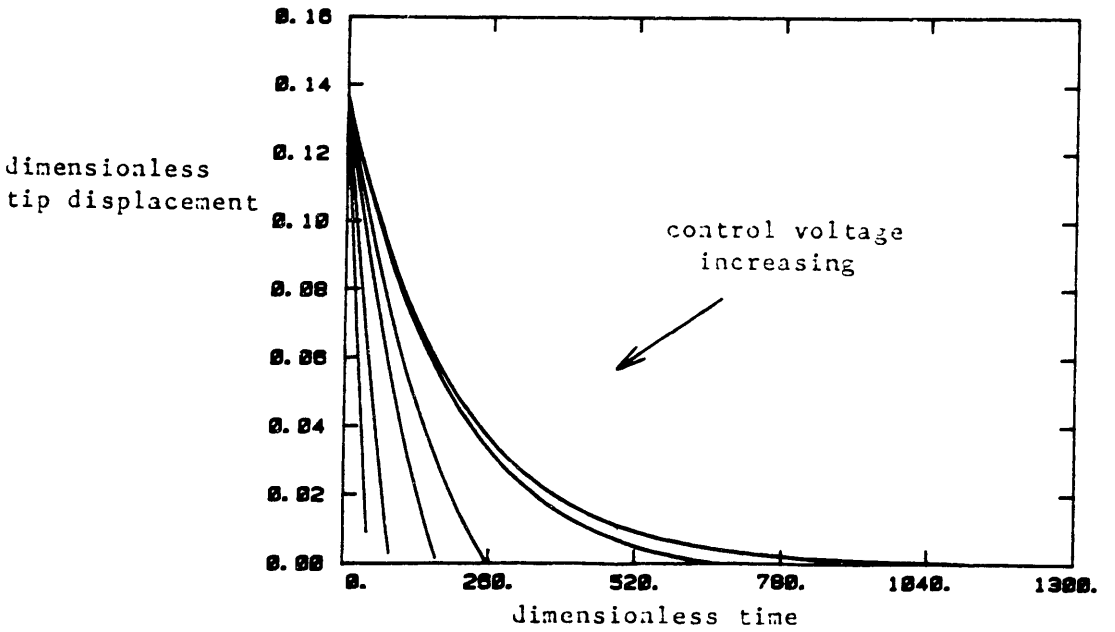

Figure 3-17: Tip displacement vs. time, decay envelope. η_p=0.007 . Control voltage varied.

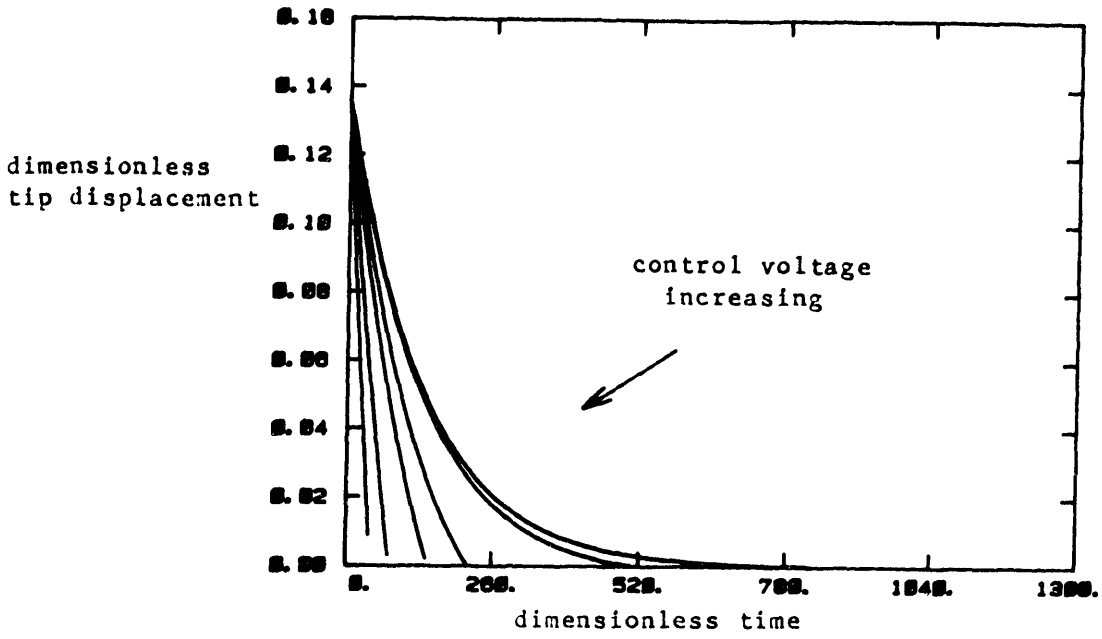

Figure 3-18: Tip displacement vs. time, decay envelope.
η_p=0.010 . Control voltage varied.

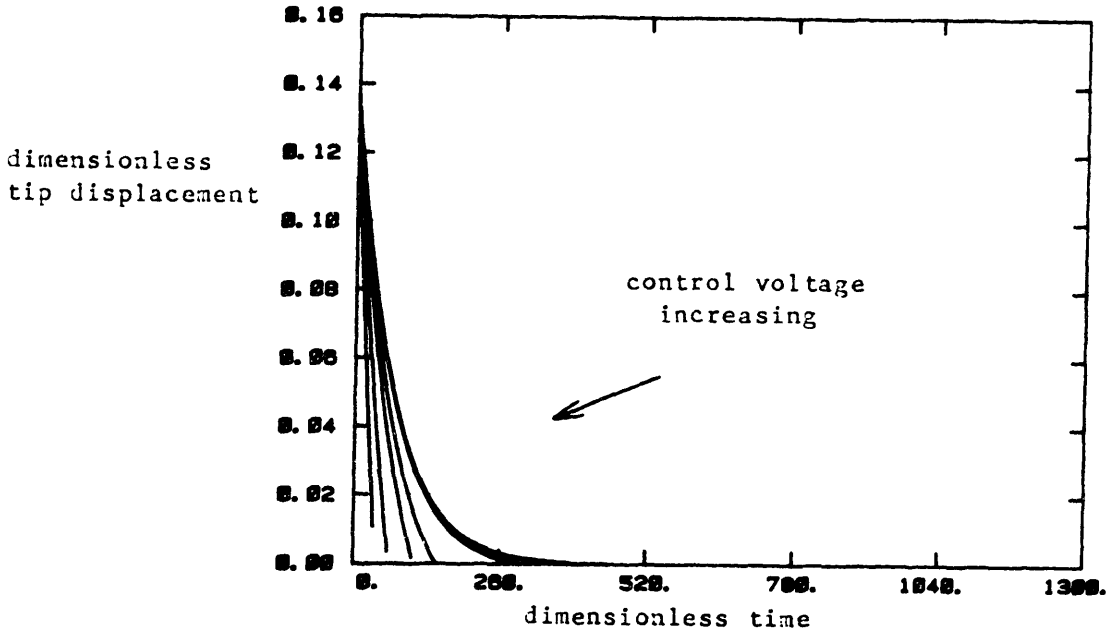

Figure 3-19: Tip displacement vs. time, decay envelope.
η_p=0.020 . Control voltage varied.

In this discussion of the simulations, the behavior of the slope of the decay envelope and the effective loss factor at various vibration amplitudes were noted in describing the effect of the active damping. To illustrate more clearly the trends that were mentioned, the simulation results were processed to provide slope vs. tip displacement and effective loss factor vs. tip displacement information (see Appendix D). The results are shown in Figures 3-20 through 3-33 and Figures 3-34 through 3-47 for the slope and effective loss factor, respectively. These Figures are organized in the same manner as the tip displacement vs. time Figures; for each Figure, one parameter, either the control voltage, V_{max}, or the passive loss factor, η_p, was held constant while the other was varied through its range. The first Figure in each set is labeled with dimensional axes that correspond to the scaled beam in addition to the non-dimensional axes.

Figures 3-20 through 3-25 show the slope vs. tip displacement plots for the cases where the control voltage is held constant and the passive loss factor is varied. Figures 3-26 through 3-33 are for the cases where the passive loss factor is held constant and the control voltage is varied. The cases with no passive damping are shown in Figure 3-26 which illustrates the constant slope of the decay envelope as a horizontal line on the slope vs. displacement plots. If the control voltage were zero, the slope of the decay envelope would be directly related to its amplitude by a factor that depends on the passive loss factor (i.e., the slope vs. tip displacement plots would be a straight line extending from the origin). This is most clearly illustrated by the cases with the minimum control voltage, $V_{max}=4\text{x}10^{-6}$. These are shown in Figure 3-20 and illustrate how increasing the passive loss factor increases the slope of the decay envelope for a given tip displacement (i.e., the 'slope' of the slope vs. tip displacement plot is increased when the passive loss factor increases). Because there is a control voltage, the slope vs. tip displacement plots are not exactly a straight line when passive damping is present. This is most noticeable with $V_{max}=4\text{x}10^{-3}$, the highest control voltage.

When the control voltage is increased, the effect is to increase the baseline slope of the decay envelope (i.e., change the y-intercept of the slope plots), which can be seen by comparing Figures 3-20 through 3-25. This can also be seen in Figures 3-26 through 3-33 where the passive loss factor is held constant and changes in the control voltage produce nearly parallel plots. Notice that the increase in the slope of the decay envelope as the passive loss factor increases is nearly the same regardless of the control voltage.

Since the slope of the decay envelope always approaches the baseline slope of the case with the same control voltage but no passive damping, this again shows that the active

damping is most effective for small vibration amplitudes. The slope vs. tip displacement plots show the amplitude dependence of the slope more clearly than the tip displacement vs. time plots, though. These plots can be used to predict the effectiveness of a combination of active and passive damping for a given vibration amplitude, passive loss factor, and control voltage. For example, they allow one to determine which type of damping is contributing most to the slope of the decay envelope and to examine different combinations of passive and active damping that would produce a given slope at a given tip displacement. This could be part of a design method for systems which will have a combination of passive and active damping.

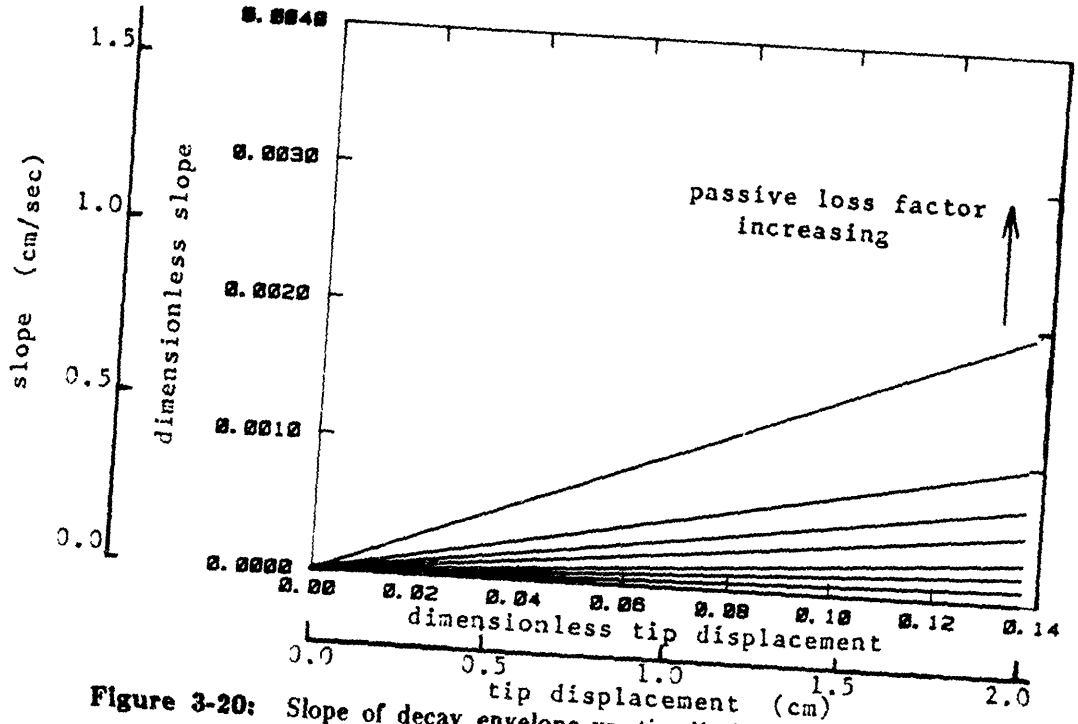

Figure 3-20: Slope of decay envelope vs. tip displacement. V_{max}=4x10^{-6}. Passive loss factor varied.

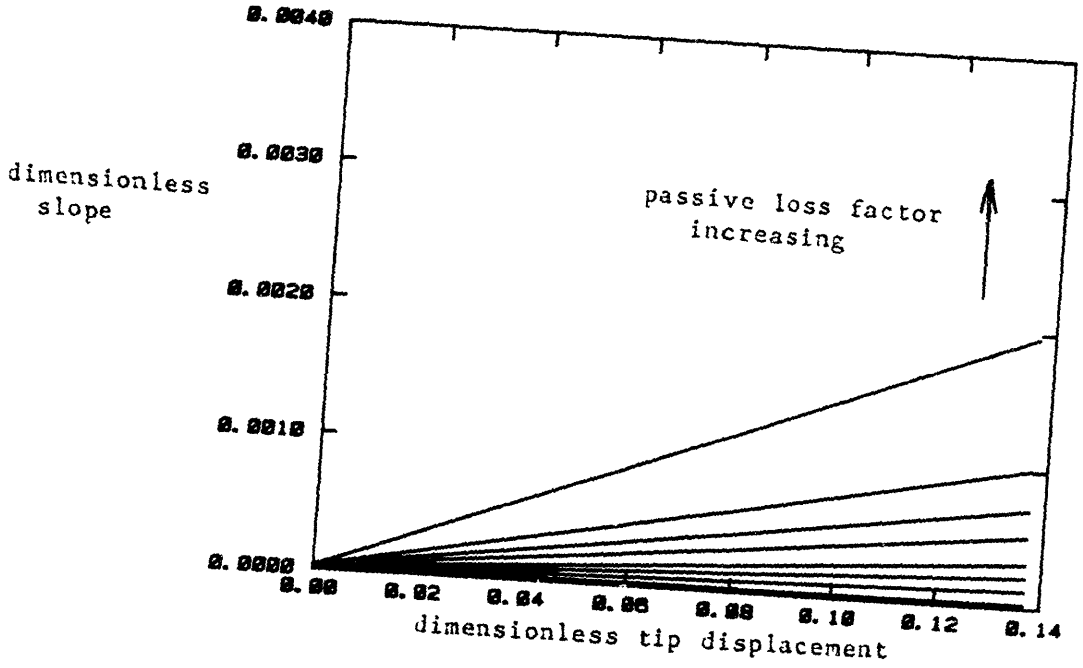

Figure 3-21: Slope of decay envelope vs. tip displacement. V_{max}=4x10^{-5}. Passive loss factor varied.

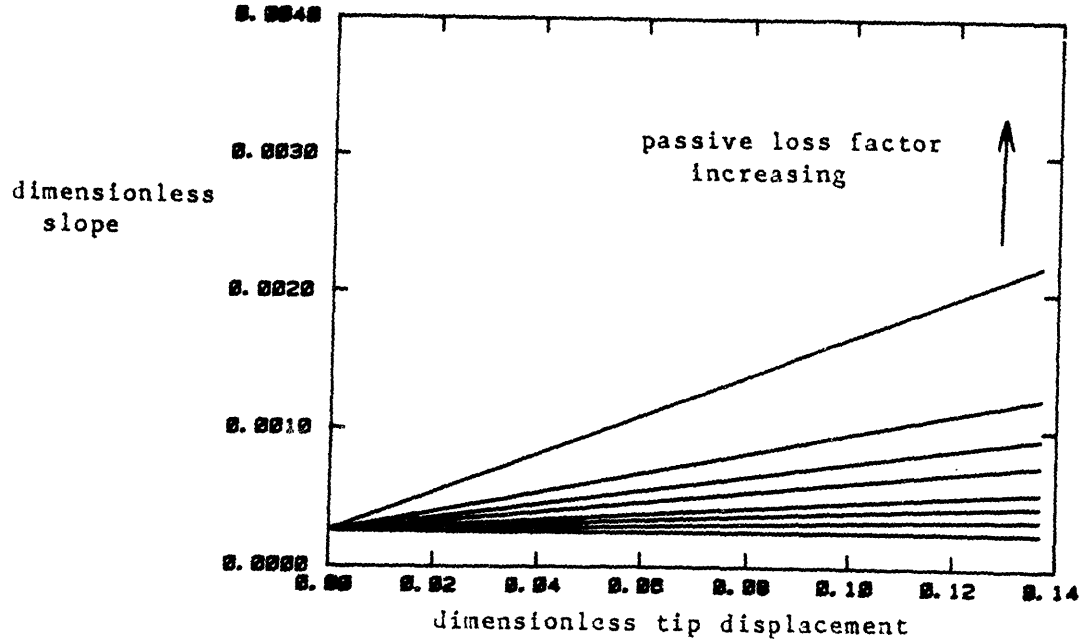

Figure 3-22: Slope of decay envelope vs. tip displacement. V_{max}=4x10^{-4}. Passive loss factor varied.

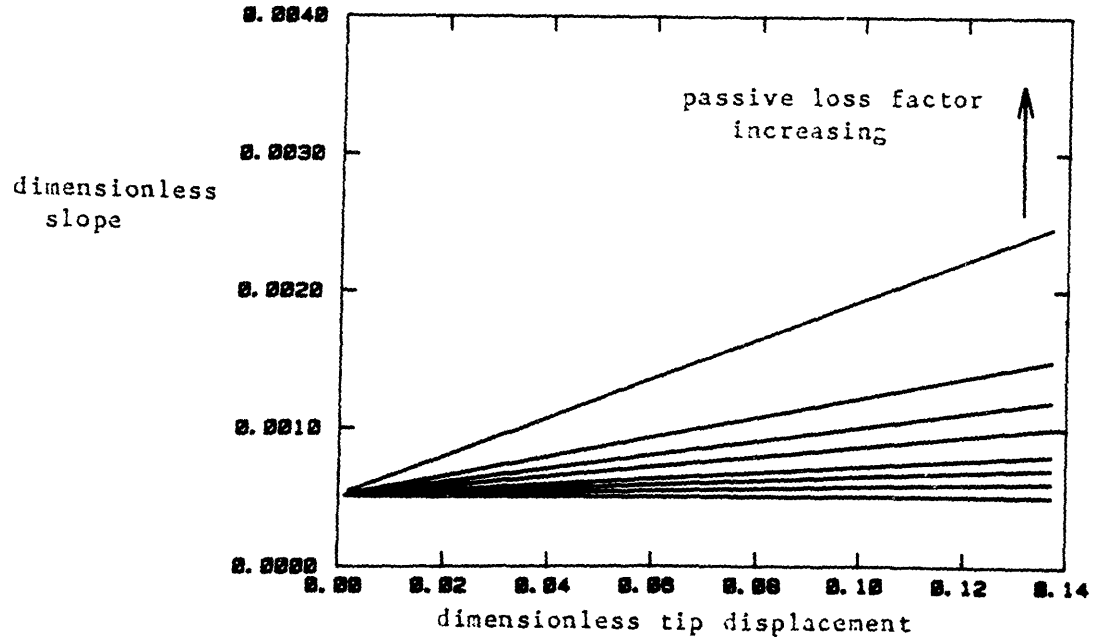

Figure 3-23: Slope of decay envelope vs. tip displacement. V_{max}=8x10^{-4}. Passive loss factor varied.

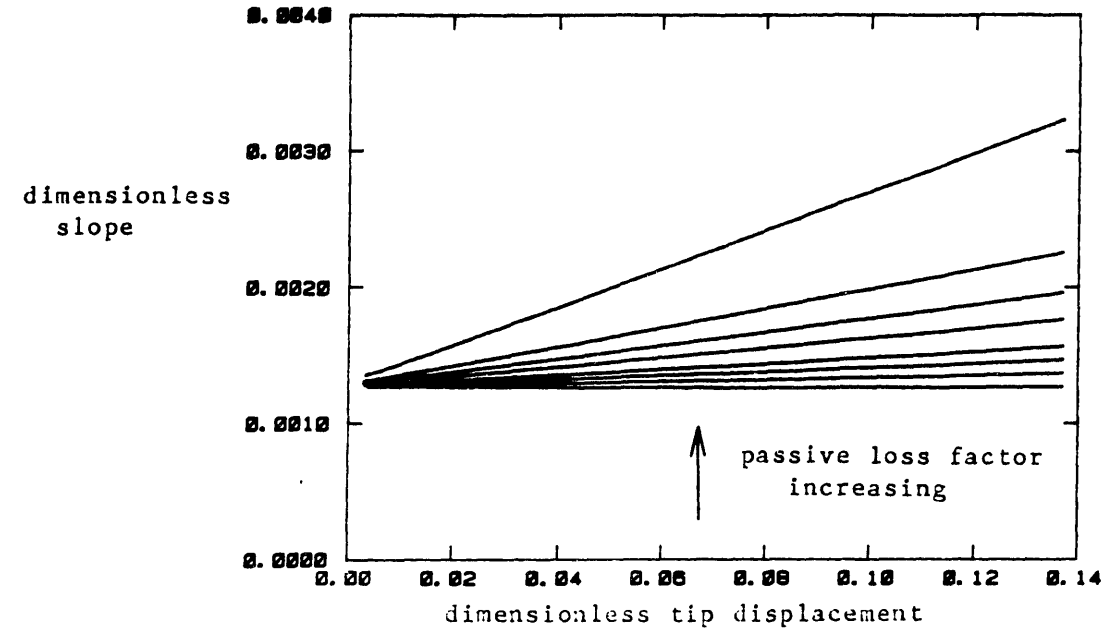

Figure 3-24: Slope of decay envelope vs. tip displacement. V_{max}=2x10^{-3}. Passive loss factor varied.

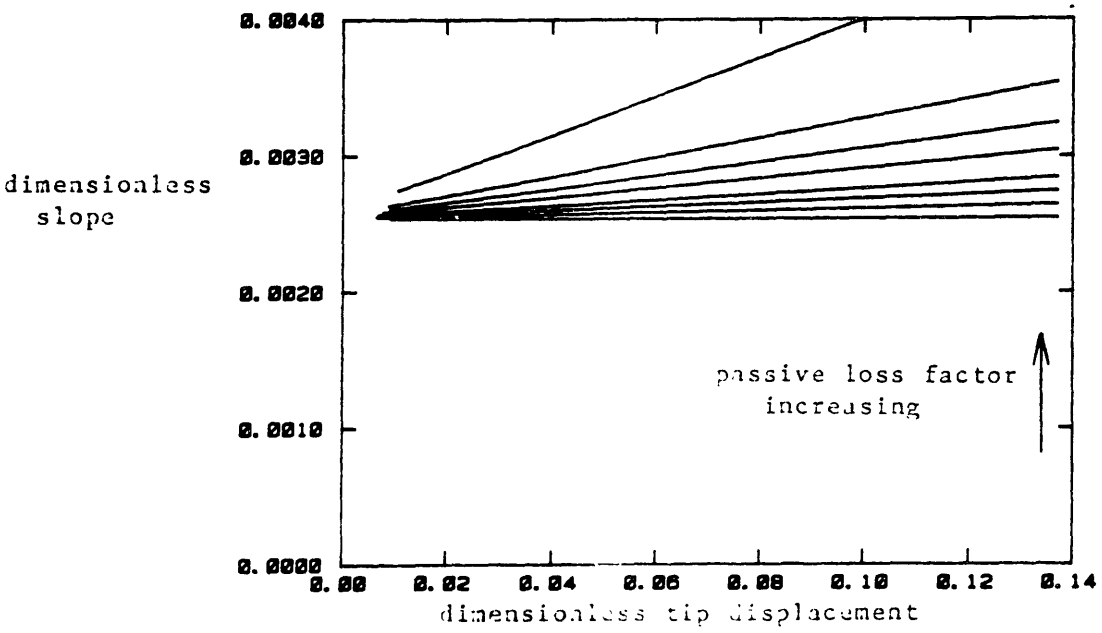

Figure 3-25: Slope of decay envelope vs. tip displacement. V_{max}=4x10^{-3}. Passive loss factor varied.

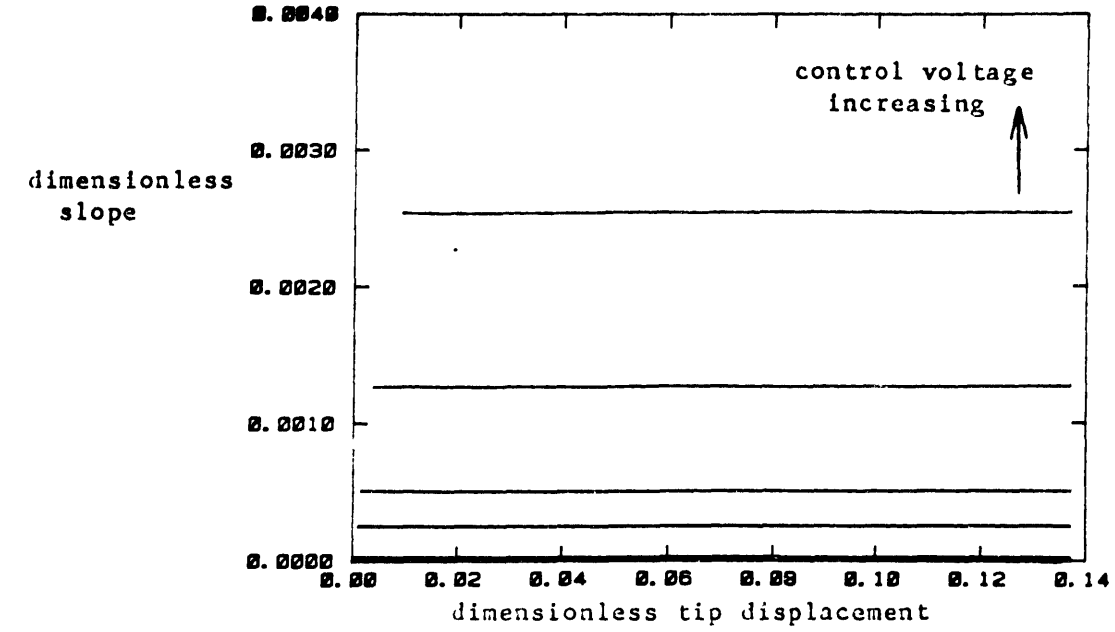

Figure 3-26: Slope of decay envelope vs. tip displacement.
η_p=0.000 . Control voltage varied.

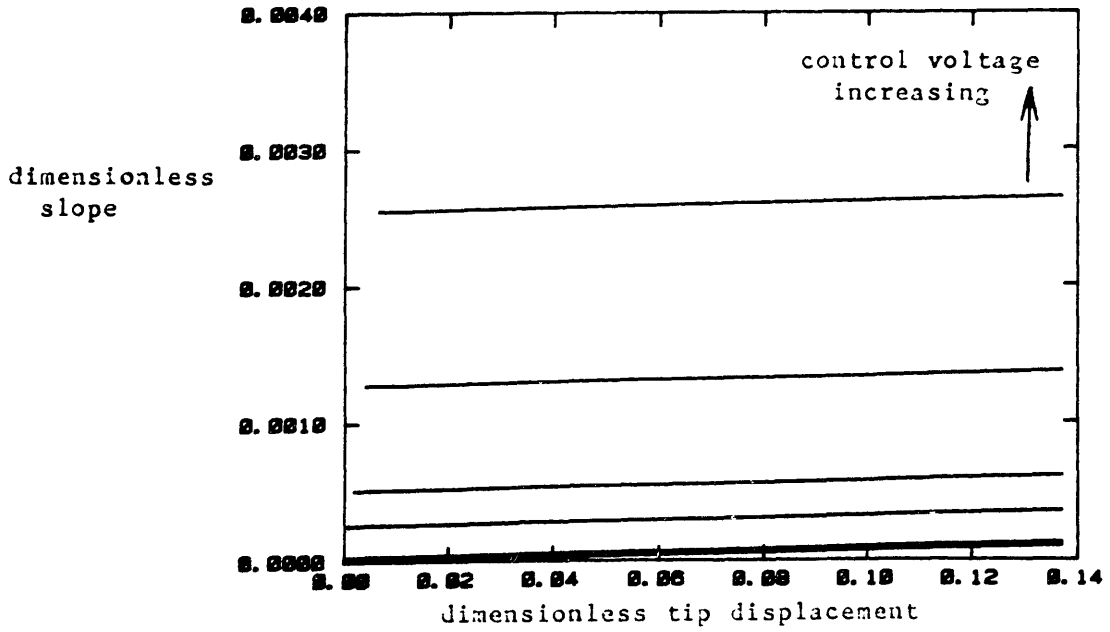

Figure 3-27: Slope of decay envelope vs. tip displacement.
η_p=0.001 . Control voltage varied.

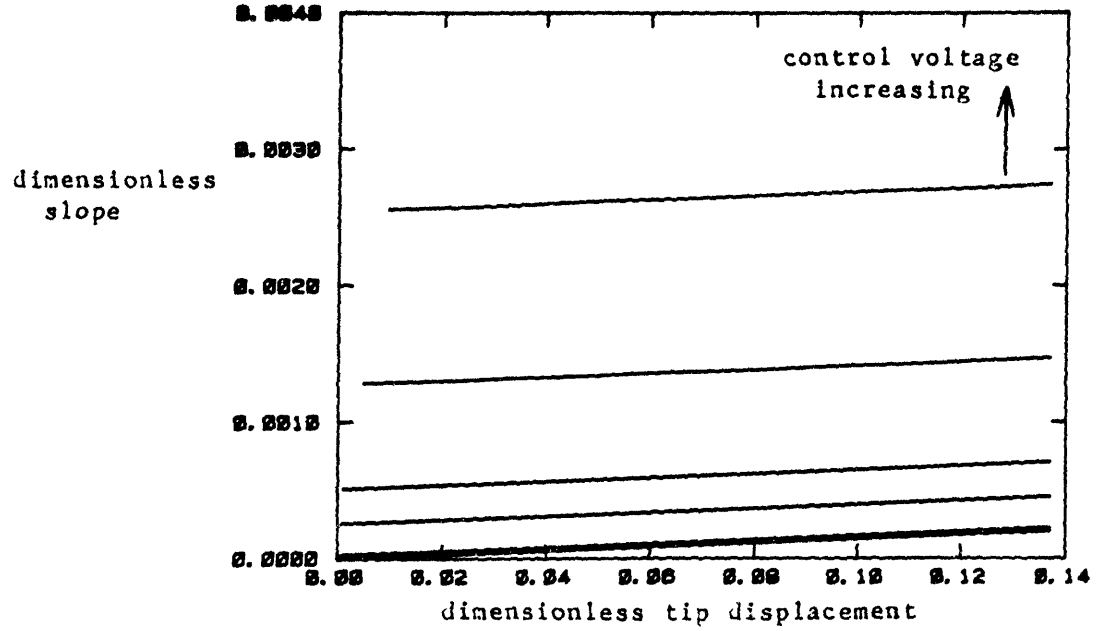

Figure 3-28: *Slope of decay envelope vs. tip displacement.*
η_p=*0.002 . Control voltage varied.*

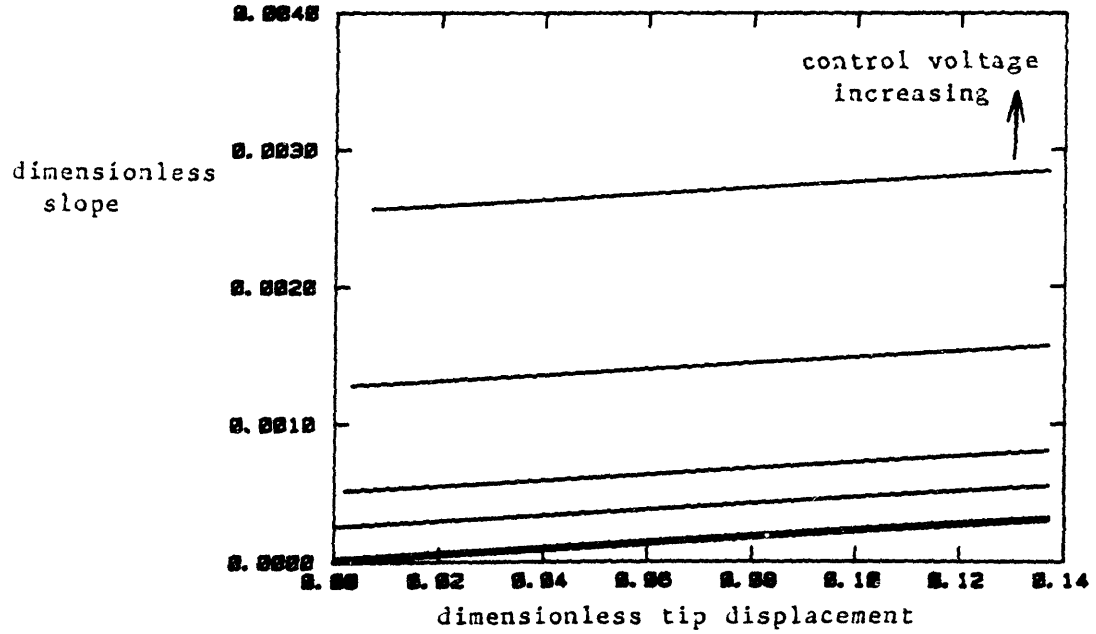

Figure 3-29: *Slope of decay envelope vs. tip displacement.*
η_p=0.003 . *Control voltage varied.*

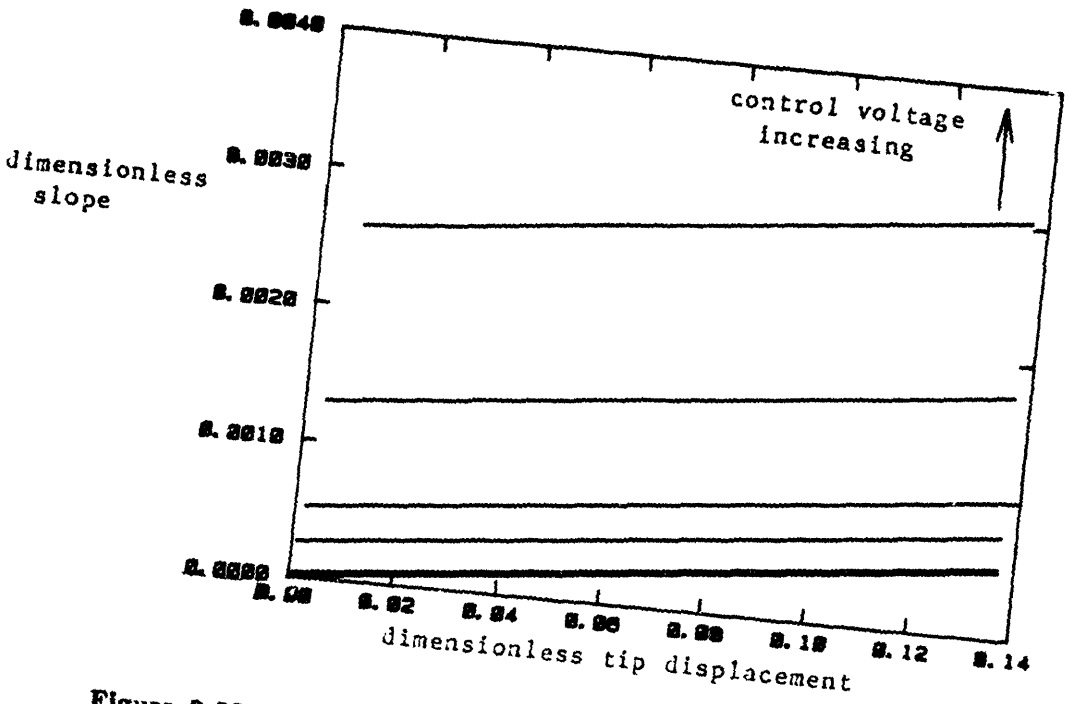

Figure 3-30: Slope of decay envelope vs. tip displacement. η_p=0.005 . Control voltage varied.

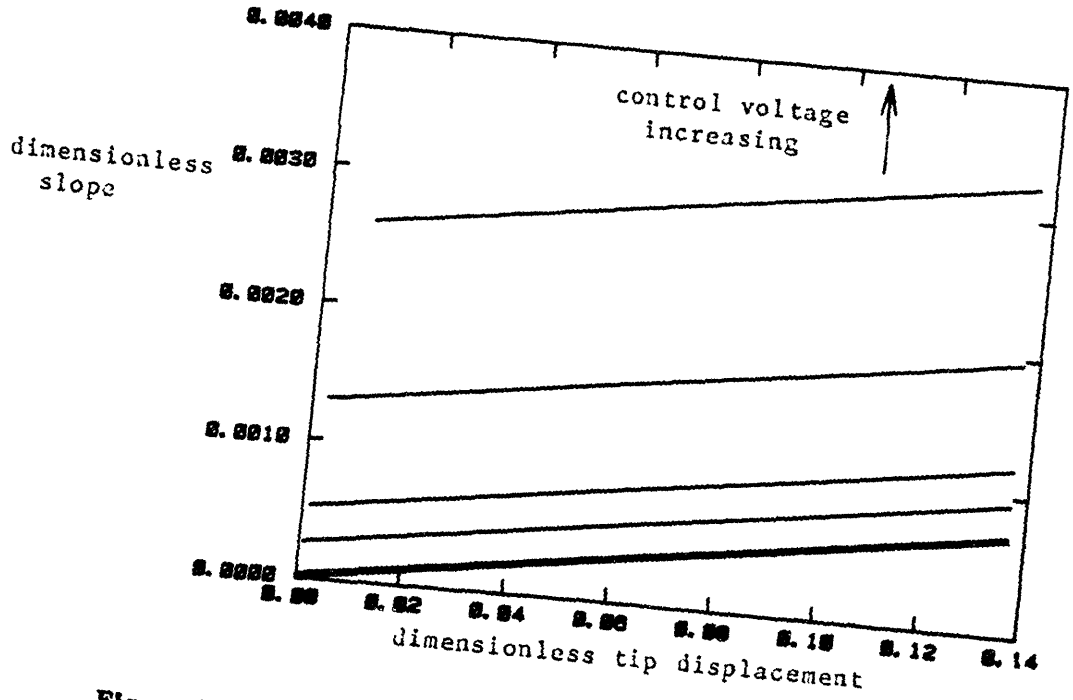

Figure 3-31: Slope of decay envelope vs. tip displacement. η_p=0.007 . Control voltage varied.

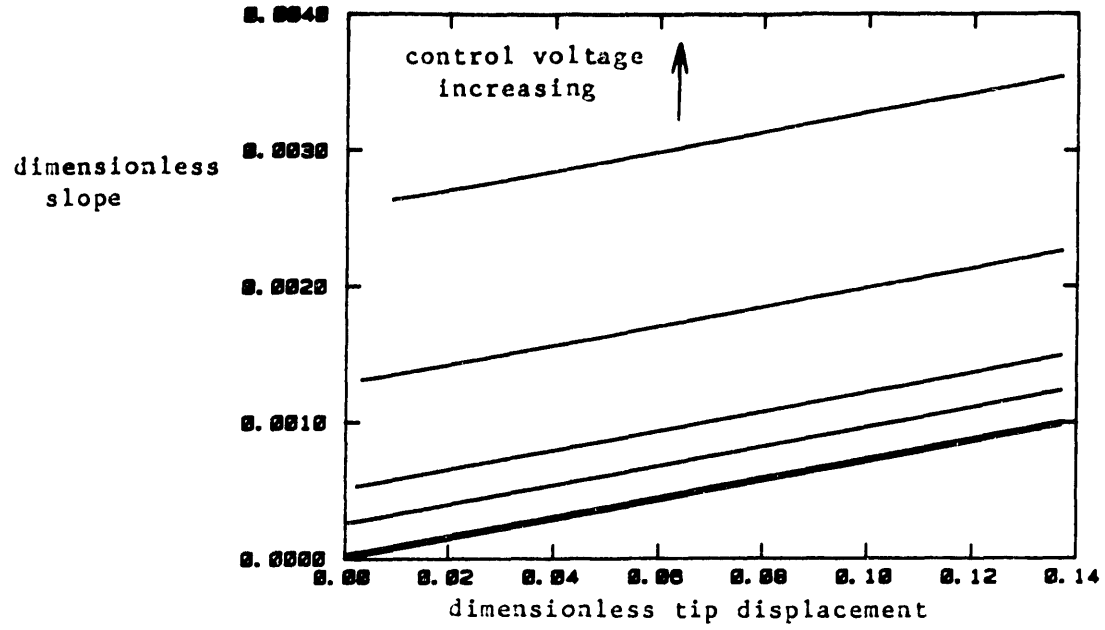

Figure 3-32: Slope of decay envelope vs. tip displacement.
η_p=0.010 . Control voltage varied.

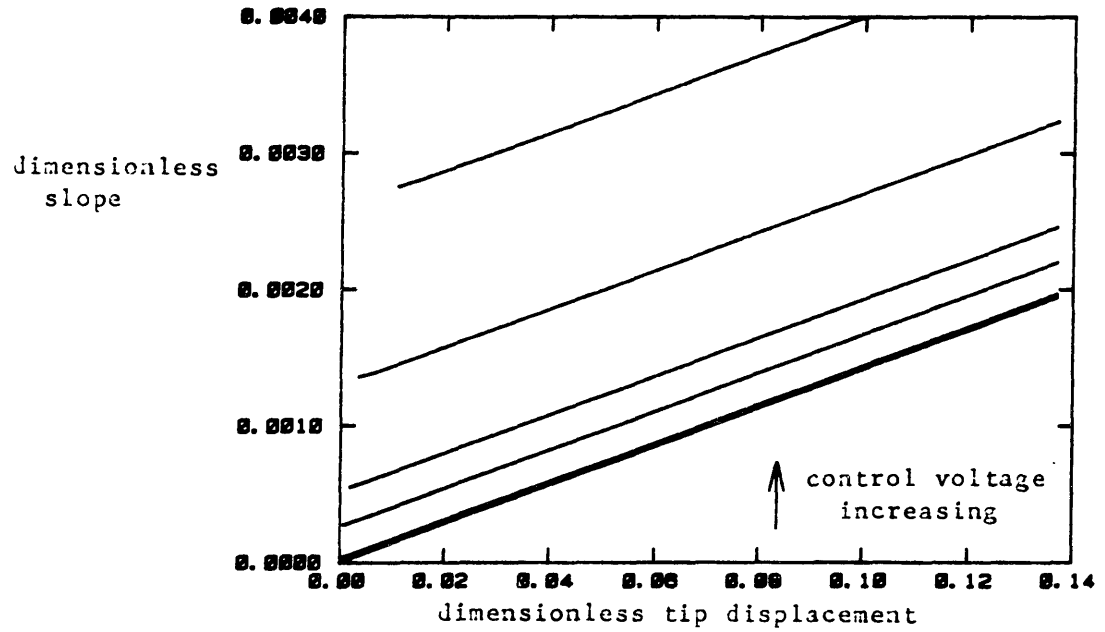

Figure 3-33: Slope of decay envelope vs. tip displacement.
η_p=0.020 . Control voltage varied.

Figures 3-34 through 3-39 show the effective loss factor vs. tip displacement plots for the constant control voltage cases while Figures 3-40 through 3-47 are for the constant passive loss factor cases. The loss factor is plotted on a logarithmic scale. Passive damping provides a constant loss factor which would be a horizontal line on the effective loss factor plots. The effect of the active damping is to increase the effective loss factor from the baseline loss factor of the passive damping. Figure 3-34 shows the cases with $V_{max}=4x10^{-6}$, the smallest control voltage. This figure shows how the passive damping dominates for most of the amplitude range, except for the zero passive damping case. However, even this small control voltage produces a significant increase in the effective loss factor for very small tip displacements. For the case with $\eta_p=0.001$, when the tip displacement has decreased to $d_t=0.001$ the effective loss factor has increased by a factor of 10 over the passive loss factor of $\eta_p=0.001$.

This same effect is present in the cases with higher passive loss factors. The increase in η_{eff} is not apparent until smaller amplitudes. However, just before the amplitude reaches zero, the effective loss factor is nearly independent of the passive loss factor (for the passive loss factors used in this study) and approaches $\eta_{eff}=0.50$ for all values of η_p. This is very impressive considering the control voltage is only $V_{max}=4x10^{-6}$ (1 volt for the scaled beam). As the control voltage is increased, the amplitude at which the active damping becomes dominant increases as well.

The passive loss factor is the baseline loss factor that the active damping increases. This is shown in Figures 3-40 through 3-47 which are the effective loss factor plots for the cases where η_p was held constant and the control voltage was varied. These plots clearly show the amplitudes at which the active damping starts to increase η_{eff} (for a given control voltage and passive loss factor) and how effective an increase in control voltage would be for a given η_p. For example, the cases with $\eta_p=0.010$, shown in Figure 3-46, indicate that a control voltage of $V_{max}=4x10^{-4}$ at least doubles the baseline passive loss factor for tip displacements below $d_t=0.04$. When $\eta_p=0.005$, shown in Figure 3-44, the effective loss factor is at least doubled for tip displacements below $d_t=0.07$ for the same control voltage. The effective loss factor for the case with $\eta_p=0.005$ is lower than that for the case with $\eta_p=0.010$, but the percentage increase in η_{eff} is larger.

The effective loss factor vs. tip displacement plots show some of the tradeoffs between active and passive damping in terms of the effective loss factor of the system. The plots for the constant voltage cases, shown in Figures 3-34 through 3-39, indicate how sensitive η_{eff} is to changes in η_p and what passive loss factor is needed to produce a given η_{eff} for a given

control voltage. Figures 3-40 through 3-47 show the plots for the constant passive loss factor cases and illustrate how sensitive η_{eff} is to changes in the V_{max} and what control voltage is needed to produce a given η_{eff} for a given passive loss factor. These two sets of plots allow one to easily compare different combinations of active and passive damping. Using a parameter study such as this as a design tool, one could go beyond just satisfying a damping criteria and begin to deal with questions such as trading-off the added mass needed to increase the passive loss factor (i.e., viscoelastic damping treatments, etc.) with the added complexity of increasing the power of an active damper.

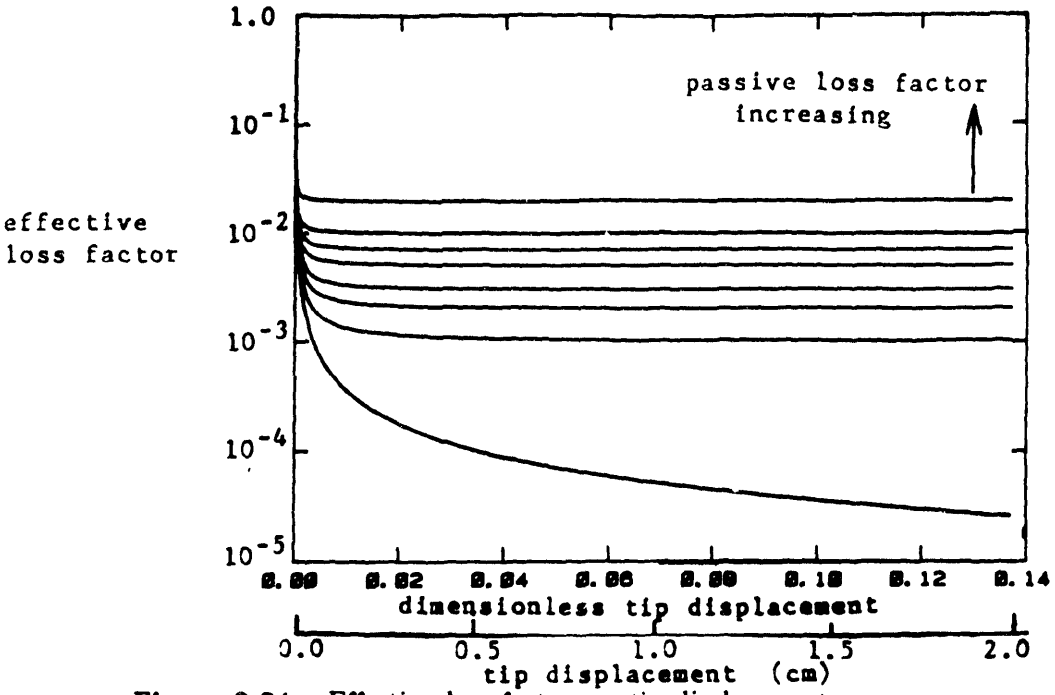

Figure 3-34: Effective loss factor vs. tip displacement.
V_{max}=4x10^{-6}. Passive loss factor varied.

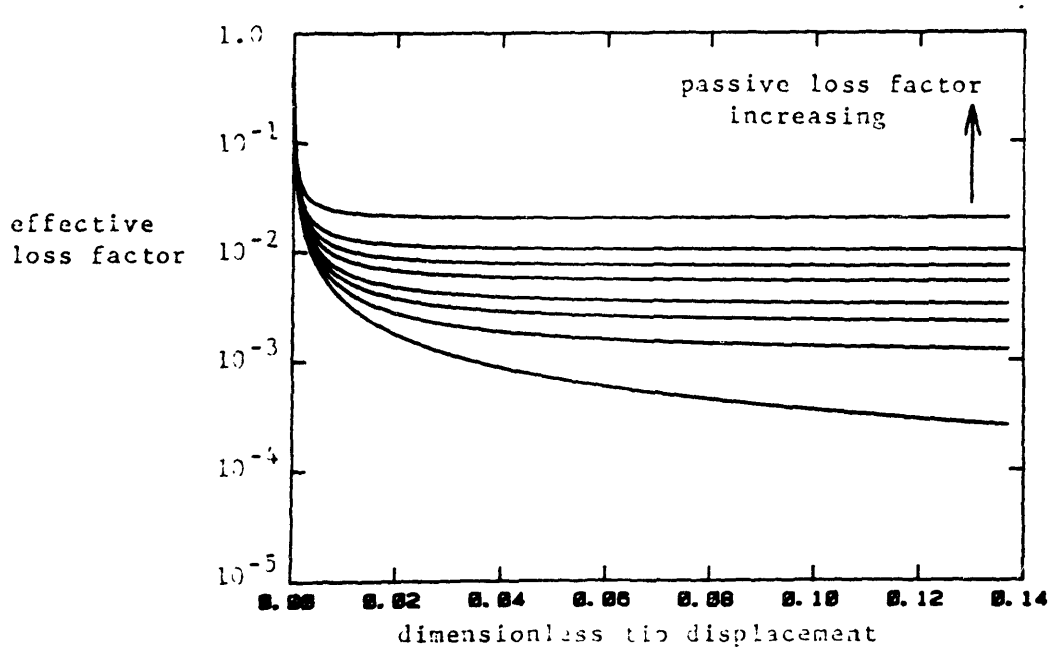

Figure 3-35: Effective loss factor vs. tip displacement.
V_{max}=4x10^{-5}. Passive loss factor varied.

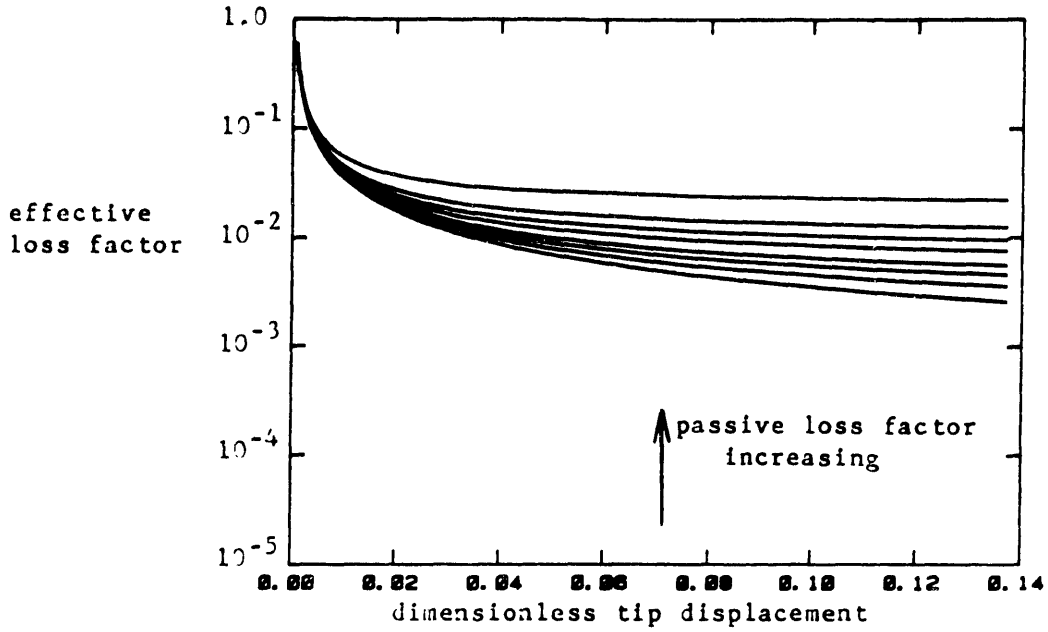

Figure 3-36: Effective loss factor vs. tip displacement.
V_{max}=4x10^{-4}. Passive loss factor varied.

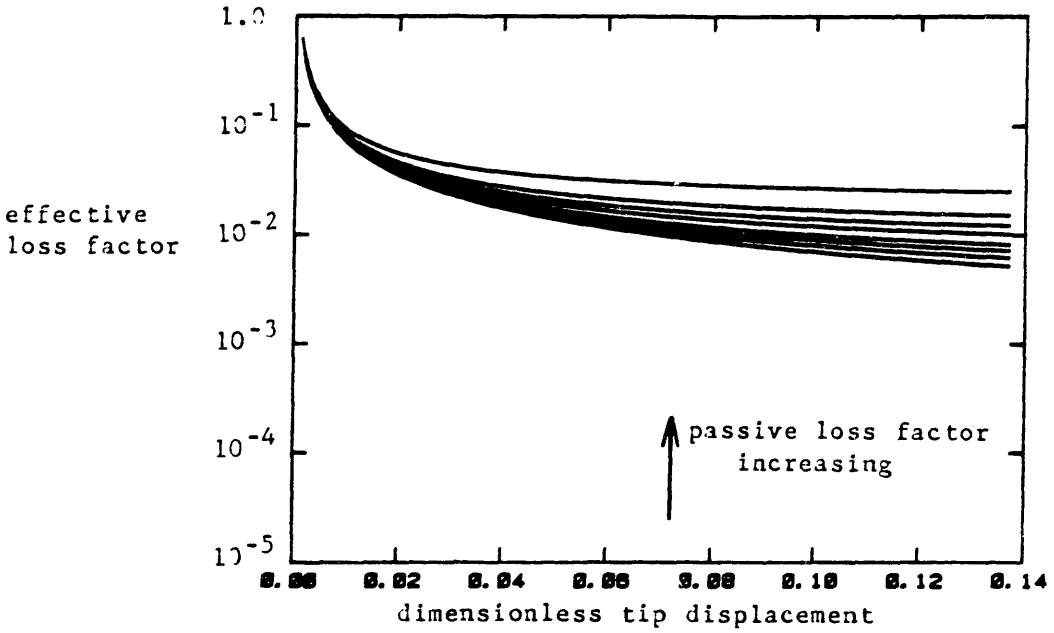

Figure 3-37: Effective loss factor vs. tip displacement.
V_{max}=8x10^{-4}. Passive loss factor varied.

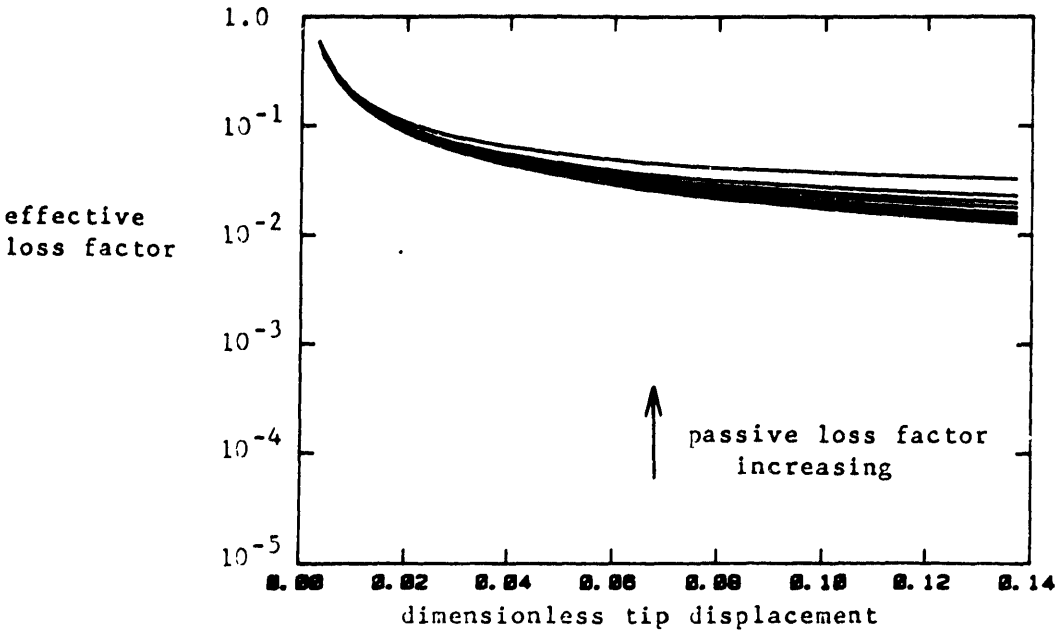

Figure 3-38: Effective loss factor vs. tip displacement.
V_{max}=2x10^{-3}. Passive loss factor varied.

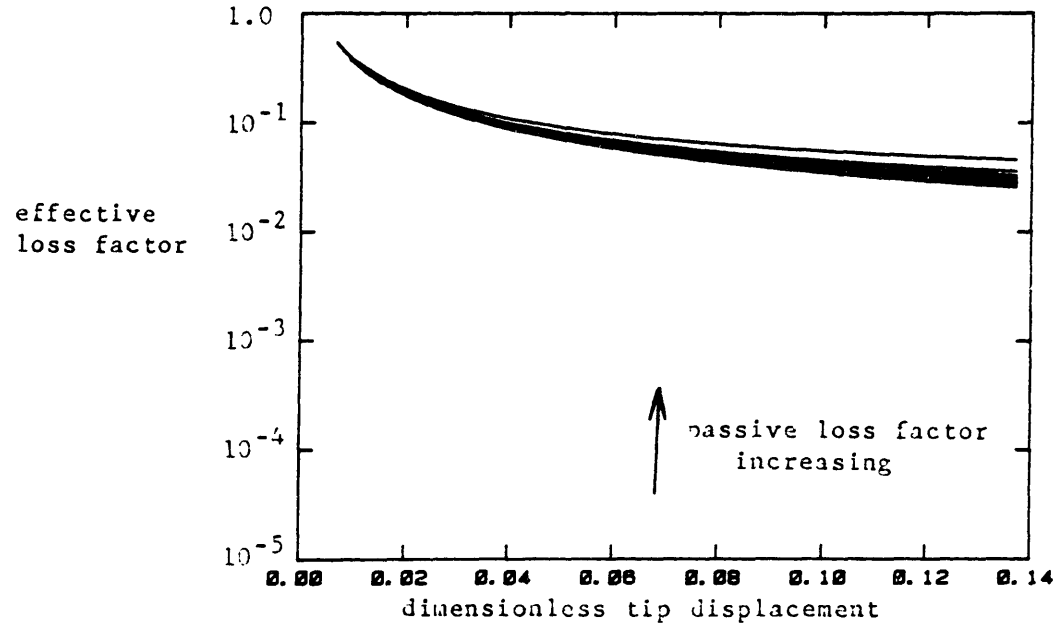

Figure 3-39: Effective loss factor vs. tip displacement.
V_{max}=4x10^{-3}. Passive loss factor varied.

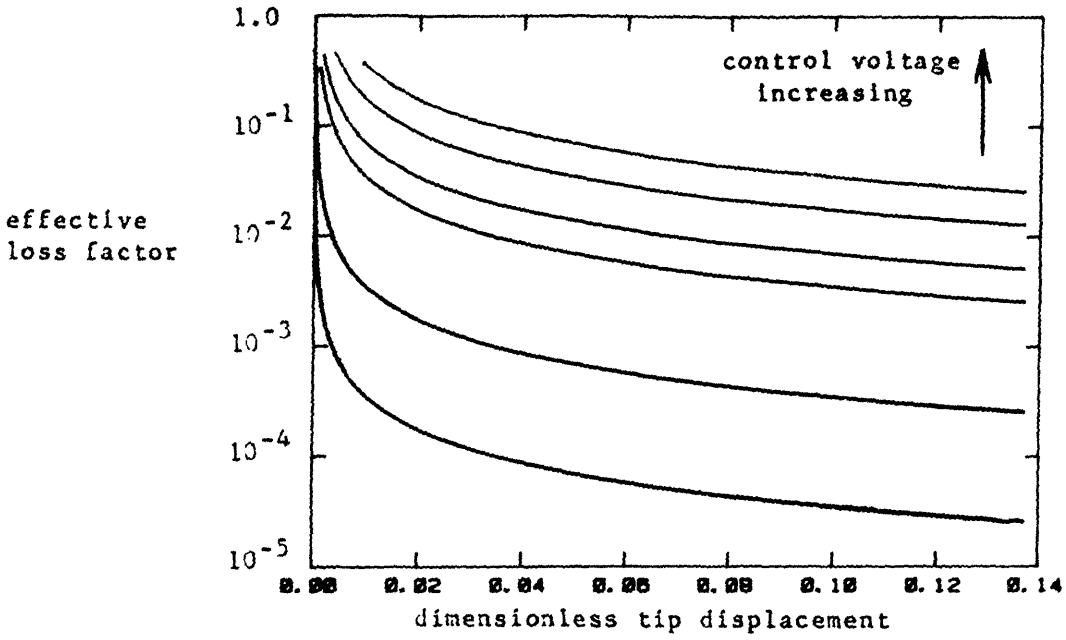

Figure 3-40: Effective loss factor vs. tip displacement.
η_p=0.000 . Control voltage varied.

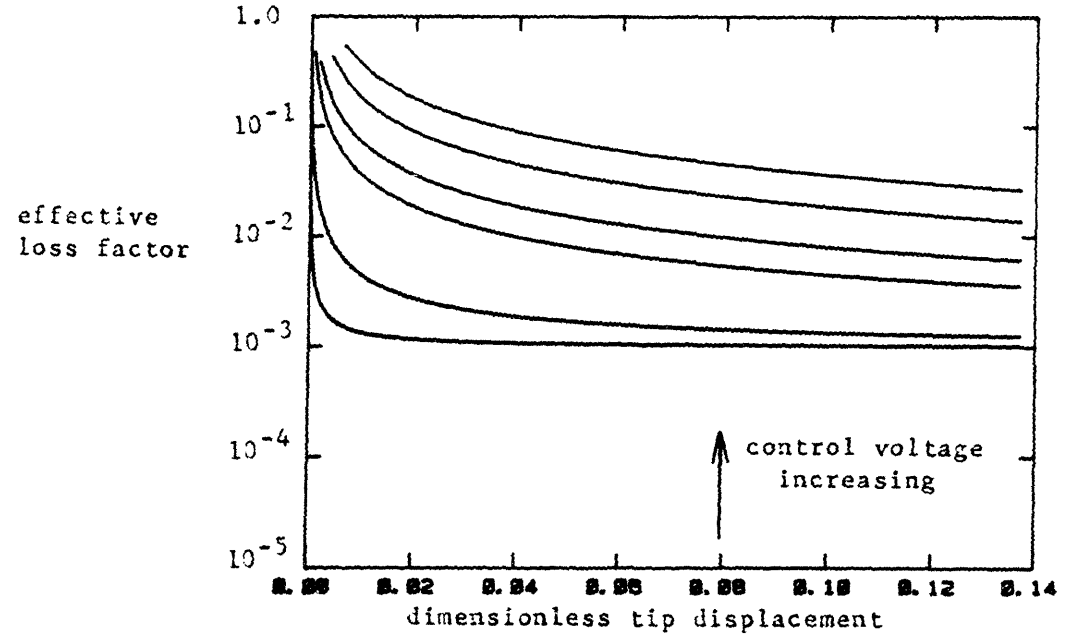

Figure 3-41: Effective loss factor vs. tip displacement.
η_p=0.001 . Control voltage varied.

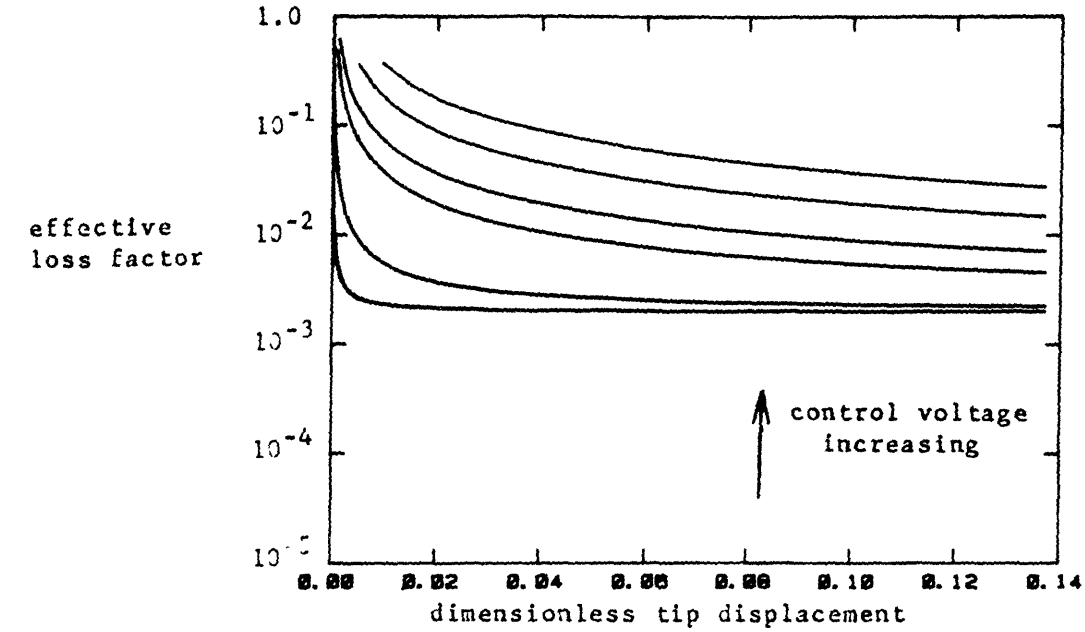

Figure 3-42: Effective loss factor vs. tip displacement.
η_p=0.002 . Control voltage varied.

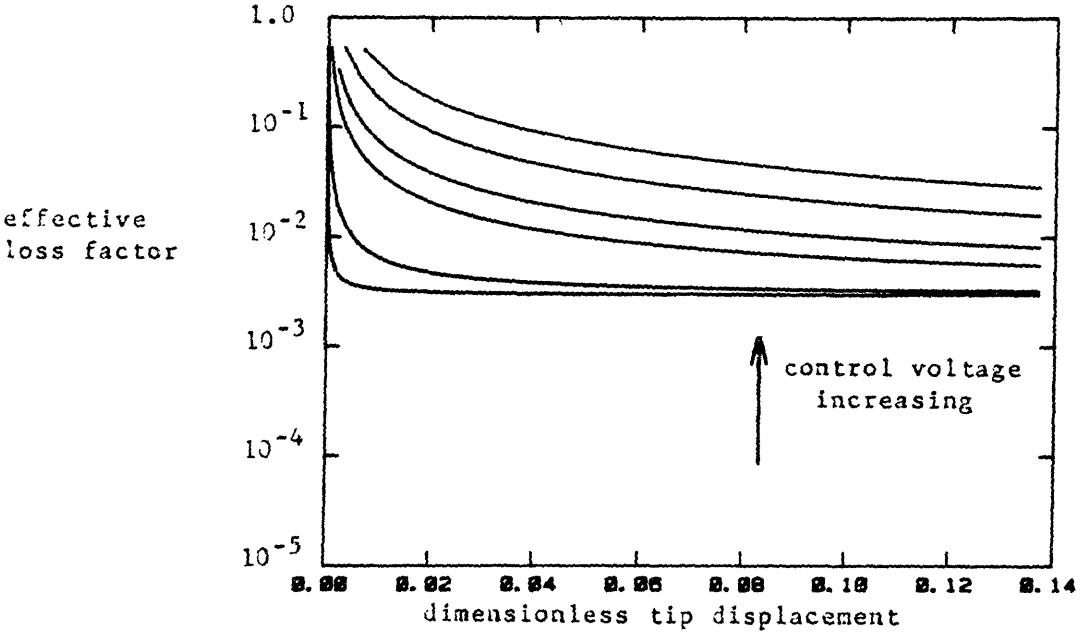

Figure 3-43: Effective loss factor vs. tip displacement.
η_p=0.003 . Control voltage varied.

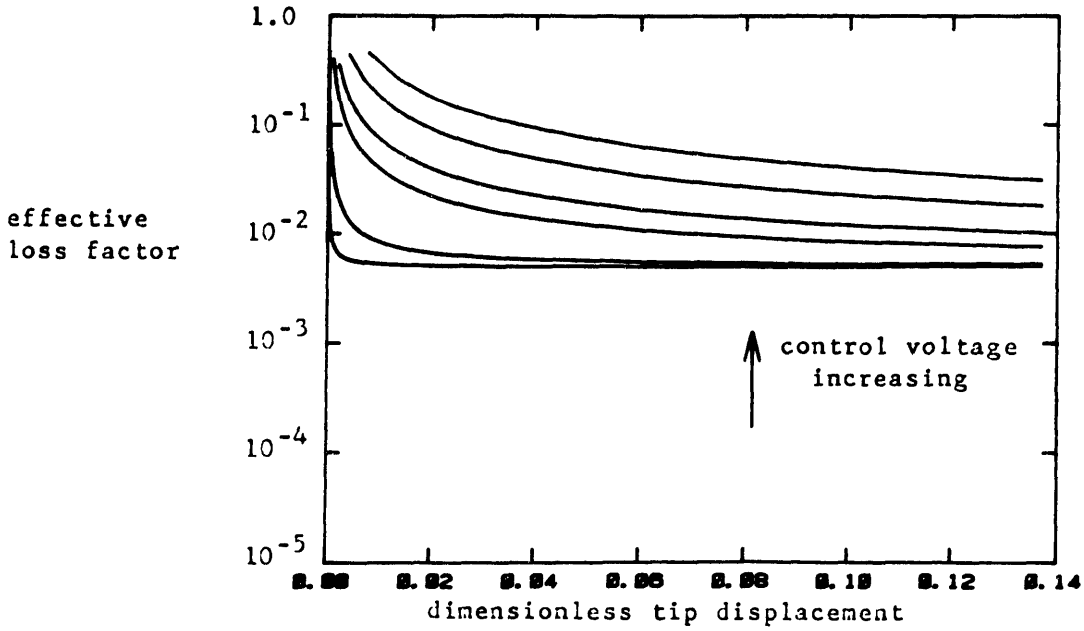

Figure 3-44: Effective loss factor vs. tip displacement.
η_p=0.005 . Control voltage varied.

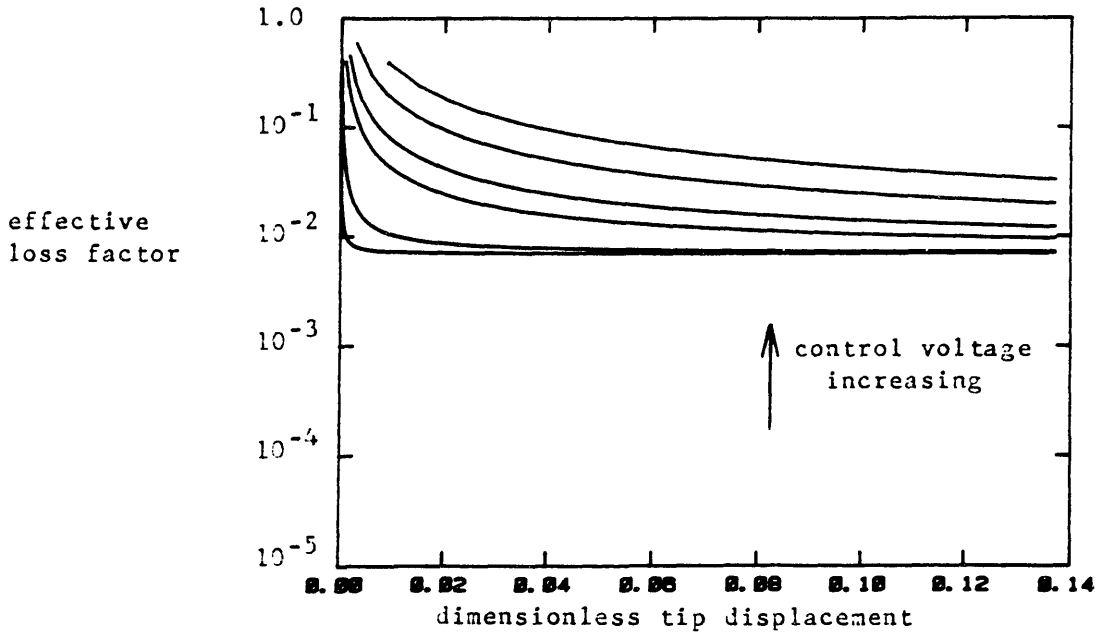

Figure 3-45: Effective loss factor vs. tip displacement.
η_p=0.007 . Control voltage varied.

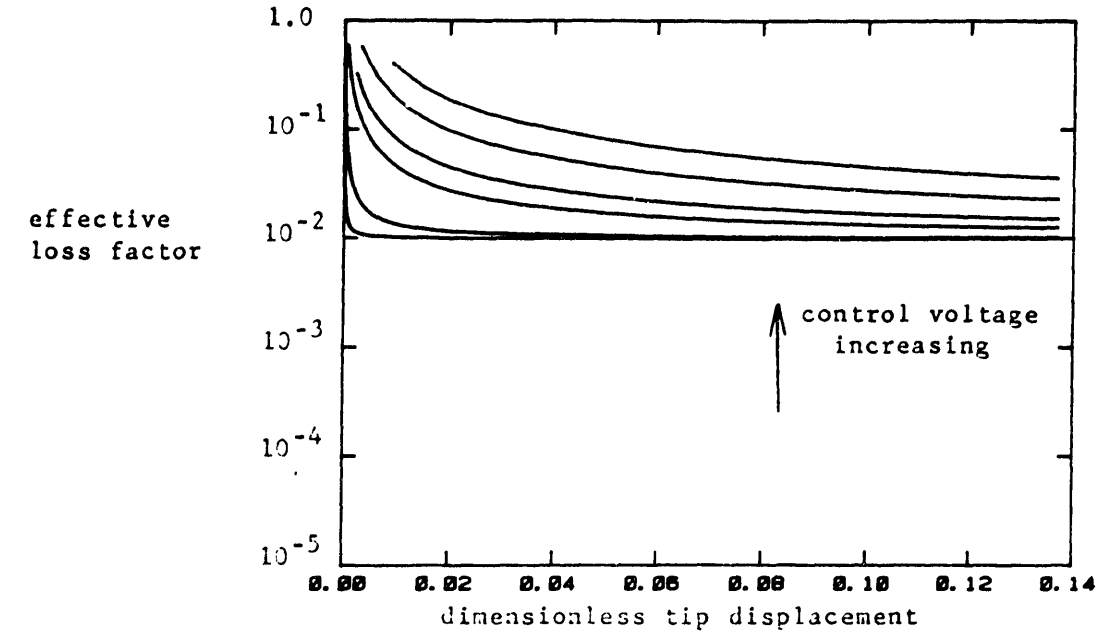

Figure 3-46: Effective loss factor vs. tip displacement.
η_p=0.010 . Control voltage varied.

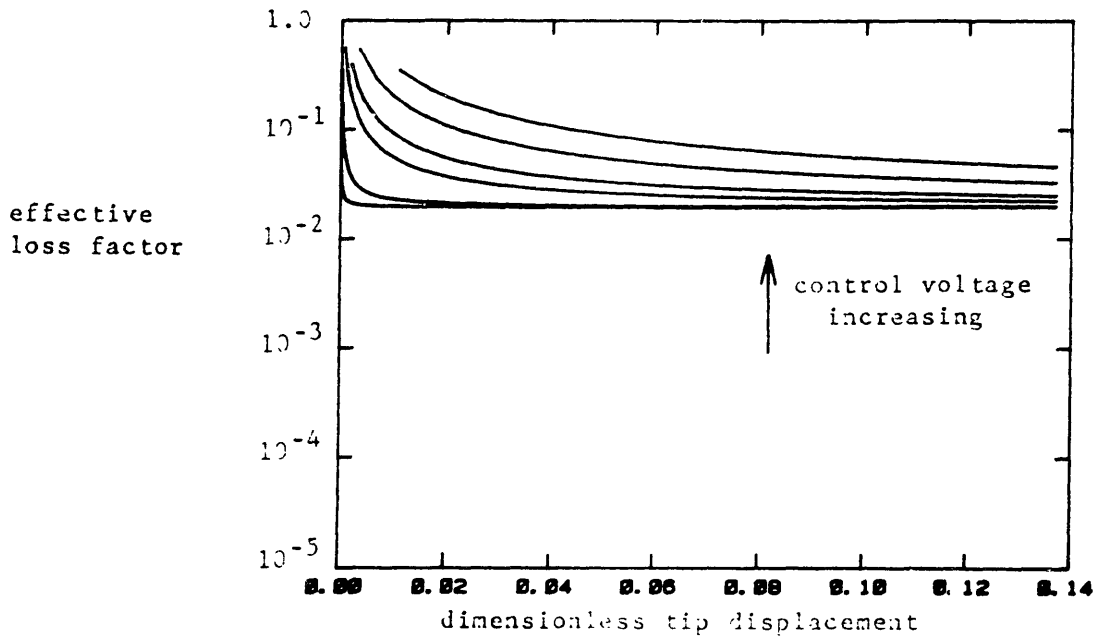

Figure 3-47: Effective loss factor vs. tip displacement.
η_p=0.020 . Control voltage varied.

Chapter 4
Experimental Analysis

This chapter presents the result of the experimental testing of the active damper. Section 4.1 describes the construction of the damper and the testing fixtures. Section 4.2 presents the measuring of the torque constant, the baseline impact tests, and the free decay tests, all performed using the stationary fixture. Section 4.3 describes the continuous excitation tests performed using the shaker fixture. All results in this chapter are reported using dimensional values, i.e., they have not been non-dimensionalized.

4.1 Construction of Scaled Test Structure and the Active Damper

4.1.1 Scaled Beam and Active Damper Construction

The choice of beam material and dimensions is discussed in Section 2.2. Table 2-II summarizes the final design parameters for the scaled beam. Figure 4-1 shows a schematic of the cantilever beam with both the tip mass and PVF_2 attached and the fixture used for stationary testing. The beam was made from a piece of steel feeler stock, 0.381 mm (0.015 in) thick, 1.27 cm (0.5 in) deep (or wide), and 30.5 cm (12. in) long. The flexible length of the beam was changed by adjusting the location at which it was clamped in the fixture. The other dimensions were not changed.

The tip mass consists of a 2 gm accelerometer (Bruel & Kjaer model 4344) and square (1.27 cm, .5 in. on a side) pieces of shim stock. A 0.3 gm mass allowance was made for the accelerometer cable connector. The steel shim stock was 0.381 mm (0.015 in) thick while the brass was 0.635 mm (0.025 in). The shim stock was epoxied to the beam. A smaller piece of shim stock was used to adjust the tip mass to 6.7 $\pm$0.1 gm. A detail of the tip mass is shown in Figure 4-2. The weights were placed so that nearly half of the mass would be on each side of the beam, i.e., so that the center of gravity of the tip mass would be close to the midplane of the beam. This helps to inhibit any torsional coupling.

No attempt was made to achieve the correct tip inertia. However, an estimate of the tip inertia was made using basic mechanics. The accelerometer was treated as a cylinder of

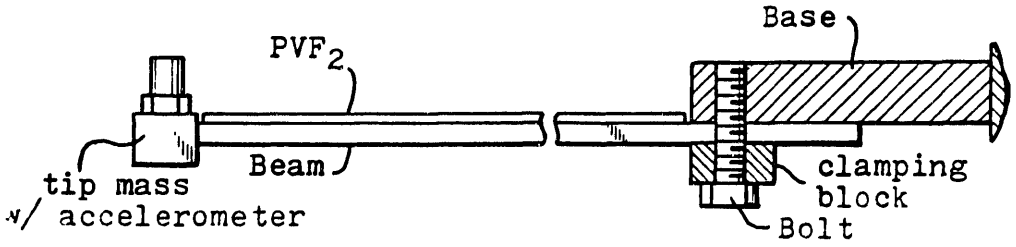

(a). Top view of beam in stationary fixture.

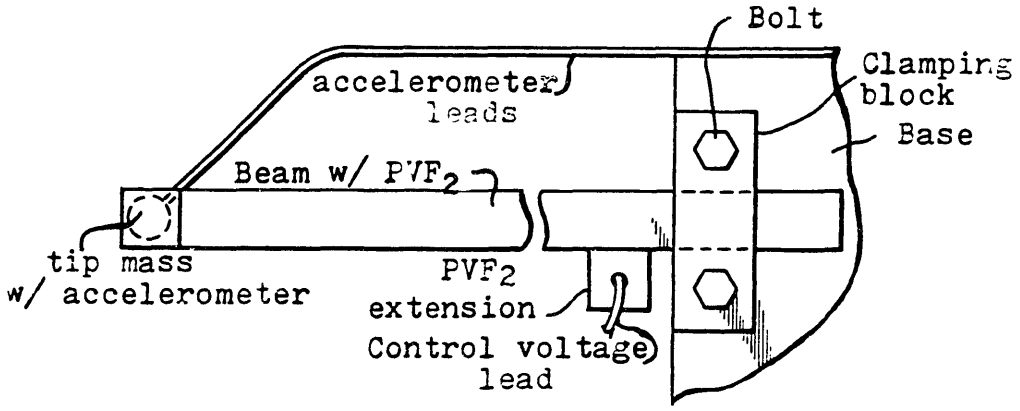

(b). Side view of beam in stationary fixture.

Figure 4-1: Schematic of the active damper in stationary fixture.

uniform density and the density and dimensions of the other elements of the tip mass are known. The centroidal moment of inertia was calculated for each element and the parallel axis theorem was used to find the inertia about the tip of the beam. (Point A in Figure 4-2). The estimated tip inertia was 4.4 g·cm^2 compared with 4.98 g·cm^2 called for by the dynamic scaling. This error was considered acceptable for the development work.

The PVF_2 used for the active damper was uniaxially polarized and was 25 μm (10^{-6}m)

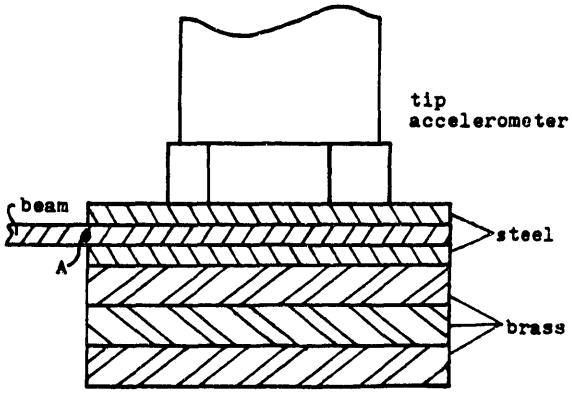

Figure 4-2: Detail of tip mass.

thick. A layer of PVF_2 was bonded to the steel beam using Eccobond 45LV, a low viscosity, high strength, two-part epoxy. The PVF_2 covered an entire side of the beam. A thin film of the epoxy was applied to the steel beam with a razor blade and the PVF_2 was placed on top of the epoxy. Care was taken to insure that air bubbles weren't trapped under the PVF_2, that the PVF_2 was seated well in the epoxy, and that the nickel plating on the PVF_2 was not rubbed off. The layers were then clamped together until the epoxy had set (overnight). The thickness of the epoxy layer ranged from 5 to 15 μm.

The PVF_2 layer included an extension below the beam where the input voltage leads would be attached. The face of the PVF_2 next to the beam was always grounded, as was the beam and the fixture, for safety reasons. The control voltage was applied to the outer face (away from the beam) of the PVF_2. The lead wires were soldered to copper foil tabs and the tabs were clamped against the appropriate face of the PVF_2. This was found to be the most reliable and convenient method of attaching the leads for the development work. Other methods of attaching the leads are being investigated.

Eventually, due to vibration and wear, the nickel plating on the extension was either removed or cracked so that there was no electrical continuity between nickel on the extension and that on the rest of the PVF_2. Rather than remove the PVF_2 and apply a new layer, the control voltage lead was clamped to the outer face of the PVF_2 near the root of the beam. The ground lead was attached directly to the beam. Since the piezoelectric strain is induced by a field, not the charge or voltage directly, this lead configuration worked well

even if the inner face of the PVF_2 did not make contact with the beam. The field produced between the beam and the outer face of the PVF_2 is only slightly weaker (for a given voltage) than the field between the two faces of the PVF_2 due to the thickness of the adhesive layer.

The leads to the accelerometer were made from a pair of small wires shielded inside a layer of aluminum foil and were extended above the beam from the clamping fixture to the accelerometer at the tip. (See Figure 4-1.) This lead configuration was necessary because conventional accelerometer cables were too stiff and massive and hence greatly affected the motion of the beam. However, the electrical noise was greatly increased. The aluminum foil made a good shield from electric fields, but relative motion between the shield and the conductors inside had charge coupling or triboelectric effects. This was a major source of noise, especially during the continuous excitation testing when the fixture was excited with random noise. Other types of cables and different types of accelerometers are being considered to alleviate this problem.

Table 4-I is a summary of the parameters for the active damper. These are the values that were used in the parameter study (Section 3.5).

4.1.2 Fixture Construction

When measuring the mechanical behavior of a system, it is important that the fixture or support does not absorb much energy from the system, or otherwise affect its behavior. For a cantilever beam this means that the clamping fixture should be as rigid as possible. The fixture used for the stationary tests is shown with the beam in Figure 4-1. The base was made from 9.5 mm (0.375 in) thick aluminum angle stock attached to a base plate that was clamped to the work table. A horizontal slot 1.3 cm (0.5 in) wide and .13 mm (0.005 in) deep in the side of the base insured that the beam was clamped in a horizontal position. The clamping block was made from 1.3 cm (0.5 in) aluminum stock and was bolted to the base. The faces of the base and the clamping block that contact the beam were milled to insure uniform clamping. The edges of the base and the clamping block that form the root of the beam were also milled to insure that the root was perpendicular to the longitudinal axis of the beam.

The fixture for the continuous excitation testing was very similar except that the base was made from 2.5 cm (1.0 in) aluminum stock which was bolted to an electrodynamic

Table 4-I: Parameters for the Active Damper.

	Scaled model	PVF_2
material	steel	-
modulus, E (Nm^{-2})	$210x10^9$	$2.0x10^9$
density, ρ (kgm^{-3})	7800	1800
length, l (m)	0.146	0.146
thickness, h (mm)	0.381	$28x10^{-3}$
depth, b (cm)	1.27	1.27
tip mass, M_t (kg)	$6.73x10^{-3}$	-
tip inertia, I_t (kgm^2)	$4.4x10^{-7}$	-
static piezoelectric constant, d_{31} ($m \cdot V^{-1}$)	-	$22x10^{-12}$

shaker. The clamping block was larger to allow the mounting of a 500 gm accelerometer to monitor the vibrations of the base of the beam.

4.2 Stationary Fixture Tests

This section presents the results of three different tests performed using the stationary fixture. The first test was measuring the torque constant, c, for the active damper. The second test was to determine the baseline behavior of the beam using impact testing. The third test was to apply the constant-gain and constant-amplitude controllers to the free decay of the first mode of vibration.

4.2.1 Measuring the Torque Constant

The torque constant, c, represents the torque produced per unit volt of control. Preliminary simulation results for the free decay of the first mode indicated that the active control was nearly 3 times more effective than predicted. The simulation depends on five parameters: the control voltage, the torque constant, the modal energy per unit tip displacement, the tip angle per unit tip displacement, and the passive damping in the system (see Section 3.4). The passive damping had been measured in the baseline tests and the voltage was monitored during the free decay tests so these parameters were assumed accurate. Since the first mode shape of a cantilever is much like the deformed shape of a cantilever with a normal load at the tip, the modal energy and the tip angle could be estimated with basic mechanics [29]. The modal energy was estimated by treating the cantilever as a spring and determining the energy stored when a normal force at the tip is applied. The tip angle for the first mode was estimated by determining the tip angle due to a normal force. When compared with the estimates, the values calculated from the mode shape agreed to within one percent. This left the torque constant as the most likely source of error, so it was decided to experimentally determine the torque constant.

The relation between tip displacement and the torque applied at the end of a cantilever can be found from basic mechanics [29]. For a torque, T, applied at the tip, the tip displacement of a cantilever beam, d_t, is given by

$$d_t = \frac{T\,\ell^2}{2EI} \tag{4.1}$$

where EI is the stiffness of the composite beam and ℓ is its length. Substituting for the torque, T, from the relation that defines the torque constant, Eqn. (3.6), and solving for the torque constant, c, yields

$$c = \frac{d_t}{V} \cdot \frac{2EI}{\ell^2} \quad . \tag{4.2}$$

By measuring the tip displacement per volt, one can determine the effective torque constant.

The apparatus used for this measurement is shown in Figure 4-3. A DC power supply was used to apply a voltage to the PVF_2. The resulting torque produced a tip displacement which was measured using a Fotonic^{TM} sensor (MTI Model KD-45). A Fotonic^{TM} sensor measures the distance to a target by emitting light from half of the fibers in a fiber optic bundle, and receiving the light that is reflected from the target in the other half. The

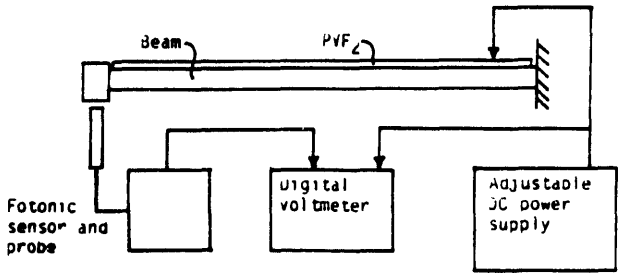

Figure 4-3: Schematic of apparatus used to determine the effective torque constant.

amount of light reflected is related to the distance from the target. This reflected light signal is converted to a voltage which is measured.

The measured relation between tip displacement and applied voltage was 3.0×10^{-7} m·V^{-1}. Using this value in Eqn. (4.2) and the nominal values of l and EI yields

$$c = 3.4 \times 10^{-7} \text{ NmV}^{-1} \quad . \tag{4.3}$$

Compared with the nominal value of the torque constant of $c = 1.2 \times 10^{-7}$ Nm·V^{-1} (calclulated from Eqn. (3.6)), the measured torque constant is nearly 3 times that predicted by the nominal value. This accounts for most of the discrepancy found between the preliminary simulations and the free decay results. One possible explanation for the difference between the measured and predicted torque constants is the epoxy layer in the composite beam. This layer was not modeled in the equations of motion and increases the moment arm between the midplane of the PVF_2 layer and the neutral axis of the composite beam. Another explanation may be that the d_{31} piezoelectric constant is actually higher than the nominal value, resulting in a higher torque. The measured torque constant was used in Section 3.5 to non-dimensionalize the voltages for the parameter study.

4.2.2 Impact Testing

Impact testing was used to identify the natural frequencies and modal damping of the first three modes of the cantilever beam without the active damper attached. A schematic of the apparatus used in this testing is shown in Figure 4-4.

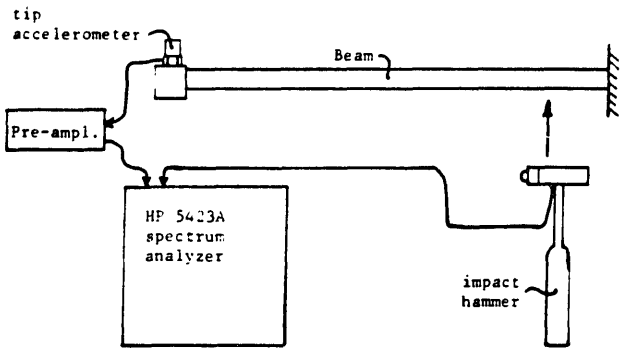

Figure 4-4: Schematic of apparatus used for impact testing.

A spectrum analyzer (HP model 5423A) was used to measure the transfer function between a force impulse from an impact hammer near the root of the beam as the input and the tip acceleration as the output. Band selectable analysis, or the zoom technique, was used to increase the frequency resolution by centering the analysis band around a resonant frequency. All of the final measurements were taken with a frequency resolution of 0.1 Hz. A typical transfer function taken centered around the first resonance is shown in Figure 4-5. Neither the accelerometer nor the impact hammer were calibrated because only the resonant frequency and the modal damping were of interest. The modal damping depends only on the shape of the transfer function near a resonance, not the magnitude. The calibration gains only affect the magnitude of the transfer function, not the shape.

The spectrum analyzer applied a curve fit to the experimental data points near a resonance and used the half power bandwidth method on the fitted curve to determine the modal damping. The same procedure could have been performed manually, but by comparing the accuracy of the two methods, it was found that the spectrum analyzer was more accurate due its curve fitting routine. Table 4-II summarizes the results of the impact testing for the

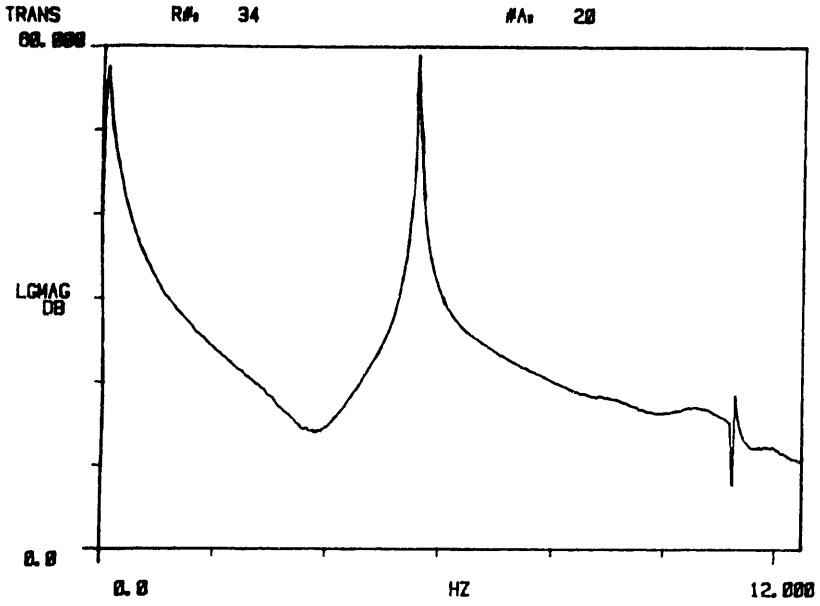

Figure 4-5: Typical transfer function from impact tests (first mode).

Table 4-II: Impact Test Results.

Mode #	Frequency (Hz)	Passive loss factor
1	5.6	0.001
2	59	0.002
3	180	0.002

first three modes of vibration. These damping values are for low level vibration since the impact testing did not excite high levels of vibration. The modal damping for each of the modes was very small, on the order of the structural damping in the steel itself [28]. This gave confidence that the fixture was indeed rigid and that the accelerometer cables were not significantly affecting the motion of the beam. Also, the measured natural frequencies match fairly closely the ones predicted in Appendix B.

4.2.3 Free Decay Testing

4.2.3.1 Apparatus and Procedures

The constant-gain and constant-amplitude control laws derived in Section 3.3 were used to actively damp the free decay of the first mode of vibration of the composite beam. (A controller to implement the Lyapunov control law is currently being assembled.) A schematic of the equipment used for this testing is shown in Figure 4-6.

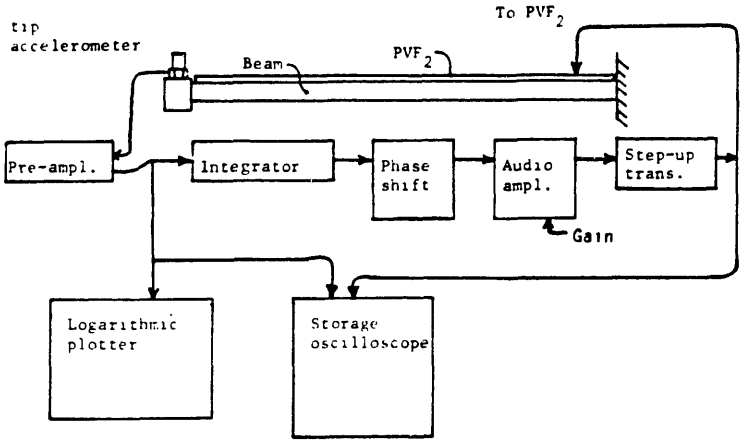

Figure 4-6: Schematic of apparatus used for free decay testing of the active damper.

The tip accelerometer signal was integrated to give tip velocity, phase-shifted, amplified through an audio amplifier and a step-up transformer, and applied to the PVF_2. The overall gain of this feedback loop was determined by adjusting the gain of the audio amplifier. The first mode of the composite beam was near 5.6 Hz, much below the linear region of an audio amplifier, so the additional phase shift is necessary to correct for the phase shift through the audio amplifier. The phase-shifting was done using a continuously variable filter set. The poles of the filter were adjusted to provide the appropriate overall phase shift at the resonant frequency ($\pm$90 degrees, depending on the polarity of the PVF_2 layer). The most reliable way to adjust the phase shift around the feedback loop was to replace the accelerometer signal with a random noise signal and use the spectrum analyzer to measure the transfer function between the noise input and the feedback voltage output. The poles of the filter set were adjusted until the phase of the transfer function was correct at the resonant frequency of

interest, in this case the first mode.

The storage oscilloscope was used to record the feedback voltage and the tip acceleration. However, the acceleration is scaled as needed and reported as tip displacement. This is valid because the system is operating in a nearly linear regime and is useful because tip displacement is easier to visualize than acceleration. The same scaling was done for the logarithmic plotter.

The logarithmic plotter was used to plot the decay envelope on a logarithmic scale because the damping of the system is related to the slope of the decay envelope on a logarithmic plot, as discussed in Appendix D. The plots allowed both a qualitative and quantitative look at how the damping changed with time. This was especially helpful with the nonlinear feedback of the constant-amplitude controller.

The test procedure was to impose an initial condition of 2 cm tip displacement by touching only the tip of the beam, release it, and observe the decay envelope. Using this procedure, very little of the second and higher modes were introduced in the initial conditions. For the constant-gain controller, the gain was set so that the maximum voltage amplitude would not exceed the voltage limit, V_{max}. The maximum gain allowed was easily determined experimentally since the maximum voltage occured when the beam was first released. For the constant-amplitude controller, the initial gain was determined in the same manner, but the gain was increased after the beam was released to keep the amplitude of the feedback voltage constant. This was done by manually adjusting the gain on the audio amplifier while watching the feedback voltage on the oscilloscope. The gain was increased until the gain limit of the amplifier was reached. At this point, the controller defaulted back to a constant-gain controller.

Two voltage limits were chosen, 100 and 200 volts rms. Rms limits were used because the voltmeter used to monitor the feedback voltage measured rms voltage, not peak voltage. All dimensional voltages reported in this section are rms voltages unless otherwise specified. These limits were dictated by safety and control circuitry limitations, not the breakdown voltage of the PVF_2. Note in Table 2-I that its breakdown voltage is well over 1000 volts. A test setup is currently being designed that will operate with control voltages up to 1000 volts.

4.2.3.2 Results and Discussion

The typical decay of an uncontrolled beam, a baseline test, is shown in Figure 4-7 in an oscilloscope photograph and a logarithmic plot. The upper trace in the oscilloscope photo is the rms feedback voltage, uniformly zero for this case. The lower trace is the tip displacement. Even though the decay envelope looks exponential in the oscilloscope photo, the logarithmic plot shows a slight change in slope. (The logarithmic plot should be a straight line for exponential decay. See Appendix D.) This indicates that the loss factor changes slightly with the amplitude of the vibrations. The passive loss factor at the large initial amplitudes (±2. cm tip displacement) was slightly more than $\eta_p = 0.003$, decreasing to 0.001 for small amplitudes (±0.5 mm tip displacement). This confirms the damping values obtained for small amplitude vibrations from the impact testing.

The results for the constant-gain controller and the two voltage limits are shown in Figures 4-8 and 4-9. Since this is a linear controller, one expects the decay envelope to be exponential. In the oscilloscope photos, the decay envelope does indeed look exponential, but, as in the uncontrolled case, the logarithmic plots show a change in the slope. This is partly due to the amplitude dependence of the passive damping seen in the uncontrolled case. Another cause for the change in slope may be that as the control voltage decays, its amplitude drops too low to be effective or falls below the noise floor.

For $V_{max} = 100$ V rms, the effective loss factor is slightly less than $\eta_{eff} = 0.006$, and slightly more than $\eta_{eff} = 0.007$ for $V_{max} = 200$ V rms. This is an improvement over the baseline damping in the beam, but, as noted in Section 3.3, the feedback voltage drops as the vibrations decay, indicating that for a given V_{max} much better damping could be achieved at the smaller vibration amplitudes.

The constant-amplitude controller took advantage of this by trying to keep the amplitude of the feedback voltage always at V_{max}. The results for the constant-amplitude controller, Figures 4-10 and 4-11, show a dramatic improvement over the constant-gain controller. With $V_{max} = 100$ V rms, the vibrations are totally damped in 18 seconds. For $V_{max} = 200$ V rms, the vibrations are damped in 15 seconds. Because the decay envelope of the vibration in the oscilloscope photo is not exponential, it is difficult to see how the effective loss factor is changing. However, the logarithmic plots clearly show how dramatically the effective damping increases for the lower amplitudes of vibration. For both voltage limits, the effective loss factor starts at the value achieved with the constant-gain controller and steadily increases to at least $\eta_{eff} = 0.040$ for the smaller amplitudes. This is at least a

factor of 40 increase in the damping at small vibration levels and was achieved using a very simple control law and moderate control voltages.

As mentioned previously, when the gain limit of the audio amplifier was reached, the controller defaulted to a constant-gain control law. This can be seen in the oscilloscope photos on the control voltage trace. The amplitude of the feedback voltage was constant until the vibrations were nearly zero. Then the decay envelope of the control voltage became exponential, a characteristic of a linear controller. Notice that this decay was much faster than that of the constant-gain controller tests, again indicating that the effective damping was much higher. This should be no surprise because the only difference between the constant-gain controller tests and the constant-gain portion of the constant-amplitude tests was that the gain was much higher in the latter case.

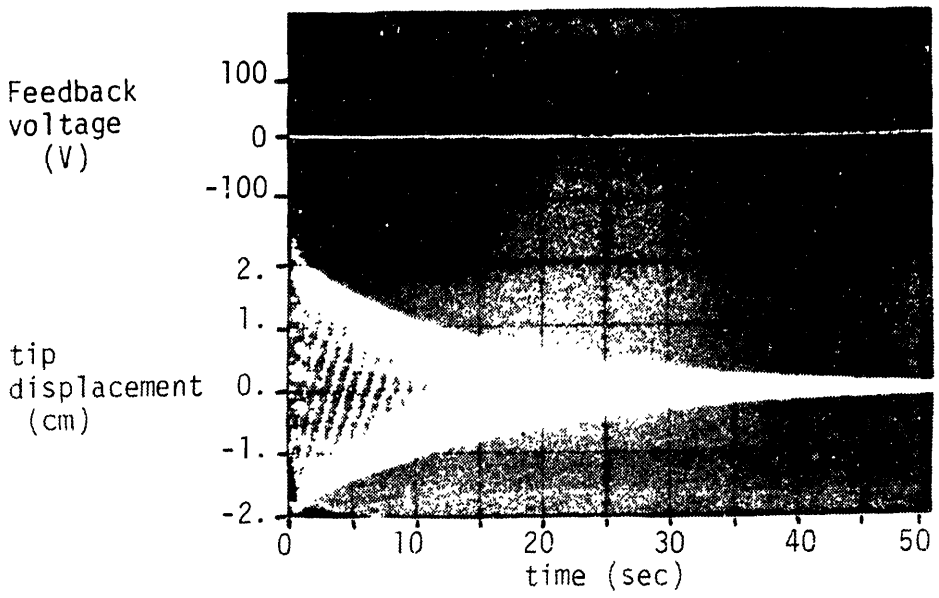

(a). Feedback voltage and tip displacement for the uncontrolled beam.

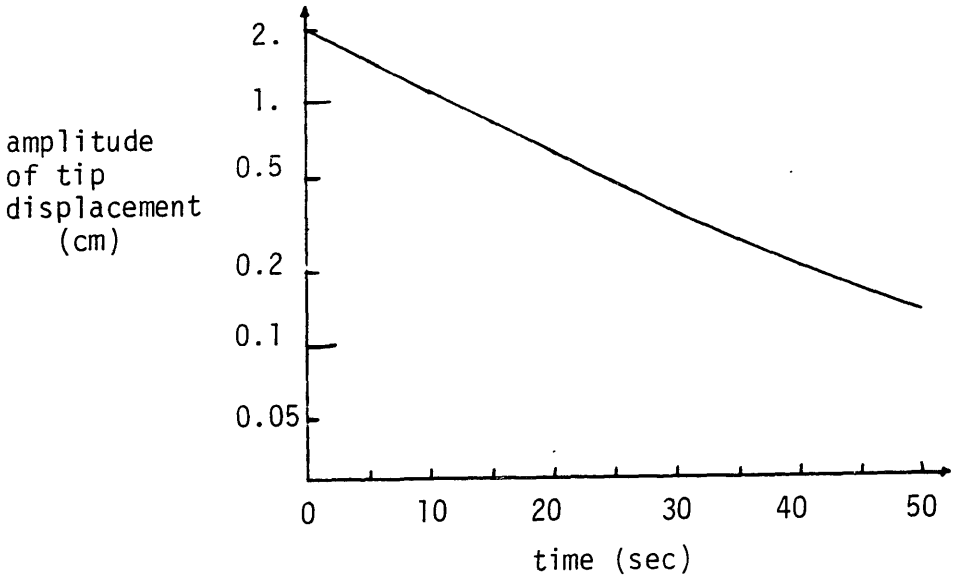

(b). Logarithmic plot of tip displacement decay envelope.

Figure 4-7: Free decay of first mode results for the uncontrolled beam.

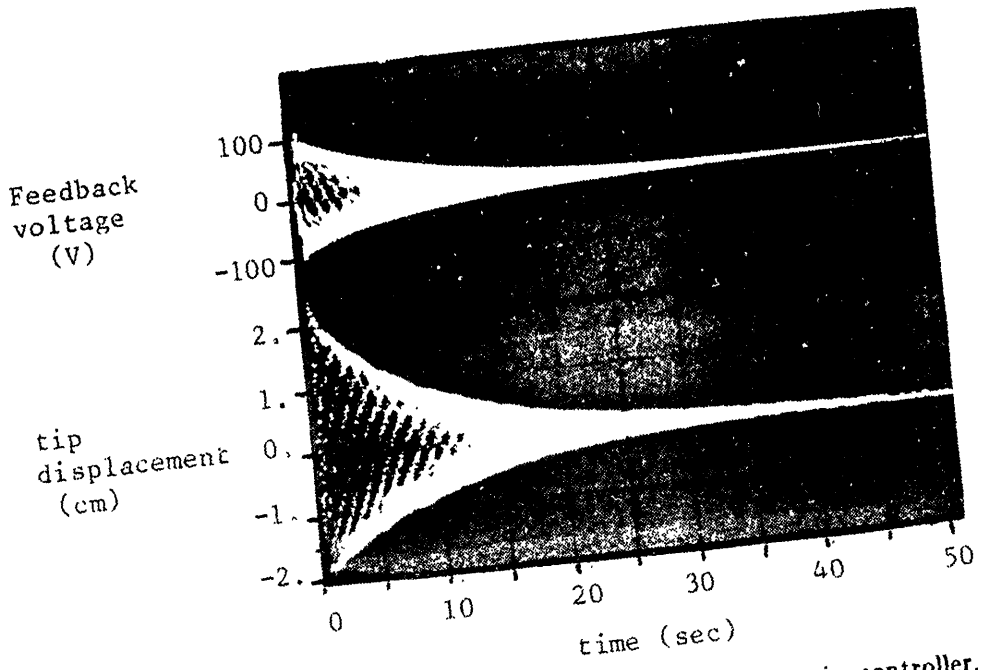

(a). Feedback voltage and tip displacement for the constant-gain controller.

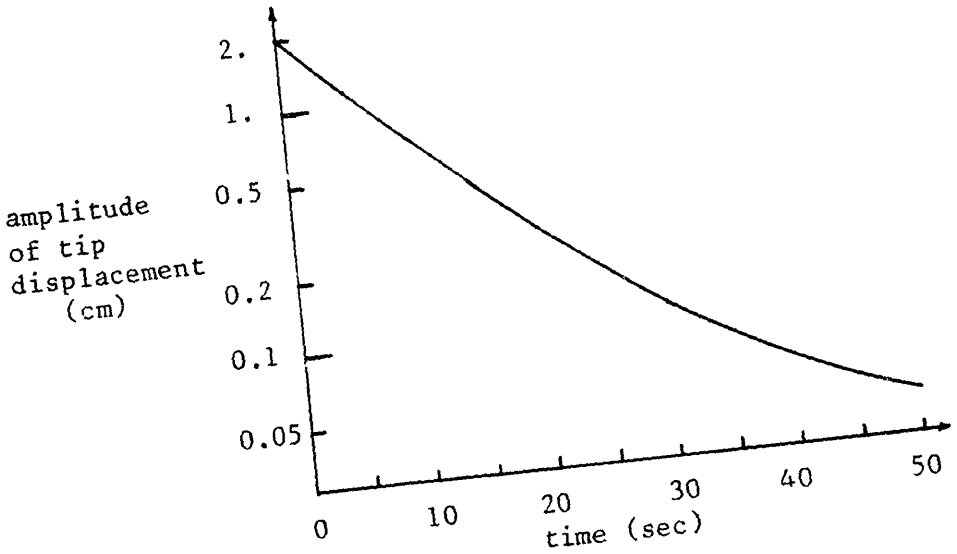

(b). Logarithmic plot of tip displacement decay envelope.

Figure 4-8: Free decay of first mode results for the constant-gain controller. $V_{max} = 100$ V rms.

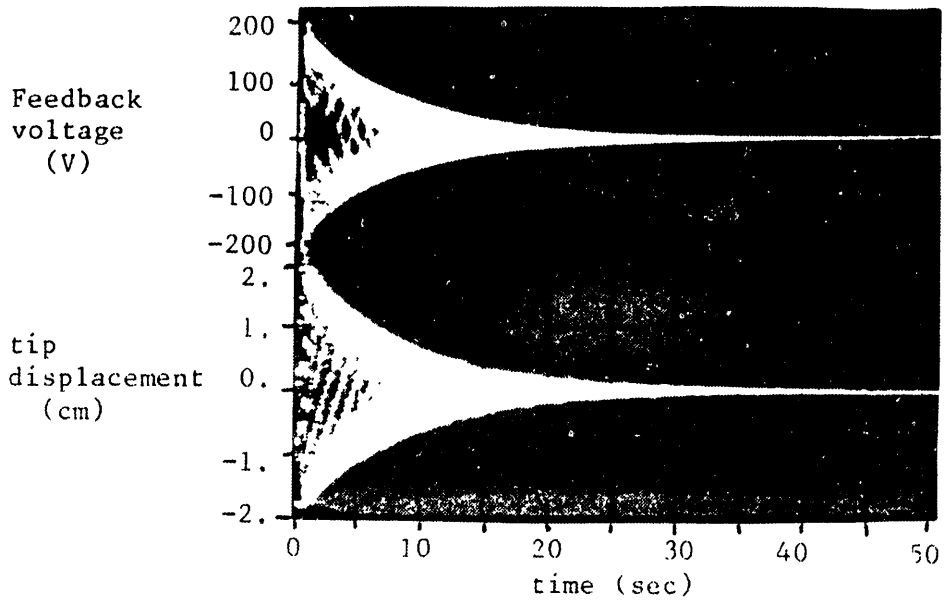

(a). Feedback voltage and tip displacement for the constant-gain controller.

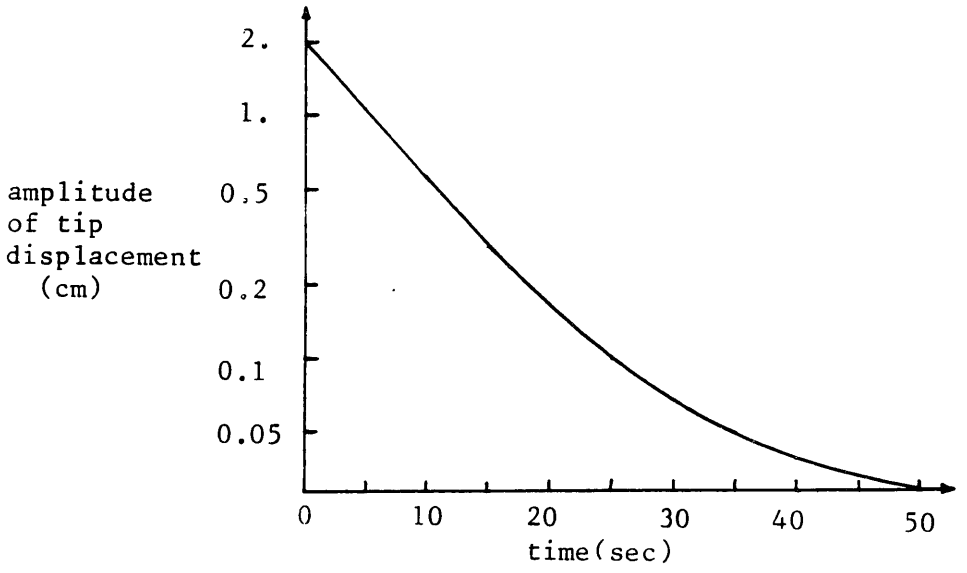

(b). Logarithmic plot of tip displacement decay envelope.

Figure 4-9: Free decay of first mode results for the constant-gain controller. V_{max} = 200 V rms.

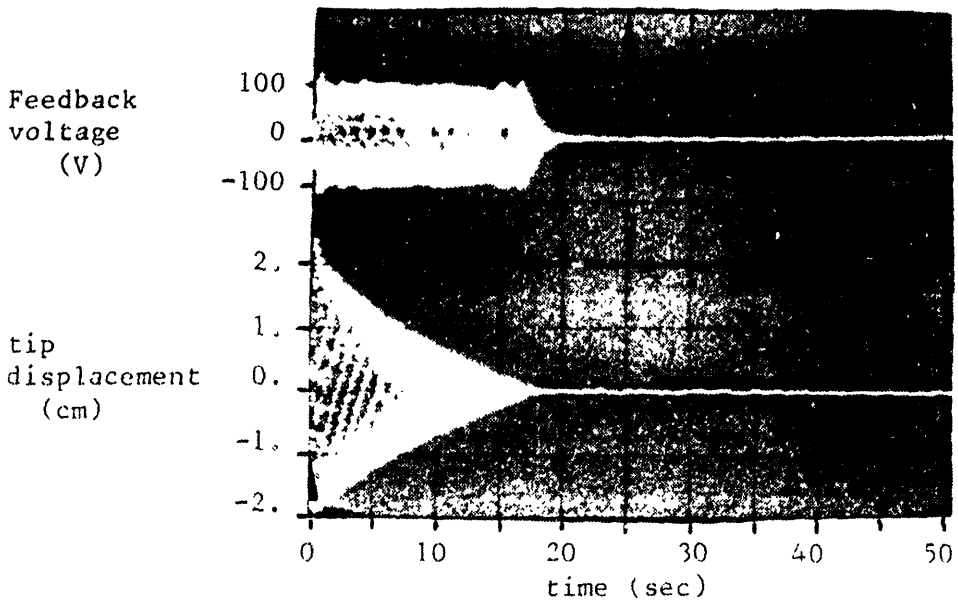

(a). Feedback voltage and tip displacement for the constant-amplitude controller.

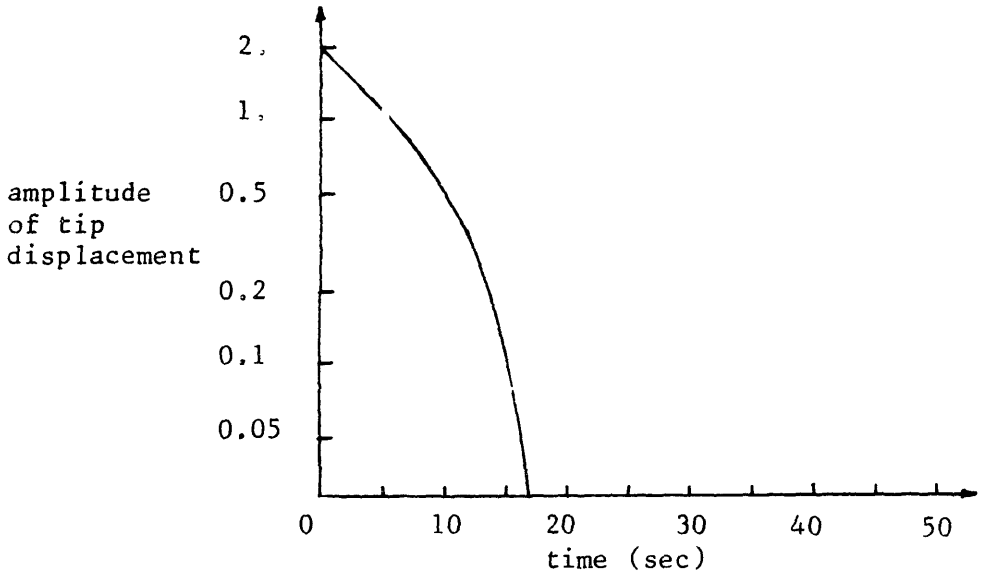

(b). Logarithmic plot of tip displacement decay envelope.

Figure 4-10: Free decay of first mode results for the constant-amplitude controller. $V_{max.} = 100$ V rms.

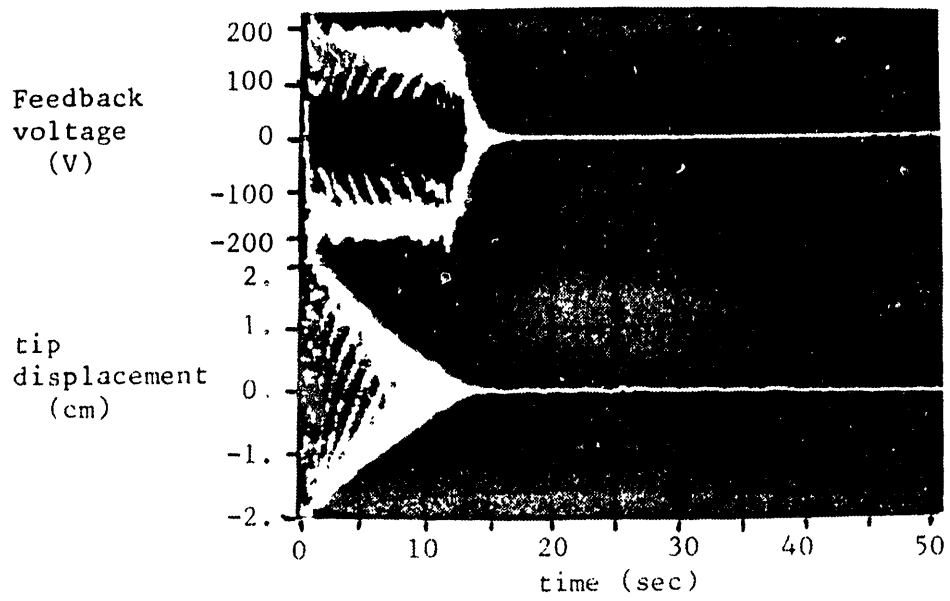

(a). Feedback voltage and tip displacement for the constant-amplitude controller.

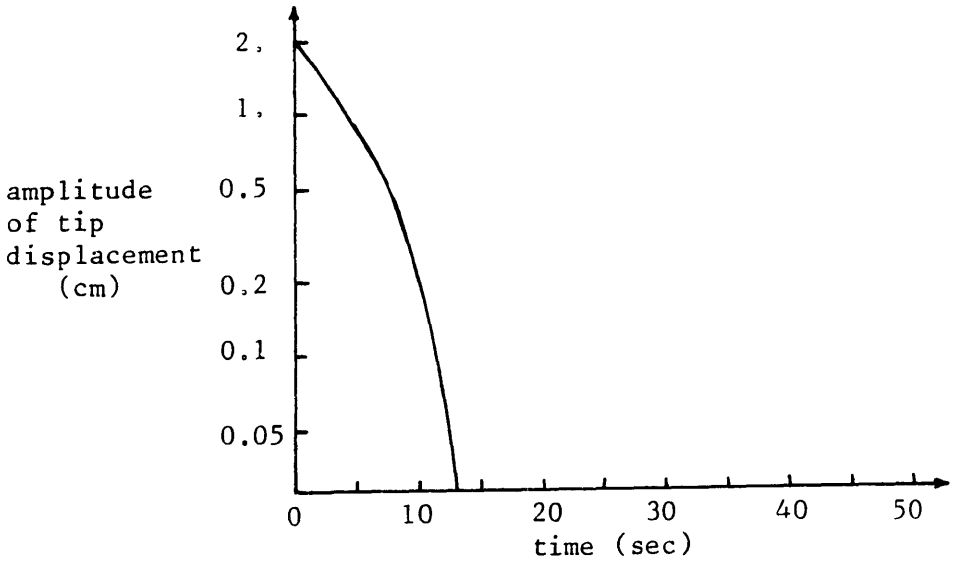

(b). Logarithmic plot of tip displacement decay envelope.

Figure 4-11: Free decay of first mode results for the constant-amplitude controller. V_{max} = 200 V rms.

The constant-amplitude controller results should also be compared with the simulation results from the parameter study (see Section 3.5). The passive loss factor in the composite beam was between $\eta_p = 0.003$ and 0.001 and the V_{max} was either 100 or 200 volts. The simulation cases that correspond to these voltages and $\eta_p = 0.002$ are shown in Figure 4-12 with the axes labeled in dimensional units that correspond to the dynamically scaled beam.Comparing the experimental results with the simulations one sees that the shape of the decay envelopes is very similar, both are nearly linear. This gives confidence in the simulations since the overall trends are same as those observed during the experimentation. However, the simulations predict that the control would be more effective than was actually observed. Part of the discrepancy may come from the fact that the simulations used the Lyapunov control law while the experimental results were achieved using the constant-amplitude control law. The Lyapunov control law produces a constant amplitude square wave which will do more work against the beam than the constant amplitude sine wave produced by the constant-amplitude controller, if the two waveforms have the same peak voltage limit. However, the constant-amplitude controller used an rms voltage limit, increasing the peak voltage, so the work done by the constant amplitude sine wave was increased as well. The trends are the same, though, because both the Lyapunov and the constant-amplitude controller produce constant amplitude feedback wave forms. The difference comes about because the wave forms are different.

Although the simulations are not entirely accurate, the experimental results do verify the simulation algorithm. They also dramatically support the trends that were predicted by the parameter study, particularly that the effective loss factor increases by more than an order of magnitude at small vibration levels for the same feedback voltage. These results, both experimental and analytical, indicate that an active damper with this type of control law may provide a way to keep resonant vibration from building up due to the extremely high levels of damping that can be achieved for low level vibrations. It may be possible to use this kind of damper in conjunction with another, more powerful actuator that will control the large amplitude vibrations. Powerful actuators often have problems such as limit-cycling and/or need a deadband at small vibration levels, providing a good complement to the active damper described here. Another configuration may be to use a nominal amount of passive damping to control the large amplitude vibrations which would be augmented by the active damper at low vibration levels.

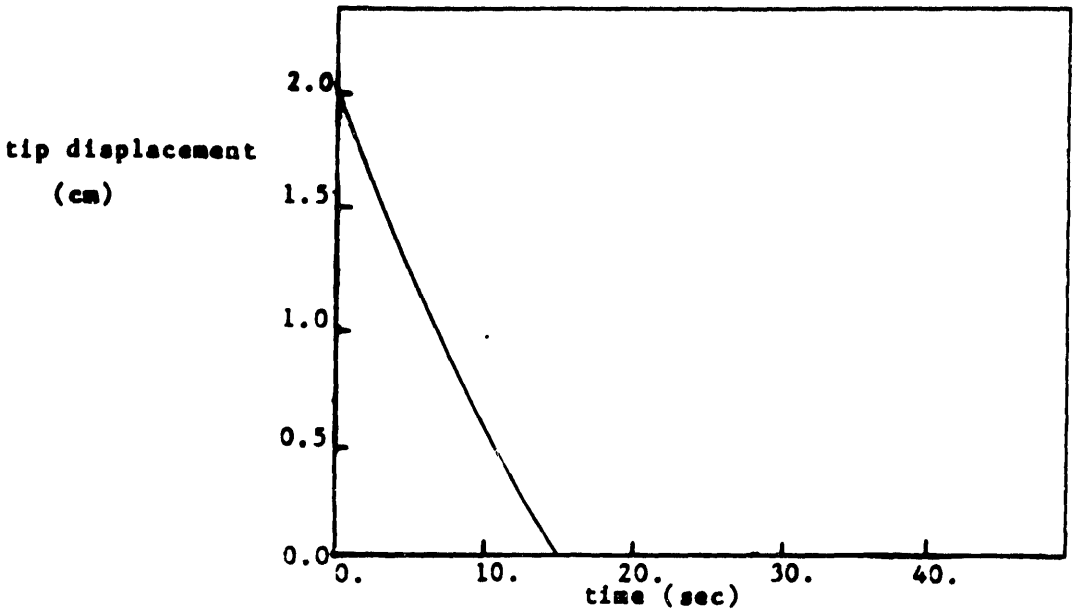

(a). Simulation results for $V_{max} = 100$ V.

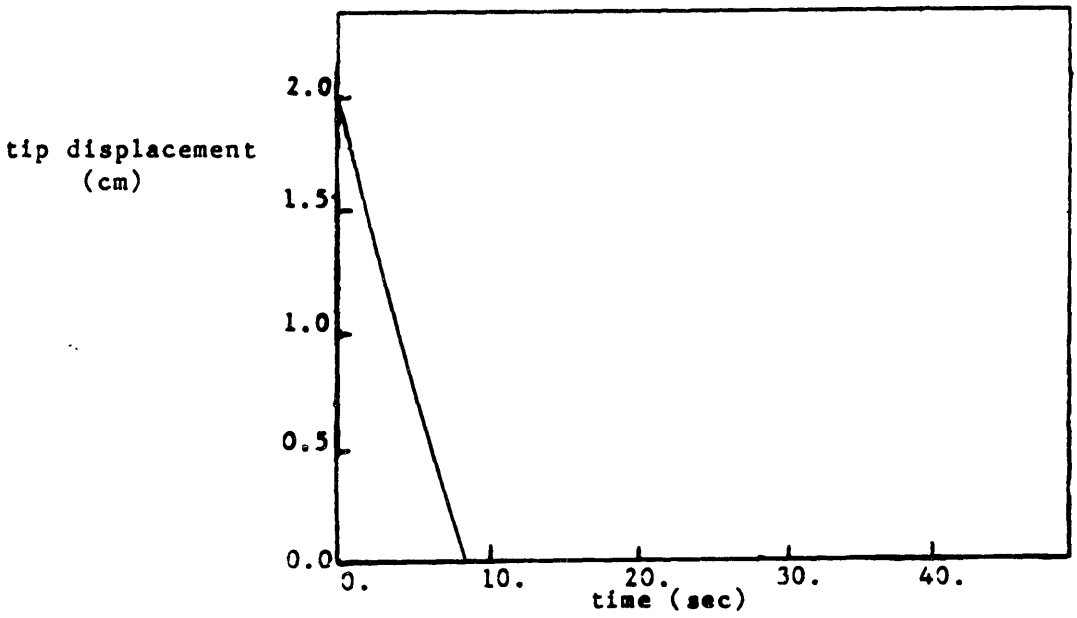

(b). Simulation results for $V_{max} = 200$ V.

Figure 4-12: Simulation results for the Lyapunov control law for two voltage limits. $\eta_p = 0.002$.

4.3 Continuous Excitation Testing

4.3.1 Apparatus and Procedures

In this set of tests, the effectiveness of the active damper was tested with a continuous excitation being applied to the base of the cantilever beam. By band limiting the excitation near the resonant frequency of interest, only that mode of vibration was excited. This allowed the control laws to be implemented using the linear velocity rather than angular velocity at the tip of the beam, and allowed the testing of the second and third modes as well as the first. A schematic of the apparatus used is shown in Figure 4-13.

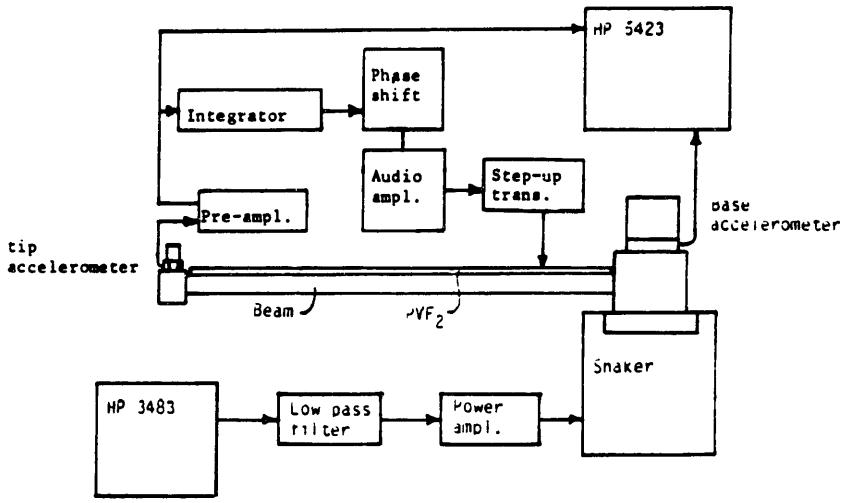

Figure 4-13: Schematic of apparatus used for continuous excitation testing.

The cantilever was clamped in a fixture which was mounted on a large shaker (Bruel & Kjaer model 4801 exciter body and model 4812 General Purpose head). A Hewlett-Packard model 3483 spectrum analyzer was used as an adjustable bandlimited random noise source. The noise signal from the analyzer had discrete steps so it was low pass filtered to smooth the steps before being input to the shaker amplifier.

The acceleration of the base of the beam, i.e., the clamping fixture, was measured using a 500 gm, internally preamplified accelerometer (Bruel & Kjaer model 8306). The tip acceleration was monitored using the same acceleromoeter and signal conditioning as used for the free decay tests. The measurement for this series of tests was a transfer function

between the base acceleration as input and the tip acceleration as output. This measurement was made with a second spectrum analyzer (HP model 5423A). Two analyzers were used so that the analysis bandwidth and the excitation bandwidth could be adjusted separately. This was useful during the preliminary testing because the power spectrum of the input could be held constant while the analysis bandwidth was adjusted to determine an appropriate setting. The damping was found using the half power bandwidth method, as was done for the impact testing. The base accelerometer was calibrated so the level of base acceleration could be determined, but the tip accelerometer was not because, as mentioned in Section 4.2.2, only the damping was of interest, not magnitude of the transfer function. The control circuitry was the same as for the free decay tests. Only the constant-gain controller was implemented because it was impossible to manually adjust the gain satisfactorily. (A Lyapunov controller is currently being designed which will be used in both the free decay and the continuous excitation tests.)

The shaker setup had a relatively large amount of noise associated with it. There were electrical and magnetic fields as well as some background vibration and thermal drift due to air currents in the test cell. Shielding took care of the fields and the air currents. The background vibrations had two main sources; the integral blower motor used to cool the shaker exciter and 120 Hz ripple in the field coil supply voltage. The blower motor was disconnected and a remote blower was rigged to cool the shaker. Filter capacitors were used to smooth the field coil supply. These efforts reduced the background vibrations to an acceptable level for the frequencies near the first and second modes. The noise level near the third mode, however, was too high and hence no results are available for the third mode.

To test the active damper for a given mode, first the phase of the feedback loop was adjusted to give the correct overall phase at the resonant frequency of interest. This was done in the same manner as for the free decay tests. The noise source was adjusted so that the noise bandwidth was centered on the resonant frequency. In this manner, only the mode of interest was excited.

During the testing, both the rms level of base acceleration and the feedback gain were varied. First, the rms base acceleration was adjusted to a given level using the gain on the shaker amplifier. Three levels of rms base acceleration were used for each mode. The highest level was chosen to be just below the level that would cause nonlinear vibrations or excessive motion, i.e., the beam hitting the shaker. The other two levels were lower and were chosen to give at least an order of magnitude range in the rms power of the base acceleration, i.e., the mean square base acceleration. While the base level of acceleration was

held constant, several transfer function measurements were made using different feedback gain levels. The feedback gain was adjusted using the gain on the audio amplifier. It was not adjusted to a specific gain level, rather it was adjusted so that a given peak voltage limit was not exceeded. Again, the measured voltage was an rms voltage. Instead of the peak 'instantaneous' rms voltage, a more appropriate measure to be used in the future may be a limit on the rms of the feedback voltage waveform over an extended period of time since the structure is undergoing random vibration.

4.3.2 Results and Discussion

Table 4-III summarizes the conditions and settings used for the continuous excitation testing. The results for the first mode are shown in Figures 4-14, 4-15, and 4-16. Figures 4-17, 4-18, and 4-19 give the results for the second mode. The transfer functions for the second mode appear to be stepped because the spectrum analyzer used as a noise source produced the noise at discrete frequencies. The analysis bandwidth happened to be small enough so that the individual frequency components of the excitation could be detected. No results are available for the third mode because there was too much background vibration from the shaker near the third mode's resonant frequency. Each transfer function plot shows a series of cases at the same rms base vibration level but with different feedback gains. The text below each transfer function plot summarizes the parameters for each of the cases.

Figure 4-14 shows the results for the highest rms level of base acceleration. The transfer function shows that the two controlled cases have only slightly less magnitude at resonance than the uncontrolled case. The effective loss factor values reflect the small increase in damping for each controlled case. Note that this small increase was achieved with the one of the largest feedback voltages used on the shaker setup.

Figure 4-15 shows the results for the first mode with the medium rms level of base vibration. Here the active control is more effective as shown by the reduced amplitude of the transfer function at resonance. The effective loss factor values were correspondingly improved, but not tremendously so.

Figure 4-16 shows the results for the first mode with the lowest rms base acceleration. Here the effective damping is much improved. The highest control voltage limit (100 V rms) yielded a decrease of nearly 15 db in the magnitude of the resonance. This was almost a factor of 8 increase in the damping over the uncontrolled case. As in the simulations and

the free decay tests, the active damper is most effective, for a given voltage limit, at low levels of vibration. For continuous excitation testing, though, the levels of vibration are rms displacement amplitude. Also note that the uncontrolled cases showed the loss factor depends on the rms vibration level, confirming the amplitude dependence noticed in the baseline free decay test.

The results for the high level of base acceleration for the second mode are shown in Figure 4-17. The added damping is easily observed in the transfer function plot but the largest increase in damping was slightly less than a factor of three. The results for the medium and low base acceleration levels for the second mode are shown in Figures 4-18 and 4-19, respectively. The effectiveness of the active damping was increased as the amplitude of vibrations was lowered. The magnitude reduction in the transfer functions were obvious, 10 db decrease for only 30 V rms maximum feedback voltage (lowest base acceleration case), but the increase in effective loss factor was relatively small, a factor of three maximum. One reason for this was that the tip acceleration for the second mode was smaller than that of the first mode so that the gain limit of the audio amplifier was reached sooner. This severely limited the range of feedback voltages that could be used. For the lowest level of base acceleration, the maximum feedback voltage was 30 V rms. If higher voltages could be reached, the effective loss factor would be correspondingly higher.

The results from the continuous excitation tests for the first mode cannot be compared with the results from the constant-amplitude controller for the free decay tests. This is because two different control laws were being used. For the continuous excitation tests, even though the feedback gain was changed between cases to adjust to a different voltage limit, it was constant within a given case. Hence the results from the continuous excitation tests can only be compared to the constant-gain controller results. In this light, the continuous excitation results show a marked improvement. The largest effective loss factor achieved for the constant-gain controller during the free decay tests was slightly over $\eta_{eff} = 0.007$ while the largest for the continuous excitation tests was $\eta_{eff} = 0.019$, both achieved with a voltage limit of 100 V rms. The reason for the increase was that during the continuous excitation case the voltage limit was reached at a higher gain. Since the constant-gain controller is linear, one would expect the effective loss factor to be dependent only on the feedback gain, not the amplitude of the vibration. To fully compare the constant-gain results and the continuous excitation tests, more free decay tests should be performed using smaller initial tip diplacements and the same voltage limits. This would have the effect of increasing the gain at which the voltage limit was reached, much the same as changing the level of base

acceleration for the continuous excitation tests. Such a comparison should show that the effective loss factor for a given feedback gain would be the same for both the free decay and the continuous excitation tests.

The active damper was effective on both the first and second modes of the cantilever beam. The same trends were noted for both modes, particularly that a given level of feedback voltage is much more effective at smaller vibration levels. However, the active damping seems to be more effective on the first mode. This is because the second mode has a larger modal energy per tip angle ratio than the first mode. This means that a larger feedback gain is needed for the second mode to achieve the same effective loss factor.

Table 4-III: Summary of conditions for continuous excitation testing.

	Mode # 1	Mode # 2
Excitation analyzer;		
Center frequency, (Hz)	0.00	64.0
Bandwidth, (Hz)	10.0	25.0
Resolution, (Hz)	0.145	0.145
Measurement analyzer;		
Center frequency, (Hz)	8.00	61.5
Bandwidth, (Hz)	8.00	8.00
Resolution, (Hz)	0.0313	0.0313
Mean square base acceleration, g^2_{rms}		
maximum	1.38×10^{-4}	7.35×10^{-4}
	1.86×10^{-5}	1.87×10^{-4}
minimum	2.46×10^{-6}	3.84×10^{-5}

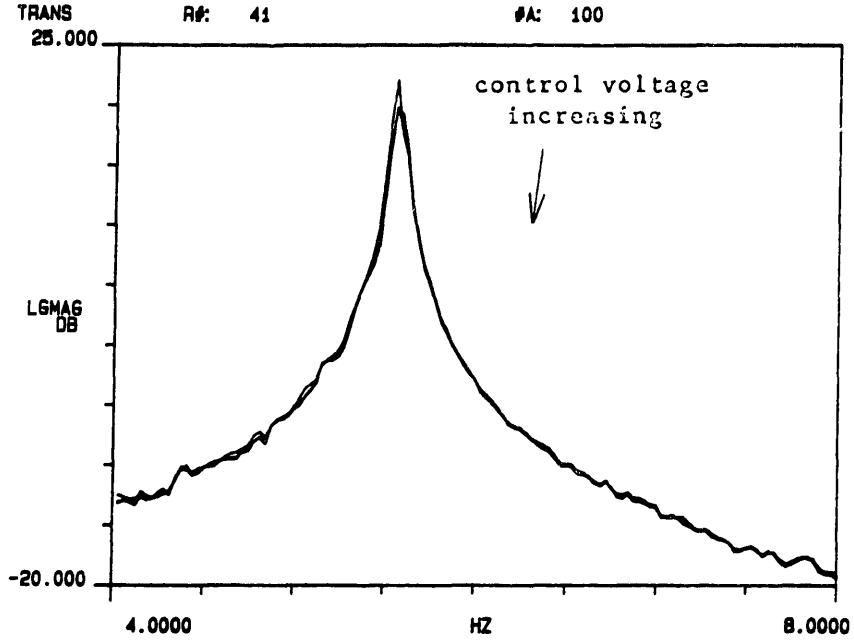

(a). Transfer functions for first mode. Highest base acceleration.

Mean square base acceleration: 1.38×10^{-4} g^2_{rms}

voltage limit	effective loss factor
0	0.0040
90	0.0051
130	0.0054

(b). Summary of results.

Figure 4-14: Continuous excitation testing, first mode, highest base acceleration.

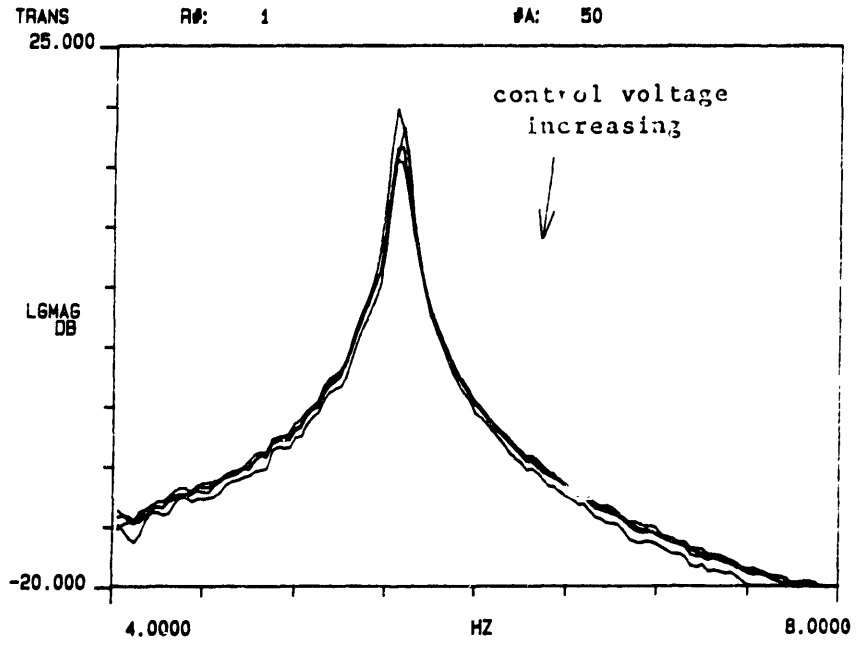

(a). Transfer functions for first mode. Medium base acceleration.

Mean square base acceleration: 1.36×10^{-5} g^2_{rms}

voltage limit	effective loss factor
0	0.0031
50	0.0051
100	0.0066
130	0.0075

(b). Summary of results.

Figure 4-15: Continuous excitation testing, first mode, medium base acceleration.

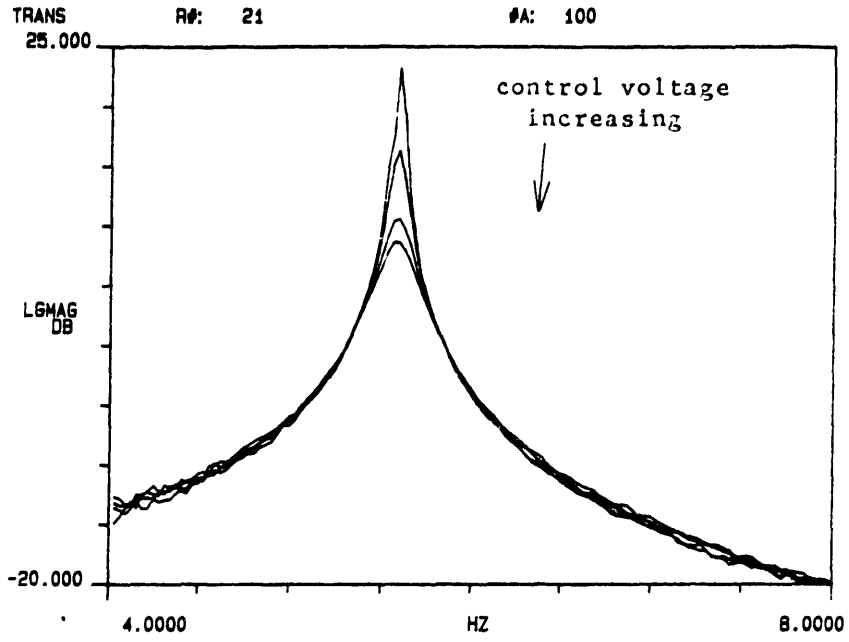

(a). Transfer functions for first mode. Lowest base acceleration.

Mean square base acceleration: 2.46×10^{-6} g^2_{rms}

voltage limit	effective loss factor
0	0.0026
50	0.0075
90	0.015
100	0.019

(b). Summary of results.

Figure 4-16: Continuous excitation testing, first mode, lowest base acceleration.

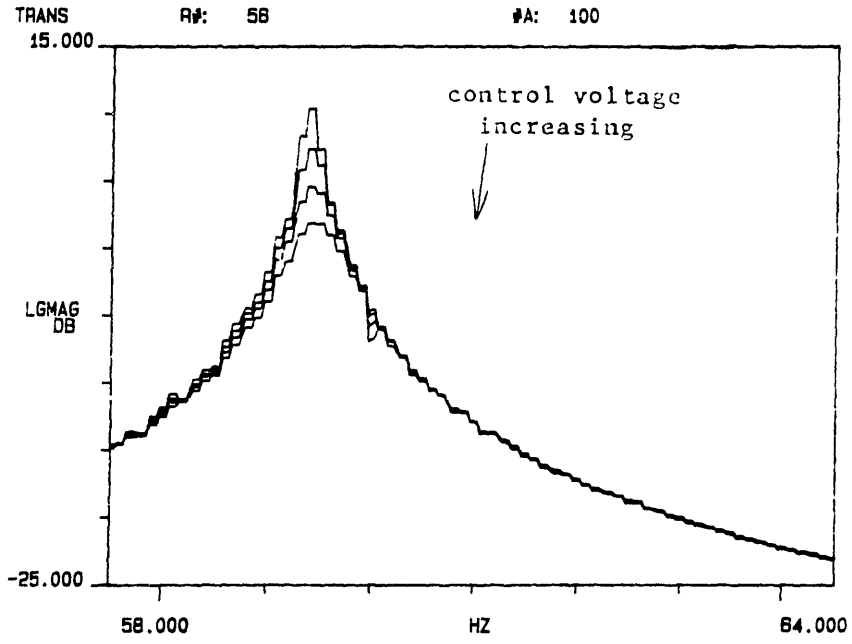

(a). Transfer functions for second mode. Highest base acceleration.

Mean square base acceleration: 7.35×10^{-4} g^2_{rms}

voltage limit	effective loss factor
0	0.0016
25	0.0023
65	0.0032
100	0.0043

(b). Summary of results.

Figure 4-17: Continuous excitation testing, second mode, highest base acceleration.

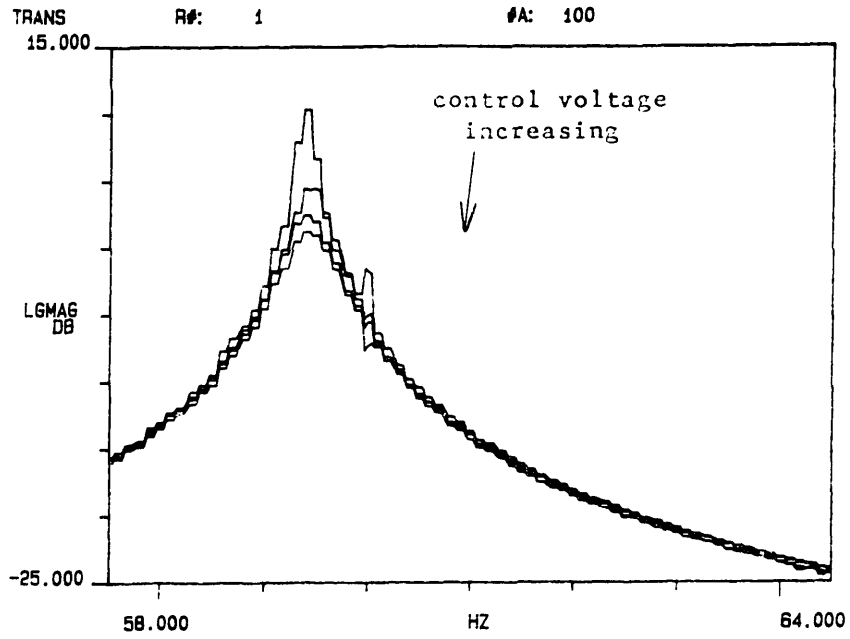

(a). Transfer functions for second mode. Medium base acceleration.

Mean square base acceleration: 1.37×10^{-4} g^2_{rms}

voltage limit	effective loss factor
0	0.0014
30	0.0029
50	0.0037
60	0.0041

(b). Summary of results.

Figure 4-18: Continuous excitation testing, second mode, medium base acceleration.

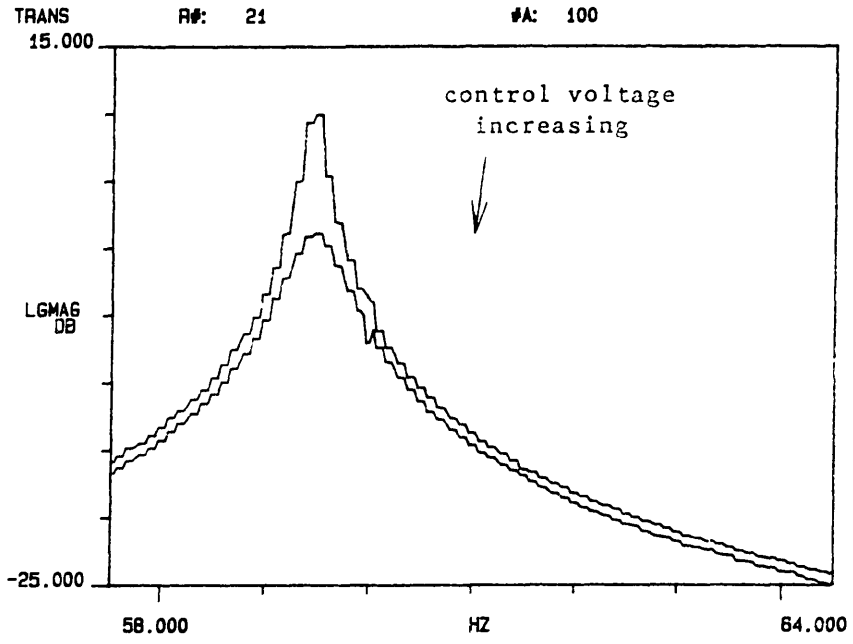

(a). Transfer functions for second mode. Lowest base acceleration.

Mean square base acceleration: 3.34×10^{-5} g^2_{rms}

voltage limit	effective loss factor
0	0.0014
30	0.0039

(b). Summary of results.

Figure 4-19: Continuous excitation testing, second mode, lowest base acceleration.

Chapter 5
Conclusions and Recommendations

5.1 Conclusions

The control of distributed-parameter systems with discrete actuators and sensors and using lumped-parameter control theory may lead to perfomance tradeoffs [1, 4]. Using distributed-parameter control theory and distributed-parameter actuators one can avoid some of the tradeoffs, such as truncation of the model. An active distributed-parameter damper for a cantilever beam was designed and evaluated. The distributed-parameter active element was a piezoelectric polymer, poly(vinylidene fluoride). A control law was developed using Lyapunov's second method for distributed-parameter systems. For the damper configuration used, this control law depends only on the angular velocity at the tip of the cantilever beam. Since no modes were truncated in the analysis, this control law will theoretically control all the modes of vibration. This avoids any structural problems with uncontrolled modes. Also, an attempt was made to use a distributed-parameter 'optimal' formulation by Tzafestas [12, 13] that parallels the variational calculus approach used in lumped-parameter modern control theory. During this attempt, several questions were raised concerning the validity of certain mathematical operations used to obtain a Riccati equation. No attempt was made to solve this Riccati equation.

The angular velocity of the tip of the cantilever beam was not available. The linear velocity at the tip was available and was found by integrating the linear acceleration at the tip. The linear velocity and the angular velocity at the tip of the beam are directly related if only one mode of vibration is present, so the remaining analysis and the preliminary testing was performed on a single mode at a time so this relation could be used. This sensor limitation and the resulting use of one mode at a time was not related to the distributed-parameter nature of the system, however.

A simulation algorithm to predict the effect of the active damper on the free decay of a single mode of the cantilever beam using the non-dimensionalized equations of motion was developed. A parameter study was performed using the first mode of the cantilever beam and the Lyapunov control law. The control voltage limits and the amount of passive

damping in the system were varied. The parameter study results are presented in three forms; tip displacement amplitude or decay envelope vs. time, slope of decay envelope vs. tip displacement amplitude, and effective loss factor vs. tip displacement. These simulation results are presented in dimensionless format and show the differences in the effect of the passive and active damping.

The passive damping is linear and gives the typical exponential decay envelope, indicating a constant effective loss factor. The passive damping is most effective for larger vibration amplitudes because a large amount of energy is in the system. Since the passive damping dissapates a fixed percentage of the energy in the system each cycle, a relatively large amount of energy is dissapated each cycle. For smaller vibration levels, the amount of energy in the system decreases as the square of the vibration amplitude so the energy dissapated approaches zero as the vibration level decreases even for large values of passive damping.

The active damping is nonlinear and gives a linear decay envelope, indicating a changing effective loss factor which increases for smaller vibration levels. The active damping is most effective for smaller vibration levels because an actuator with a nonlinear control law such as the Lyapunov control law dissapates an increasing percentage of the system energy as the vibration amplitude decreases. Even though the amount of energy dissapated per cycle is decreasing, the amount of energy in the system is decreasing faster as the vibration amplitude decreases. For all of the control voltage limits used in the parameter study, the effective loss factor for the active damping increased to at least $\eta_{eff} = 0.5$ for small vibration levels regardless of the passive damping value, although the vibration level at which a given effective loss factor was achieved was highly dependent on the control voltage limit.

Two other control laws were developed to compare experimentally with the Lyapunov control law; constant-gain and constant-amplitude. The constant-gain control law was negative velocity feedback with a constant gain, a linear control law that would be easy to implement. The constant-amplitude control law was negative velocity feedback with a time varying gain such that the amplitude of the the feedback was constant. This was a nonlinear control law that was very similar to the Lyapunov control law. The constant-amplitude control law would produce a constant amplitude sine wave for the feedback voltage while the Lyapunov control law would produce a constant amplitude square wave.

Preliminary testing of the active damper was done on the first mode of vibration of a small cantilver beam for the free decay testing and on the first and second modes for the

continuous excitation testing. The baseline damping for the first mode was η=0.003 for large vibrations ($\pm$2 cm tip displacement) decreasing to η=0.001 for small vibrations ($\pm$0.5 mm tip displacement). Free decay testing was performed using the constant-gain and constant-amplitude controllers and with two control voltage limits, 100 and 200 V rms. The constant-gain controller provided approximately double the baseline damping for V_{max}=100 V rms, slightly more for the 200 V rms case. The constant-amplitude controller was nonlinear and provided nonlinear damping; double the baseline damping for large vibrations increasing by a factor of 40 to at least η=0.040 for small vibrations. This behavior is the same as predicted by the parameter study for the Lyapunov control law, which is expected because the control laws are very similar, e.g., they both produce constant amplitude feedback waveforms.

For the continuous excitation testing, the clamping fixture for the beam was mounted on a shaker. The beam was excited by bandlimited random noise that was centered on the resonant frequency of interest so that only one mode of vibration would be present. Only the constant-gain controller was implemented during the continuous excitation testing. The rms level of base acceleration and the feedback gain were varied between runs. These tests showed the same trends as the free decay tests and the parameter study. For the highest mean level of base acceleration, and hence the highest rms energy in the system, the effective loss factor was lower for a given peak feedback voltage limit than for a run with a lower level of base acceleration.

For the first mode, with the highest rms level of base acceleration and a control voltage limit of V_{max}=130 V rms, the loss factor was increased from a baseline damping of η_p=0.0040 to η_{eff}=0.0054. With the lowest rms level of base acceleration and a control voltage limit of V_{max}=100 V rms, the damping was increased from η_p=0.0026 to η_{eff}=0.020, nearly an order of magnitude increase. This increase damping produces a corresponding decrease in the magnitude of the resonance. For the low level acceleration case cited here the magnitude dropped 15 db.

Similar results were achieved for the second mode. With the highest rms base acceleration and V_{max}=25 V rms, the damping was increased from η_p=0.0016 to η_{eff}=0.0023. For the lowest rms base acceleration and V_{max}=30 V rms, the damping increased from η_p=0.0014 to η_{eff}=0.0039 . This corresponds to a 10 db reduction in the magnitude of the resonance. The range for V_{max} was restricted because the gain limit of the audio amplifier was reached, especially in the lowest rms base acceleration case.

5.2 Recommendations

The work presented here has only begun to examine the use of distributed-parameter control theory and distributed-parameter actuators on a very basic level. The use of PVF_2 as distributed-parameter actuator opens many new possibilities. Several possible topics for further work are discussed below.

One project would be attempting to control all modes at once using the Lyapunov control law and an angular velocity or angular acceleration sensor at the tip of the cantilever beam. Controlling all modes, or at least several, at once, even for such a simple system, would be a great step towards a practical realization of distributed-parameter control theory for elastic systems.

Another project would be the use of viscoelastic materials to provide nominal passive damping which can be actively adjusted higher or lower. There may be instances where a very lightly or a very heavily damped resonance is desired, but only at certain times. The passive damping would control the vibrations for most of the time, allowing the active control to be off until either more or less damping is required.

The use of distributed-parameter optimal control theory to design control algorithms will allow one to apply spatial weightings between the same elements of vectors as well as weightings between different elements of a vector. One possible application of this may be to weight the vibration at the tip of the cantilever beam more heavily than the vibrations along its length, attempting to keep the tip still at the expense of vibrations along the length of the beam. Another applicaton may be shape control of large space structures, weighting regions more heavily where the shape is more critical. Distributed-parameter optimal control could also determine the optimum spatial distribution of the control if the spatial distribution could be varied in real time.

Spatially varying control could be either a fixed or time-varying spatial distribution. A fixed distribution may allow the control to be tailored to a particular mode of interest. One use for this may be to control only one of several closely spaced modes. Since the control is tailored to a particular mode shape, the neighboring modes will be excited less. A time-varying spatial distribution could be used in conjunction will distributed-parameter optimal control to provide the optimal control in space as well as time.

PVF_2 could also be used as a distributed-parameter sensor. The voltage across its surfaces produced by a strain is proportional to the integral of the charge produced by each

section of PVF_2. Hence the voltage is proportional to the integral of the strain. The possibility of spatially varying the sensing is also introduced. As with spatially varying control, spatially varying sensing could be used to sense a particular mode from several closely spaced modes.

Appendix A
Equations of Motion For the Active Damper

This appendix will present the derivation of the equations of motion for the active damper. First, the piezoelectric strain and its effects on the system are examined. A variational formulation is used to find the equations of motion for the active damper. Finally, the equations of motion are non-dimensionalized so that the results of the analysis can easily be applied to either the scaled model or to the actual Draper structure.

A.1 Effect of the Piezoelectric Strain

The active damper consists of a cantilever beam with a tip mass and tip inertia and a layer of PVF_2 bonded to one side of the beam. A sketch of the resulting two layer beam is shown in Figure A-1.

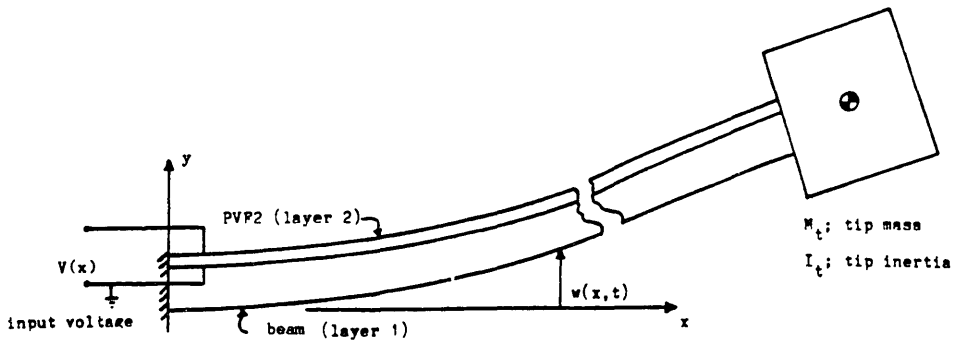

Figure A-1: Active damper configuration.

The beam has a flexible length, l. A subscript $(\cdot)_1$ refers to the original beam while a $(\cdot)_1$ refers to the PVF_2 layer. The control is the voltage applied to the PVF_2. The voltage causes a stress in the PVF_2 due to the piezoelectric effect.

If the PVF_2 layer was free to move (i.e., not bonded to the beam) the piezoelectric strain in the x-direction, ϵ_p, would be given by

$$\epsilon_p(x,t) = V(x,t) \cdot \frac{d_{31}}{h_2} \tag{A.1}$$

where d_{31} is the appropriate static piezoelectric constant, h_2 is the thickness of the PVF_2 layer, and V(x,t) is the control voltage. The composite beam is assumed to be uniform along its length. Since the PVF_2 is bonded to the beam, however, it is not free to move and the effect of the control voltage is to induce a *negative* prestrain in the PVF_2 layer. The prestrain is termed negative because it is in the opposite direction as the strain of the unbonded PVF_2. If the unbonded PVF_2 strains ϵ_p, a prestrain of $-\epsilon_p$ is needed to bring the PVF_2 back into position to be bonded to the original beam. This is shown in Figure A-2.

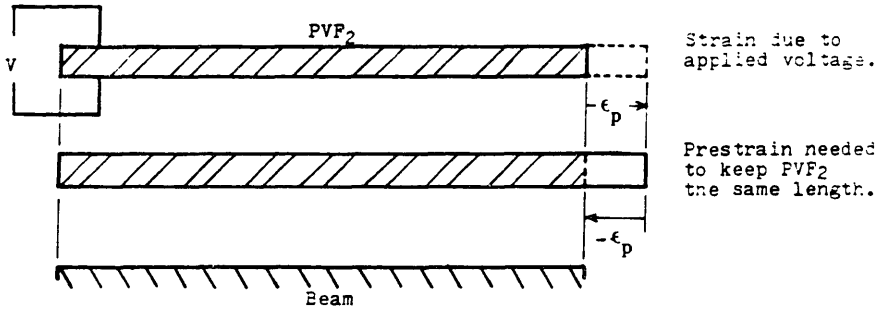

Figure A-2: The control voltage introduces a *negative* prestrain.

This prestrain has two effects on the two layer beam:

1. Longitudinal strain, ϵ_l to keep a force equillibrium in the axial (x-direction), and
2. Bending due to the torque from the prestrain acting through the moment arm from the midplane of the PVF_2 layer to the neutral axis of the two layer beam.

This is very similar to the behavior of a bimetallic spring as the temperature changes.

The total force on a crosssection of the beam in the x-direction is

$$F_x = \int_A \sigma_x \, dA$$
$$= \int_A E\epsilon_x \, dA \qquad (A.2)$$

where σ_x and ϵ_x are the stress and strain in the x-direction, respectively, A is the cross-sectional area of the composite beam, and E is the Young's modulus. The total strain in the x-direction for the PVF_2 layer is the sum of the prestrain, the longitudinal strain, and the bending strain, or

$$\epsilon_2 = -\epsilon_p + \epsilon_l + \epsilon_b \quad . \qquad (A.3)$$

For the original beam, the total strain in the x-direction is

$$\epsilon_1 = \epsilon_l + \epsilon_b \quad . \qquad (A.4)$$

The longitudinal strain is assumed to be constant across the cross-section of the composite beam and the prestrain is assumed to constant across the cross-section of the PVF_2 layer. Combining these relations with Eqn. (A.2) gives

$$F_x = \int_0^b \int_0^{h_1} E_1(\epsilon_b + \epsilon_l) \, dy \; + \int_{h_1}^{h_1+h_2} E_2(\epsilon_b + \epsilon_l - \epsilon_p) \, dy \, dz \qquad (A.5)$$

where b is the depth of the beam (both layers are assumed to have the same depth) and h_1 and h_2 are the thickness of the original beam and the PVF_2 layers, respectively. For a beam in bending, the strain is given by

$$\epsilon_b(y) = \frac{-(y - D)}{R} \qquad (A.6)$$

where D is the location of the neutral axis and R is the radius of curvature. Tension is considered positive. The neutral axis is the surface in a beam that does not experience any strain due to bending. A two layer beam with positive radius of curvature is shown in Figure A-3.

Assuming that the motion due to the longitudinal strain is negligible so that any

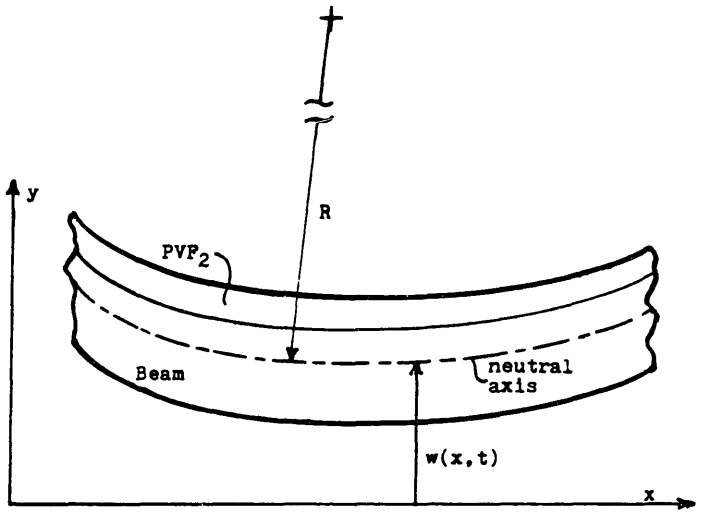

Figure A-3: Two layer beam in bending.

longitudinal inertial forces are negligible, F_x must be equal to zero because there is no longitudinal force applied to the beam. Substituting Eqn. (A.6) into Eqn. (A.5) and performing the integration yields

$$F_x = b \left[\frac{-1}{R} \left(E_1 h_1 \left(\frac{h_1}{2} - D \right) + E_2 h_2 \left(\frac{h_2}{2} + h_1 + D \right) \right) + \left(E_1 h_1 \epsilon_l + E_2 h_2 (\epsilon_l - \epsilon_p) \right) \right] = 0 \quad . \tag{A.7}$$

The terms in square brackets are grouped into those due to bending and those due to longitudinal strain. Using the principle of superposition, one can say that the combination of longitudinal strain and bending strain is equivalent to the sum of the individual strains. Therefore, one can use Eqn. (A.7) to show that the bending terms and the longitudinal terms are each equal to zero, or

$$E_1 h_1 \epsilon_l + E_2 h_2 (\epsilon_l - \epsilon_p) = 0 \tag{A.8}$$

and

$$E_1 h_1 \left(\frac{h_1}{2} - D \right) + E_2 h_2 \left(\frac{h_2}{2} + h_1 + D \right) = 0 \quad . \tag{A.9}$$

The location of the neutral axis, D, can be found by solving Eqn. (A.8) for D, which yields

$$D = \frac{E_1 h_1^2 + E_2 h_2^2 + 2h_1 h_2 E_2}{2(E_1 h_1 + E_2 h_2)} \quad . \tag{A.10}$$

From Eqns. (A.1) and (A.9) one can solve for the value of ϵ_l in terms of the control voltage, V, which is

$$\epsilon_l(x,t) = \frac{E_2 h_2}{E_1 h_1 + E_2 h_2} \cdot \epsilon_p(x,t) \quad . \tag{A.11}$$

The moment or torque, T, is developed because the prestrain, ϵ_p, and the longitudinal strain, ϵ_l, result in a force in the beam which acts through the moment arm to the neutral axis. The torque is found by taking the integral over the cross-section of the beam of the longitudinal force multiplied by the moment arm to the neutral axis, or

$$\begin{aligned} T(x,t) &= \int_0^b \int_0^{h_1} E_1 \epsilon_l \, (y - D) \, dy \quad + \int_{h_1}^{h_1+h_2} E_2(\epsilon_l - \epsilon_p)(y - D) \, dy \quad dz \\ &= E_1 \epsilon_l h_1 b\left(\frac{h_1}{2} - D \right) + E_2(\epsilon_l - \epsilon_p) h_2 b\left(\frac{h_2}{2} + h_1 - D \right) \quad . \end{aligned} \tag{A.12}$$

The first group of terms represents the torque from layer 1, the original beam, while the second represents the torque from the PVF_2 layer. The terms inside brackets represent the moment arm from the midplane of the particular layer to the neutral axis of the beam. The terms outside the brackets are the net force in that layer. Substituting Eqn. (A.10) into Eqn. (A.12) and reducing yields

$$T(x,t) = - \frac{E_1 h_1 E_2 h_2 b}{(E_1 h_1 + E_2 h_2)} \left(\frac{h_1 + h_2}{2} \right) \epsilon_p \quad . \tag{A.13}$$

Note that all terms involving ϵ_l have canceled. This means the torque is only a function of the prestrain and the materials and geometry of the composite beam, and does not depend on the longitudinal strain. Substituting for ϵ_p from Eqn. (A.1), the torque can be found as a function of control voltage, given by

$$\begin{aligned} T(x,t) &= - \frac{E_1 h_1 E_2 b}{(E_1 h_1 + E_2 h_2)} \left(\frac{h_1 + h_2}{2} \right) d_{31} \, V(x,t) \\ &= c \cdot V(x,t) \quad . \end{aligned} \tag{A.14}$$

where c is a constant (for given beam materials and geometry) that expresses the torque produced per unit control voltage.

A.2 Variational formulation of equations of motion

The formulation presented here will use a Bernoulli-Euler beam model and Hamilton's Principle to find the equations of motion [30]. Hamilton's Principle states:

> An admissible motion of a system between specified states at times t_i and t_f is a natural motion if and only the variational indicator vanishes for arbitrary admissible variations.

The variational indicator, VI, is given by

$$VI = \int_{t_i}^{t_f} \left[\delta(T^* - V) + \sum_{j=1} \Xi_j \, \delta\xi_j \right] dt \tag{A.15}$$

where δ is the variational operator, ξ_j is the jth generalized coordinate, Ξ_j is the jth generalized force, T^* is the kinetic co-energy, and V is the potential energy of the system [30]. The only generalized coordinate for this case is the transverse displacement, w(x,t), since the longitudinal motion of the beam is assumed to be negligible.

For transverse motions of the composite beam, the kinetic co-energy of the system is given by

$$T^* = \int_0^l \frac{1}{2} (\rho_1 A_1 + \rho_2 A_2) \left(\frac{\partial w}{\partial t}\right)^2 dx + \frac{1}{2} \left(M_t \left(\frac{\partial w}{\partial t}\right)^2 + I_t \left(\frac{\partial w}{\partial t}\right)^2 \right) \Bigg|_{x=l} \tag{A.16}$$

where ρ is the density and A is the cross-sectional area of the particular layer. The groups of terms represent the kinetic co-energy of the beam, the tip mass, and the tip inertia, respectively.

To find the potential energy of the system, first note that the strain energy per unit volume (specific strain energy), V, for an element undergoing uniaxial strain is

$$V = \frac{1}{2} E\epsilon^2 \quad . \tag{A.17}$$

The total potential energy (all strain energy for this case) can be found by integrating the specific strain energy over the entire composite beam. Therefore, the total potential energy, V, is given by

$$V = \int_0^l \int_0^b \int_0^{h_1} \frac{1}{2} E_1 \epsilon_1^2 \, dy + \int_{h_1}^{h_1+h_2} \frac{1}{2} E_2 \epsilon_2^2 \, dy \, dz \, dx \quad . \tag{A.18}$$

Substituting for the strains from Eqns. (A.4), (A.3), and (A.6), using the approximation that

$$\frac{1}{R} \approx \frac{\partial^2 w}{\partial x^2} \tag{A.19}$$

for large R, and performing the integration over y and z yields

$$V = \int_0^l \left[\frac{1}{2} [E_1 I_1 + E_2 I_2] \left(\frac{\partial^2 w}{\partial x^2} \right)^2 + \frac{1}{2} [E_1 h_1 b \epsilon_l^2 + E_2 h_2 b (\epsilon_l - \epsilon_p)^2] \right.$$
$$\left. - b [E_1 \epsilon_l h_1 \left(\frac{h_1}{2} - D \right) + E_2 (\epsilon_l - \epsilon_p) h_2 \left(\frac{h_2}{2} + h_1 - D \right)] \frac{\partial^2 w}{\partial x^2} \right] dx \tag{A.20}$$

where I is the area moment of inertia of a layer about the neutral axis. The first term represents the strain energy due to bending, the second is the strain energy due to the longitudinal strain, and the third represents the work done by the torque, T(x). Since the torque is included in the potential energy relation, there are no generalized forces for this case.

Substituting Eqns. (A.16), (A.20), and (A.12) into the variational indicator, Eqn. (A.15), and taking the variations with respect to the transverse displacement, w, yields

$$VI = \int_{t_i}^{t_f} \left[\int_0^l \rho A \frac{\partial w}{\partial t} \delta \left(\frac{\partial w}{\partial t} \right) dx + \left[M_t \frac{\partial w}{\partial t} \delta \left(\frac{\partial w}{\partial t} \right) + I_t \frac{\partial^2 w}{\partial t \partial x} \delta \left(\frac{\partial^2 w}{\partial t \partial x} \right) \right] \Bigg|_{x=l} \right.$$
$$\left. - \int_0^l \left(EI \frac{\partial^2 w}{\partial x^2} \delta \left(\frac{\partial^2 w}{\partial x^2} \right) - T \delta \left(\frac{\partial^2 w}{\partial x^2} \right) \right) dx \right] dt \tag{A.21}$$

where $EI = E_1 I_1 + E_2 I_2$, or the total bending stiffness of the composite beam and $\rho A = \rho_1 A_1 + \rho_2 A_2$, or its total mass per unit length. The geometric boundary conditions for the composite cantilever beam are prescribed by

$$w = \frac{\partial w}{\partial x} = 0 \qquad \text{for } x=0 \tag{A.22}$$

so that the variations at x=0 must be zero for an admissible variation. Also, since the motion is taking place between known states, the variations at times $t=t_i, t_f$ must be zero as well. Using integration by parts with respect to both space and time, as necessary, along with the boundary conditions mentioned above, and regrouping yields

$$VI = \int_{t_i}^{t_f} \Bigg[\int_0^{l} \left(- \rho A \frac{\partial^2 w}{\partial t^2} - EI \frac{\partial^4 w}{\partial x^4} + \frac{\partial^2 T}{\partial x^2} \right) \delta w \; dx + \left(- M_t \frac{\partial^2 w}{\partial t^2} + EI \frac{\partial^3 w}{\partial x^3} - \frac{\partial T}{\partial x} \right) \delta w \Big|_{x=l} + \left(- I_t \frac{\partial^3 w}{\partial x \partial t^2} - EI \frac{\partial^2 w}{\partial x^2} + T \right) \delta \left(\frac{\partial w}{\partial x} \right) \Big|_{x=l} \Bigg] dt = 0 \quad . \tag{A.23}$$

For the variational indicator to vanish for arbitrary variations, δw and $\delta\left(\frac{\partial w}{\partial x}\right)$, then

$$- EI \frac{\partial^4 w}{\partial x^4} - \rho A \frac{\partial^2 w}{\partial t^2} + \frac{\partial^2 T}{\partial x^2} = 0 \qquad \text{for } x: \; 0<x<l \tag{A.24}$$

and

$$\left. \begin{aligned} - I_t \frac{\partial^3 w}{\partial x \partial t^2} - EI \frac{\partial^2 w}{\partial x^2} + T &= 0 \\ - M_t \frac{\partial^2 w}{\partial t^2} + EI \frac{\partial^3 w}{\partial x^3} - \frac{\partial T}{\partial x} &= 0 \end{aligned} \right] \text{for } x=l . \tag{A.25}$$

Combined with the geometric boundary conditions from Eqn. (A.22), Eqns. (A.24) and (A.25) are the equations of motion for the active damper. Substituting for T(x) from Eqn. (A.14) gives the equations of motion in terms of the control voltage. The governing equation is

$$EI \frac{\partial^4 w}{\partial x^4} + \rho A \frac{\partial^2 w}{\partial t^2} = c \frac{\partial^2 V(x,t)}{\partial x^2} \qquad \text{for } x: \; 0<x<l \tag{A.26}$$

with boundary conditions

$$\left. \begin{aligned} w = \frac{\partial w}{\partial x} &= 0 \qquad \text{for } x=0 \\ EI \frac{\partial^2 w}{\partial x^2} &= - I_t \frac{\partial^3 w}{\partial t^2 \partial x} + c \cdot V(x,t) \\ EI \frac{\partial^3 w}{\partial x^3} &= M_t \frac{\partial^2 w}{\partial t^2} + c \cdot \frac{\partial V(x,t)}{\partial x} \end{aligned} \right] \text{for } x=l . \tag{A.27}$$

Notice that the control voltage, V(x,t), acts on both a boundary *and* the interior of the beam. From the governing equation one can see that the PVF_2 is indeed a distributed-parameter actuator.

A.3 Non-dimensionalizing the equations of motion

In this section, the equations of motion are non-dimensionalized so that the results of the analysis can easily be scaled to either the scale model or the Draper test structure. The governing equation and the boundary conditions for the active damper system are given in Eqns. (A.26) and (A.27).

The first step is to non-dimensionalize all the distances by some characteristic distance. The flexible length, l, of the composite beam was chosen for the characteristic distance so the distances x and w become

$$x = \frac{x}{l}$$

$$w = \frac{w}{l} \tag{A.28}$$

where x and w are dimensionless distances. Substituting these variables into the governing equation, Eqn. (A.26), yields

$$\frac{EI}{l^3}\frac{\partial^4 w}{\partial x^4} + \rho A l \frac{\partial^2 w}{\partial t^2} = \frac{c}{l^2}\frac{\partial^2 V(x,t)}{\partial x^2} \qquad \text{for } x: 0<x<1 \ . \tag{A.29}$$

Dividing by $\frac{EI}{l^3}$ yields

$$\frac{\partial^4 w}{\partial x^4} + \frac{\rho A l^4}{EI}\frac{\partial^2 w}{\partial t^2} = \frac{cl}{EI}\frac{\partial^2 V(x,t)}{\partial x^2} \qquad \text{for } x: 0<x<1 \ . \tag{A.30}$$

From the second term, one can see that time can be non-dimensionalized by $\sqrt{\frac{\rho AL^4}{EI}}$, or

$$t = t \cdot \sqrt{\frac{EI}{\rho AL^4}} \tag{A.31}$$

where t is the dimensionless time. Likewise, the second term of Eqn. (A.30) suggests that V be divided by $\frac{EI}{Lc}$ or

$$V(x) = \frac{cL}{EI} V(x,t) \tag{A.32}$$

where V is the dimensionless control voltage. Substituting the dimensionless time and control voltage into Eqn. (A.30) gives

$$\frac{\partial^4 w}{\partial x^4} + \frac{\partial^2 w}{\partial t^2} = \frac{\partial^2 V(x,t)}{\partial x^2} \qquad \text{for } x: \ 0<x<1 \ . \tag{A.33}$$

This governing equation is dimensionless.

Substituting the non-dimensional variables defined in Eqns. (A.28), (A.31), and (A.32) in the boundary conditions, Eqns. (A.27), and rearranging yields

$$\left.\begin{aligned} w &= \frac{\partial w}{\partial x} = 0 \qquad\qquad \text{for } x=0 \\ \frac{\partial^2 w}{\partial x^2} &= \frac{-\,I_t}{\rho A l^3}\frac{\partial^3 w}{\partial t^2 \partial x} + V(x,t) \\ \frac{\partial^3 w}{\partial x^3} &= \frac{M_t}{\rho A l}\frac{\partial^2 w}{\partial t^2} + \frac{\partial V(x,t)}{\partial x} \end{aligned}\right\} \qquad \text{for } x=1 \ . \tag{A.34}$$

The boundary conditions at $x=1$ suggest that the dimensionless tip mass, M_t, and dimensionless tip inertia, I_t, could be defined by

$$\left.\begin{aligned} M_t &= \frac{M_t}{\rho A l} \\ I_t &= \frac{I_t}{\rho A l^3} \end{aligned}\right. \ . \tag{A.35}$$

Using these dimensionless tip parameters in the boundary conditions, the full dimensionless equations of motion are

$$\frac{\partial^4 w}{\partial x^4} + \frac{\partial^2 w}{\partial t^2} = \frac{\partial^2 V(x,t)}{\partial x^2} \qquad \text{for } x: \ 0<x<1 \tag{A.36}$$

with boundary conditions

$$\left.\begin{aligned} w &= \frac{\partial w}{\partial x} = 0 \qquad\qquad \text{for } x=0 \\ \frac{\partial^2 w}{\partial x^2} &= -\,I_t \frac{\partial^3 w}{\partial t^2 \partial x} + V(x,t) \\ \frac{\partial^3 w}{\partial x^3} &= M_t \frac{\partial^2 w}{\partial t^2} + \frac{\partial V(x,t)}{\partial x} \end{aligned}\right\} \qquad \text{for } x=1 \ . \tag{A.37}$$

The dimensionless variables are collected and listed below:

$$
\begin{aligned}
x &= \frac{\mathrm{x}}{l} \quad , \\
w &= \frac{\mathrm{w}}{l} \quad , \\
t &= \mathrm{t}\sqrt{\frac{\mathrm{EI}}{\rho \mathrm{A} l^4}} \quad , \\
V &= \mathrm{V} \cdot \frac{\mathrm{c}l}{\mathrm{EI}} \quad , \\
M_t &= \frac{\mathrm{M_t}}{\rho \mathrm{A} l} \quad , \\
I_t &= \frac{\mathrm{I_t}}{\rho \mathrm{A} l^3} \quad .
\end{aligned}
\tag{A.38}
$$

Appendix B
Determining Mode Shapes

This appendix describes a procedure to find the mode shapes for the cantilever beam. The mode shapes are needed for the simulation algorithm in Section 3.4 Derivations in this appendix use the dimensionless form of all variables unless otherwise specified.

This is a procedure for finding the natural mode shapes (i.e., not forced) of a cantilever beam with both tip mass and tip inertia. The forced system is described by Eqns. (3.12) and (3.13) which are repeated here in homogeneous form (i.e., without the control voltage). The homogeneous system is described by

$$\frac{\partial^4 w}{\partial x^4} + \frac{\partial^2 w}{\partial t^2} = 0 \qquad \text{for } x: \ 0<x<1 \tag{B.1}$$

with boundary conditions

$$\left.\begin{aligned} w &= \frac{\partial w}{\partial x} = 0 \\ \frac{\partial^2 w}{\partial x^2} &= -I_t \frac{\partial^3 w}{\partial t^2 \partial x} \\ \frac{\partial^3 w}{\partial x^3} &= M_t \frac{\partial^2 w}{\partial t^2} \end{aligned}\right] \qquad \begin{aligned} &\text{for } x=0 \\ &\\ &\text{for } x=1 \ . \end{aligned} \tag{B.2}$$

To solve this system, assume separation of variables and a solution of the form

$$w(x,t) = \Phi(x)\, e^{i\omega t} \tag{B.3}$$

where $\Phi(x)$ is the dimensionless mode shape and ω is the dimensionless frequency. Substituting this solution into Eqns. (B.1) and (B.2) and canceling common terms yields

$$\frac{\partial^4 \Phi}{\partial x^4} + \omega^2 \Phi = 0 \qquad \text{for } x: \ 0<x<1 \tag{B.4}$$

with boundary conditions

$$\left.\begin{aligned} \Phi &= \frac{\partial \Phi}{\partial x} = 0 && \text{for } x=0 \\ \frac{\partial^2 \Phi}{\partial x^2} &= I_t\, \omega^2 \frac{\partial \Phi}{\partial x} \\ \frac{\partial^3 \Phi}{\partial x^3} &= -\, M_t\, \omega^2\, \Phi \end{aligned}\right\} \quad \text{for } x=1 \quad . \tag{B.5}$$

Notice that this new system is not a function of time. Now assume a solution of for the mode shape, Φ, of the form

$$\Phi = A\, e^{izx} \tag{B.6}$$

where $z^4 = \omega^2$. This solution can be rearranged to give a different form,

$$\Phi = A \cos(zx) + B \sin(zx) + C \cosh(zx) + D \sinh(zx) \tag{B.7}$$

where A, B, C, and D are constants to be determined by the boundary conditions. This is the classical solution form for the mode shapes of a Bernoulli-Euler beam.

The boundary conditions are applied by substituting the assumed solution for Φ into the boundary conditions. Applying the boundary conditions at $x=0$ to Eqn. (B.7), and rearranging yields

$$\begin{aligned} A + C &= 0 \\ B + D &= 0 \quad . \end{aligned} \tag{B.8}$$

Rewriting Eqn. (B.7) with these results gives

$$\Phi = A\,(\cos(zx) - \cosh(zx)) + B\,(\sin(zx) - \sinh(zx)) \quad . \tag{B.9}$$

Applying the boundary conditions at $x=1$ to Eqn. (B.9) yields

$$\begin{aligned} & z^2\,[-A\,(\cos(z) + \cosh(z)) - B\,(\sin(z) + \sinh(z))\,] = \\ & \quad \omega^2\, I_t\, z\,[-A\,(\sin(z) + \sinh(z)) + B\,(\cos(z) - \cosh(z))\,] \end{aligned}$$

$$\begin{aligned} & z^3\,[\,A\,(\sin(z) - \sinh(z)) - B\,(\cos(z) + \cosh(z))\,] = \\ & \quad -\omega^2\, M_t\,[\,A\,(\cos(z) - \cosh(z)) + B\,(\sin(z) - \sinh(z))] \quad \text{for } x=1 \quad . \end{aligned} \tag{B.10}$$

Grouping terms of A and B together, using $\omega^2 = z^4$, and writing in matrix form gives

$$\begin{bmatrix} -[\cos(z) + \cosh(z)] + I_t z^3[\sin(z) + \sinh(z)] & -[\sin(z) + \sinh(z)] - I_t z^3[\cos(z) - \cosh(z)] \\ [\sin(z) - \sinh(z)] + M_t z[\cos(z) - \cosh(z)] & -[\cos(z) + \cosh(z)] + M_t z[\sin(z) - \sinh(z)] \end{bmatrix}$$

$$\cdot \begin{bmatrix} A \\ B \end{bmatrix} = \underline{0} \qquad \text{for } x=1 \quad . \tag{B.11}$$

For there to be nontrival solutions for A and B then the determinant of the square matrix must be zero. After rearranging and reducing, the determinant is

$$\begin{aligned} \det\begin{bmatrix} \end{bmatrix} &= (1 + M_t I_t z^4) + \cos(z)\cosh(z)\,(1 - M_t I_t z^4) \\ &\quad + \cos(z)\sinh(z)\,(M_t z - I_t z^3) - \cosh(z)\sin(z)\,(M_t z + I_t z^3) \\ &= 0 \qquad \text{for } x=1 \quad . \end{aligned} \tag{B.12}$$

The values of z that satisfy Eqn. (B.12) are the eigenvalues of the system. Notice that these solutions only depend on the dimensionless tip mass and tip inertia, M_t and I_t, respectively. From these eigenvalues, the natural frequencies of the corresponding mode can be found. By substituting the eigenvalues back into Eqn. (B.11) one can solve for B in terms of A (or vice-versa). This determines the mode shape to within an arbitrary constant, A (or B), which will be assumed to be unity. This means that any cantilever beams with the same dimensionless tip mass and tip inertia will have the same eigenvalues and hence the same dimensionless mode shapes. The first mode shape will be found as an example.

First, one must know the dimensionless tip mass and tip inertia. Using the definitions for the dimensionless parameters given in Eqn. (3.9) and the dimensional parameter values for the composite beam given in Table 4-I, the dimensionless tip mass and tip inertia are

$$\begin{aligned} M_t &= \frac{M_t}{\rho A l} = 1.20 \\ I_t &= \frac{I_t}{\rho A l^3} = 3.71\text{x}10^{-3} \quad . \end{aligned} \tag{B.13}$$

Substituting these values into Eqn. (B.12) and performing a numerical search for the zeros gives the results summarized in Table B-I (only the first four modes are included). The dimensionless natural frequency for a mode is found from the relation $\omega_i = z_i^2$. The

dimensional natural frequency can be found by using the same parameter to dimensionalize the frequency as was used to non-dimensionalize time (see either Eqn. (3.9) or Appendix A).

Table B-I: Eigenvalues and Predicted Natural Frequencies.

Mode #	Eigenvalue	Natural frequency for scaled beam (Hz)
1	1.20	6.05
2	3.87	62.9
3	6.34	169
4	8.55	308

To find the mode shape, solve for B in terms of A using one equation of Eqn. (B.11) and use the eigenvalue for the mode of interest. For the first mode, using the first equation of Eqn. (B.11), B is given by

$$B = - A \frac{-(\cos(z) + \cosh(z)) + I_t z^3(\sin(z) + \sinh(z))}{-(\sin(z) + \sinh(z)) - I_t z^3(\cos(z) - \cosh(z))}$$

$$= -0.887 A \quad . \tag{B.14}$$

Substituting this relation into Eqn. (B.9), using the eigenvalue for the mode of interest (first mode in this case), and letting A = 1 yields

$$\Phi = \cos(1.20x) - \cosh(1.20x) - 0.887(\sin(1.20x) - \sinh(1.20x)) \quad . \tag{B.15}$$

This is the dimensionless shape of the first mode.

Appendix C
Dynamic Scaling of a Cantilever Beam

This appendix describes the dimensional analysis used to dynamically scale one of the arms of the Draper test structure (see Figure 2-2) to a smaller, more manageable size. The same techniques were used by Kelley when designing the Draper test structure to ensure that its dynamics would be similar to an actual space structure [1].

Dimensional analysis is a method which reduces the number of variables needed to describe a physical phenomenon and groups them in dimesionless form [26]. The number of variables is reduced by the number of primary quantities or dimensions which govern the phenomenon. In mechanics the primary quantities are mass, length, and time. One benefit of dimensional analysis and having dimensionless parameters is that the dimensionless parameters are independent of changes in the size or units of the primary quantities. For instance, velocity is derived from two primary quantities, length and time. A ratio of two velocities (a dimensionless parameter) is the same whether the units are miles/hr, cm/sec, or light years/century. This means that an equation will give the same results regardless of the units of the primary quantities. This leads to scaling laws between a structure or a device and a model. If a quantity, say a force, is measured on a model, the corresponding force on the structure can be calculated if the scaling laws are valid. The scaling laws are valid if the dimensionless parameters of both the model and the structure are the same.

The unforced equations of motion for the transverse motion of a cantilever beam with a tip mass and tip inertia, shown in Figure C-1, are derived in Appendix A and are repeated here. The governing equation is

$$EI \frac{\partial^4 w}{\partial x^4} + \rho A \frac{\partial^2 w}{\partial t^2} = 0 \qquad \text{for } x\text{: } 0<x<l \tag{C.1}$$

with boundary conditions

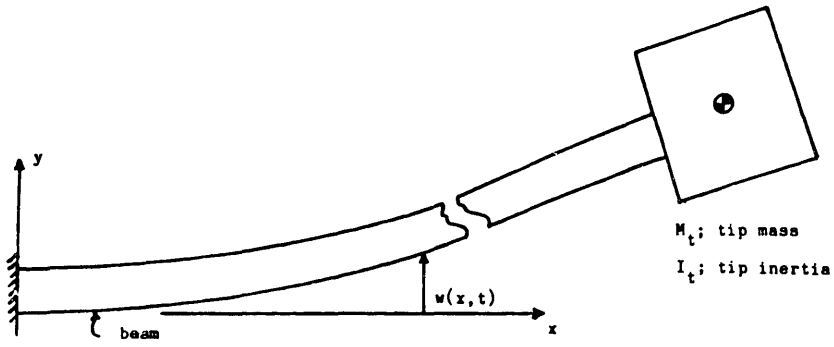

Figure C-1: A cantilever beam with tip mass and tip inertia.

$$\left.\begin{aligned} w &= \frac{\partial w}{\partial x} = 0 && \text{for } x=0 \\ EI\frac{\partial^2 w}{\partial x^2} &= -I_t\frac{\partial^3 w}{\partial t^2 \partial x} \\ EI\frac{\partial^3 w}{\partial x^3} &= M_t\frac{\partial^2 w}{\partial t^2} \end{aligned}\right\} \quad \text{for } x=l \quad . \tag{C.2}$$

Since transverse vibration of a beam is a two dimensional phenomena and the cross-section of the beam is rectangular, these equations can be written in terms of a unit depth beam. This will allow the two dimensional behavior of the beam to be dynamically scaled while letting the depth of the beam be chosen by other considerations. Dividing Eqns. (C.1) and (C.2) by the depth of the beam, b, yields

$$\frac{EI}{b}\frac{\partial^4 w}{\partial x^4} + \frac{\rho A}{b}\frac{\partial^2 w}{\partial t^2} = 0 \quad \text{for } x:\ 0<x<l \tag{C.3}$$

with boundary conditions

$$\left.\begin{aligned} w &= \frac{\partial w}{\partial x} = 0 && \text{for } x=0 \\ \frac{EI}{b}\frac{\partial^2 w}{\partial x^2} &= -\frac{I_t}{b}\frac{\partial^3 w}{\partial t^2 \partial x} \\ \frac{EI}{b}\frac{\partial^3 w}{\partial x^3} &= \frac{M_t}{b}\frac{\partial^2 w}{\partial t^2} \end{aligned}\right\} \quad \text{for } x=l \quad . \tag{C.4}$$

These are the parameters that should be preserved between the test structure and the scale model.

The first step is to non-dimensionalize the equations of motion given by Eqns. (C.3) and (C.4) and/or choose the dimensionless parameters of interest. This can be done in the same manner as in Appendix A which yields

$$\frac{\partial^4 w}{\partial x^4} + \frac{\partial^2 w}{\partial t^2} = 0 \qquad \text{for } x: \ 0<x<1 \tag{C.5}$$

with boundary conditions

$$\left.\begin{aligned} w &= \frac{\partial w}{\partial x} = 0 && \text{for } x=0 \\ \frac{\partial^2 w}{\partial x^2} &= -I_t \frac{\partial^3 w}{\partial t^2 \partial x} \\ \frac{\partial^3 w}{\partial x^3} &= M_t \frac{\partial^2 w}{\partial t^2} \end{aligned}\right\} \quad \text{for } x=1 \tag{C.6}$$

where the dimensionless variables are given by

$$\begin{aligned} x &= \frac{\mathrm{x}}{l} \ , \\ w &= \frac{\mathrm{w}}{l} \ , \\ t &= \mathrm{t} \cdot \sqrt{\frac{\mathrm{EI}}{\rho \mathrm{A} l^4}} \ , \\ V &= \mathrm{V} \cdot \frac{cl}{\mathrm{EI}} \ , \\ M_t &= \frac{\mathrm{M_t}}{\rho \mathrm{A} l} \ , \\ I_t &= \frac{\mathrm{I_t}}{\rho \mathrm{A} l^3} \ . \end{aligned} \tag{C.7}$$

Note that these are the same dimensionless variables as where derived in Appendix A because the division by the depth of the beam cancels with itself.

To obtain the scaling laws for the properties of the cantilever beam, one must first determine the scale factors for each of the primary quantities; mass, length, and time. The following analysis assumes that one is scaling from an existing structure, e.g., an arm of the

Draper test structure, denoted by $(\cdot)_s$ to a scale model denoted by $(\cdot)_m$.

The length of the model beam, l_m, is chosen subject to problem constraints, i.e., limited size of fixture, ease of handling, etc. From this, the length scale factor, S_L, and length ratio, L_m/L_s , are given by

$$S_L = \frac{L_m}{L_s} = \frac{l_m}{l_s} \quad . \tag{C.8}$$

By choosing the material for the model beam, the density ratio, α, is decided and is given by

$$\alpha = \frac{\rho_m}{\rho_s} = \frac{M_m}{M_s} \cdot \left(\frac{l_s}{l_m}\right)^3 \tag{C.9}$$

where M_m/M_s is the mass ratio of the beams since the dimensions of density are mass divided by length cubed. Substituting from Eqn. (C.8) and solving for the mass ratio yields the mass scale factor, S_M, or

$$S_M = \frac{M_m}{M_s} = \alpha\, S_L^{\,3} \quad . \tag{C.10}$$

Choosing the material also determines the modulus ratio, γ, given by

$$\gamma = \frac{E_m}{E_s} = \frac{M_m}{M_s} \cdot \frac{L_s}{L_m} \cdot \left(\frac{T_s}{T_m}\right)^2 \tag{C.11}$$

where E is the Young's modulus and T_s/T_m is the time ratio. Substituting Eqns. (C.8) and (C.10) into Eqn. (C.11) and solving for the time ratio gives the time scale factor, S_T, or

$$S_T = \frac{T_s}{T_m} = \sqrt{\frac{S_M}{S_L\, \gamma}} \quad . \tag{C.12}$$

Having found the primary scaling factors, all the physical quantities can be scaled. For example, to find what the tip mass per unit depth of the model beam, $(I_t/b)_m$, should be, first determine the dimensions of (I_t/b), which are mass times length. Now multiply the $(I_t/b)_s$ by the appropriate primary scale factors, or

$$\left(\frac{I_t}{b}\right)_m = \left(\frac{I_t}{b}\right)_s \cdot S_L \cdot S_M \quad . \tag{C.13}$$

Table C-I shows the relevant physical properties for an arm of the Draper

structure [1, 3] and some of the possible material and length scale combinations for the model cantilever beam. The final design parameters for the scale model beam are shown in Table C-II. Some of the considerations used for choosing the length scale and the material are given in Section 2.2.

Table C-I: Possible choices for the scale model beam.

	Arm of Draper structure [1]	Possible scale models 1	2	3
material	Al	brass	Al	steel
modulus, E (Nm^{-2})	$76x10^9$	$103x10^9$	$76x10^9$	$207x10^9$
density, ρ (kgm^{-3})	2840	8500	2840	7800
length, l (m)	1.22	.305	0.203	.153
thickness, h (mm)	3.18	0.794	0.529	0.397
tip mass per unit depth, M_t/b (kgm^{-1})	13.4	2.51	0.372	0.575
tip inertia per unit depth, I_t/b (kgm)	$6.88x10^{-2}$	$8.04x10^{-4}$	$5.31x10^{-5}$	$4.61x10^{-5}$
length scale factor, S_L	-	.25	0.167	.125
mass scale factor, S_M	-	$4.67x10^{-2}$	$4.63x10^{-3}$	$5.36x10^{-3}$
time scale factor, S_T	-	0.370	0.167	0.125

Table C-II: Final design parameters for the scaled beam.

material	steel
modulus, E (Nm^{-2})	$210x10^{9}$
density, ρ (kgm^{-3})	7800
length, l (m)	0.146
thickness, h (mm)	0.381
depth, b (cm)	1.27
tip mass, M_t (kg)	$6.73x10^{-3}$
tip inertia, I_t (kgm^2)	$5.0x10^{-7}$

Appendix D
Effective Loss Factor from the Decay Envelope of a Free Vibration

This appendix gives the procedure used to determine the effective loss factor of a free vibration from its decay envelope. This is done by reviewing the definition of the loss factor and how it affects the decay envelope for linear viscous damping and then generalizing to the non-linear case. This is closely related to the log-decrement method, which will also be discussed.

A general example of a free vibration is shown in Figure D-1.

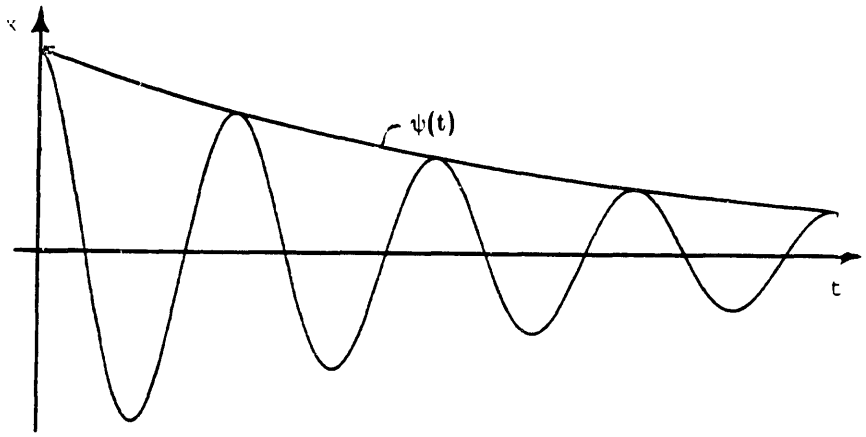

Figure D-1: An example of a free decay vibration.

The state, x(t), oscillates within the decay envelope, $\psi(t)$. Assume for the moment that the vibrations are from a linear system with linear viscous damping. Then the time history of the decay envelope could be described by

$$\psi(t) = \psi_0 \exp\left(\frac{-\eta\omega t}{2} \right) \tag{D.1}$$

for small values of η where η is the loss factor, ω is the frequency of vibration in rad/sec, and ψ_0 is the amplitude of the decay envelope at time t=0. This is the familiar exponential decay envelope.

A common method to determine the damping in a system is to plot the magnitude of the free vibrations on a logarithmic scale, as shown in Figure D-2.

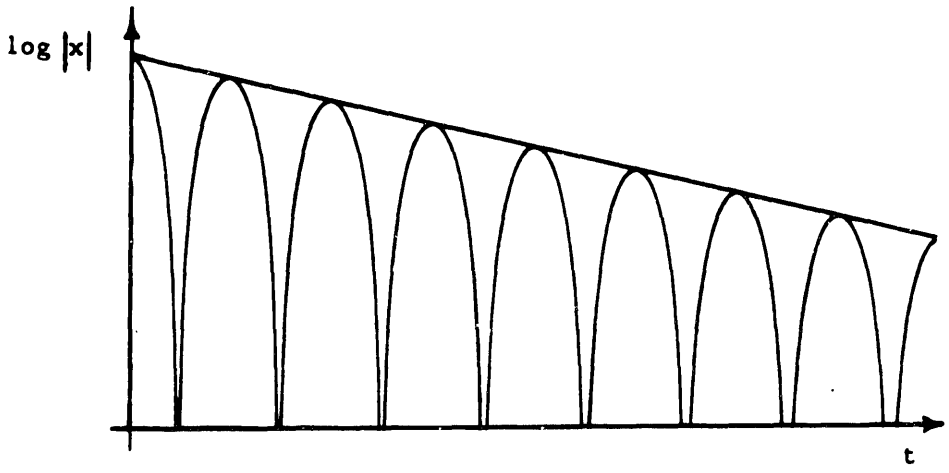

Figure D-2: A free decay vibration plotted on a logarithmic scale.

Taking the natural logarithm (base e) of the decay envelope described by Eqn. (D.1), the decay envelope on a logarithmic scale would be a straight line given by

$$\ln(\psi(t)) = \ln(\psi_0) - \frac{\eta\omega t}{2} \quad . \tag{D.2}$$

The slope (on the logarithmic plot) of the decay envelope is

$$\frac{\partial \ln(\psi)}{\partial t} = -\frac{\eta\omega}{2} \quad . \tag{D.3}$$

If the decay envelope is not a straight line, the damping in the system must be changing (assuming the frequency of vibration is constant). Therefore, for a general free vibration (not necessarily a linear system or linear damping), the loss factor, eta, is given by

$$\eta(t) = \frac{\partial \ln(\psi(t))}{\partial t} \frac{2}{\omega} \quad . \tag{D.4}$$

This provides a means of determining the loss factor from the decay envelope.

A very similar method is to observe both the slope and the magnitude of the decay envelope on a linear scale. The slope of the exponential decay envelope described by Eqn. (D.1) is given by

$$\frac{\partial \psi}{\partial t} = -\psi_0 \frac{\eta\omega}{2} \exp\left(\frac{-\eta\omega t}{2}\right)$$

$$= -\frac{\eta\omega}{2} \psi(t) \quad . \tag{D.5}$$

On a linear scale, the slope of an exponential decay envelope is directly proportional to its magnitude. Solving Eqn. (D.5) for the loss factor, eta, yields

$$\eta(t) = -\frac{\partial \psi(t)}{\partial t} \frac{2}{\psi(t)\omega} \quad . \tag{D.6}$$

If the decay envelope is exponential then $\eta(t)$ is a constant. However, this equation can also be used to determine the loss factor from a general decay envelope (not necessarily exponential).

Eqn. (D.6) is actually equivalent to Eqn. (D.4) because

$$\frac{\partial \ln(\psi(t))}{\partial t} = \frac{\partial \psi(t)}{\partial t} \frac{1}{\eta(t)} \tag{D.7}$$

is a derivative identity. Therefore both equations only provide two different ways to calculate the same value. Eqn. (D.6) was used to calculate the effective loss factor, η_{eff}, for the parameter study in Section 3.5.

Appendix E
Distributed-Parameter Optimal Control for a Cantilever Beam

This appendix describes an attempt to apply the distributed-parameter optimal control formulation described by Tzafestas [13] to a cantilever beam with a torque actuator at the tip. This formulation extends the classical variational calculus approach used in lumped-parameter optimal control to distributed-parameter systems. The beam used in this application does not have a tip mass or tip inertia. It is highly recommended that the reader first refer to Tzafestas [11, 12, 13] and then to this derivation. The majority of the points presented here are covered in [13] but [11] and [12] may provide some needed insight.

E.1 The Control Problem

The equations of motion for transverse motions, w(x,t), of a uniform Bernoulli-Euler cantilever beam with a torque actuator at the tip are given by

$$EI\,\frac{\partial^4 w}{\partial x^4} + \rho A\,\frac{\partial^2 w}{\partial t^2} = \frac{\partial^2 T(x,t)}{\partial x^2} \qquad \text{for } x:\ 0<x<l \tag{E.1}$$

with boundary conditions

$$\left.\begin{aligned} w = \frac{\partial w}{\partial x} &= 0 && \text{for } x=0 \\ EI\,\frac{\partial^2 w}{\partial x^2} &= T(x,t) \\ EI\,\frac{\partial^3 w}{\partial x^3} &= 0 \end{aligned}\right\} \quad \text{for } x=l \tag{E.2}$$

where EI is the bending stiffness of the beam and ρA is its mass per unit length. The control torque $T \in T$ where T is the admissible control space, and is assumed to be open. The interior domain, D, is x: $0<x<l$, and the boundary domain , B, is $x \in 0,l$. Note that the boundary of a one dimensional domain consists of two end points. These can be considered as spatial delta functions.

In preparation for the optimal control formulation, the equations of motion were put in matrix form. For the system to be well-posed [31], a state vector, Y(x,t), was chosen such that

$$\underline{Y}(x,t) = \begin{bmatrix} \text{curvature} \\ \\ \text{velocity} \end{bmatrix} = \begin{bmatrix} \dfrac{\partial^2 w}{\partial x^2} \\ \\ \dfrac{\partial w}{\partial t} \end{bmatrix} . \tag{E.3}$$

Rewriting the system in matrix form yields

$$\frac{\partial \underline{Y}(x,t)}{\partial t} = \begin{bmatrix} 0 & \dfrac{\partial^2(\cdot)}{\partial x^2} \\ \\ \dfrac{-EI}{\rho A}\dfrac{\partial^2(\cdot)}{\partial x^2} & 0 \end{bmatrix} \underline{Y}(x,t) = \underline{F}\,\underline{Y} \qquad \text{for } x \in D \tag{E.4}$$

with boundary conditions

$$\begin{bmatrix} EI\ \delta(x-l) & \delta(x) \\ \\ EI\dfrac{\partial(\cdot)}{\partial x}\delta(x-l) & \dfrac{\partial(\cdot)}{\partial x}\delta(x) \end{bmatrix} \underline{Y} = \begin{bmatrix} \delta(x-l) \\ \\ 0 \end{bmatrix} T \qquad \text{for } x \in B \tag{E.5}$$

where $\underline{F}$ is a linear spatial operator matrix and $\delta(x-z)$ is a spatial delta function at $x=z$. The delta functions must be included to completely describe the boundary conditions in one matrix equation. In Tzafestas' notation, Eqn. (E.5) is given by

$$\underline{\beta Y} = \underline{B}_b T(x) \tag{E.6}$$

where $\underline{\beta}$ is a linear spatial boundary operator matrix and $\underline{B}_b$ is a boundary control distribution matrix. Tzafestas assumes that the boundary operator has the form

$$\underline{\beta}(\cdot) = \underline{A}_{b1}(x,t)(\cdot) + \underline{A}_{b2}(x,t)\frac{\partial(\cdot)}{\partial \sigma} \tag{E.7}$$

where $\dfrac{\partial(\cdot)}{\partial \sigma}$ denotes partial differentiation along the conormal of B relative to $\underline{F}(\cdot)$ [13]. Tzafestas further assumes that $\underline{A}_{b2}$ is nonsingular "without loss of generality" [11]. For a one dimensional system, differentiation along the conormal of the boundary is simply the partial derivative at the boundary [32]. The boundary operator for this case can be written in the form of Eqn. (E.5), or

$$\underline{\beta}(\cdot) = \begin{bmatrix} EI\ \delta(x-\ell) & \delta(x) \\ 0 & 0 \end{bmatrix} (\cdot) + \begin{bmatrix} 0 & 0 \\ EI \dfrac{\partial(\cdot)}{\partial x} \delta(x-\ell) & \dfrac{\partial(\cdot)}{\partial x} \delta(x) \end{bmatrix} \tag{E.8}$$

Note that $\underline{A}_{b2}$ is singular in this case. This singularity will lead to difficulties later in the analysis. It is not known if this is a counter-example for Tzafestas' assumption or if there is some other problem.

E.2 The Cost Functional

A general quadratic cost functional, J, for a distributed-parameter system would be of the form

$$\begin{aligned} J = \int_{t_i}^{t_f} \Bigg[& \frac{1}{2} \int_D \int_D \underline{Y}^T(x_2,t)\underline{Q}(x_1,x_2,t)\underline{Y}(x_1,t)\ dx_1\ dx_2 \\ & + \frac{1}{2} \int_D \int_D \gamma_d\ \underline{U}_d{}^T(x_1,t)\underline{R}_d(x_1,x_2,t)\underline{U}_d(x_2,t)\ dx_1\ dx_2 \\ & + \frac{1}{2} \int_B \int_B \gamma_b\ \underline{U}_b{}^T(x_1,t)\underline{R}_b(x_1,x_2,t)\underline{U}_b(x_2,t)\ dx_1\ dx_2 \Bigg]\ dt \\ = & \int_{t_i}^{t_f} L\ dt \end{aligned} \tag{E.9}$$

where γ_d and γ_b are scalar weightings on the control vectors, $\underline{U}$, $(\cdot)^T$ indicates the transpose of a matrix or vector, $(\cdot)_d$ indicates the interior domain (x: $0<x<\ell$), and $(\cdot)_b$ indicates the boundary. The subscripts on the spatial variable, x, indicate different dummy variables for the integration. The first double integral over the interior domain weights the state vector, $\underline{Y}$, while the second weights the control vector in the domain, $\underline{U}_d$. The boundary double integral weights the boundary control vector, $\underline{U}_b$. The weighting matrices for the states, the interior control, and the boundary control are $\underline{Q}$, $\underline{R}_d$, and $\underline{R}_b$, respectively. $\underline{Q}$ is assumed to be positive semi-definite while $\underline{R}_d$ and $\underline{R}_b$ are assumed positive-definite [11]. The spatial weightings have double integrals to allow spatial crossweights, in the same manner as it is possible to crossweight the states in lumped-parameter systems. L represents the spatial weightings and is integrated from some initial time, t_i, to a final time, t_f, as in lumped-parameter control theroy.

For this problem, the governing equation is homogeneous so there is no control in the

domain. Hence, the domain control weighting term can be dropped from Eqn. (E.9). The control problem is to find the admissible boundary control, $\underline{U}_b(x,t)=T(x,t)$, $x\in B$, $T\in T$, that will minimize the cost functional, J, subject to the constraints of the equations of motion, Eqns. (E.4) and (E.6).

E.3 Finding Canonical Equations

The times t_i and t_f and the states at these times are assumed known. The curve or path described by $Y(x,t)$: $x\in D$ $t\in[t_i,t_f]$ is assumed to be twice continuously differentiable. Introduce an Euler or weak variation in the states, $\delta\underline{Y}$, about the optimizing trajectory, $\underline{Y}^o(x,t)$, such that

$$\underline{Y}(x,t) = \underline{Y}^o(x,t) + \epsilon\underline{\upsilon}(x,t) \tag{E.10}$$

where $\delta\underline{Y}(x,t) = \epsilon\underline{\upsilon}(x,t)$ and $\upsilon(x,t)$ is an arbitrary twice continuously differentiable function subject to boundary conditions. Since the end states are assumed known the variation must vanish, so the time boundary conditions for the variation are

$$\underline{\upsilon}(x,t_i) = \underline{\upsilon}(x,t_f) = 0 \quad . \tag{E.11}$$

The spatial boundary conditions can be found from Eqn. (E.6) by

$$\begin{aligned} \underline{\beta Y}(x,t) - \underline{B}_b T^o(x,t) &= \underline{\beta}(\ \underline{Y}^o(x,t) + \epsilon\underline{\upsilon}(x,t)\ ) - \underline{B}_b T^o(x,t) \\ &= \underline{\beta Y}^o(x,t) - \underline{B}_b T^o(x,t) + \epsilon\underline{\beta\upsilon}(x,t) \\ &= 0 \quad x\in B \quad \epsilon\to 0 \end{aligned} \tag{E.12}$$

where T^o is the optimal control. But, since $\underline{B}_b\underline{Y}^o(x,t) - \underline{B}_b T^o(x,t) = 0$ from Eqn. (E.6), then

$$\underline{\beta\upsilon}(x,t) = 0 \quad x\in B \quad . \tag{E.13}$$

Now the cost functional, J, is modified to reflect the homogeneous governing equation and to introduce two lagrange multiplier vectors, $\underline{\lambda}$, for the constraints; one in the interior domain, the other on the boundary, or

$$J_1 = \int_{t_i}^{t_f} \Big[\frac{1}{2} \int_D \int_D \underline{Y}^T(x_2,t)\underline{Q}(x_1,x_2,t)\underline{Y}(x_1,t)\, dx_1\, dx_2 + \frac{1}{2} \int_B \int_B \gamma_b\, \underline{U}_b^T(x_1,t)\underline{R}_b(x_1,x_2,t)\underline{U}_b(x_2,t)\, dx_1\, dx_2 + \int_D \underline{\lambda}_d^T(x_1,t)\Big(\frac{-\partial \underline{Y}(x_1,t)}{\partial t} + \underline{F}\, \underline{Y}(x_1,t)\Big)\, dx_1 + \int_B \underline{\lambda}_b^T(x_1,t)(\, \underline{\beta Y}(x_1,t) - \underline{B}_b T(x_1,t)\,)\, dx_1 \Big]\, dt \quad . \tag{E.14}$$

By definition $\underline{Y}^o$ is an optimizing curve if the weak variation (or differential) of the cost functional J_1 is zero, or

$$\frac{\partial J_1}{\partial \delta \underline{Y}} = \frac{\partial J_1}{\partial \epsilon} = \int_{t_i}^{t_f} \Big[\int_D \int_D \underline{Y}^T(x_2,t)\underline{Q}(x_1,x_2,t)\underline{\upsilon}(x_1,t)\, dx_1\, dx_2 + \int_D \underline{\lambda}_d^T(x_1,t)\, \frac{-\partial \underline{\upsilon}(x_1,t)}{\partial t}\, dx_1 + \int_D \underline{\lambda}_d^T(x_1,t)\underline{F\upsilon}(x_1,t)\, dx_1 + \int_B \underline{\lambda}_b^T(x_1,t)\, \underline{\beta \upsilon}(x_1,t)\, dx_1 \Big]\, dt \tag{E.15}$$

$$= 0 \quad .$$

The second term in Eqn. (E.15) can be integrated by parts with respect to time to yield

$$\int_D \int_{t_i}^{t_f} \underline{\lambda}_d^T(x_1,t)\, \frac{-\partial \underline{\upsilon}(x_1)}{\partial t}\, dt\, dx_1 = \int_D \int_{t_i}^{t_f} \frac{\partial \underline{\lambda}_d^T(x_1,t)}{\partial t}\, \underline{\upsilon}(x_1,t)\, dt\, dx_1 \tag{E.16}$$

using the temporal boundary conditions for the variation from Eqn. (E.11). The fourth term in Eqn. (E.15) is on the boundary and must satify the spatial boundary conditions on the variation from Eqn. (E.13). Therefore the fourth term is zero.

Tzafestas uses an extended Green's theorem on the third term in Eqn. (E.15). Here is where the assumption of a non-singular A_{b2} matrix in the boundary operator is used. Since A_{b2} is singular in this case, Tzafestas' formulation cannot be followed directly. However, one can expand the matrix notation, use Green's theorem on each equation, and recombine the results into matrix form to find the adjoint operators [33]. Expanding the matrix notation for the third term yields

$$\int_D \underline{\lambda}_d{}^T \underline{F}\underline{\upsilon}\, dx_1 = \int_D \underline{\lambda}_d{}^T \begin{bmatrix} 0 & \dfrac{\partial^2(\cdot)}{\partial x^2} \\ \dfrac{-EI}{\rho A}\dfrac{\partial^2(\cdot)}{\partial x^2} & 0 \end{bmatrix} \underline{\upsilon}(x_1,t)\, dx_1$$

$$= \int_D \lambda_{d1} \frac{\partial^2 \upsilon_2}{\partial x_1^2} - \lambda_{d2} \frac{EI}{\rho A} \frac{\partial^2 \upsilon_1}{\partial x_1^2}\, dx_1 \qquad \text{(E.17)}$$

where $(\cdot)_i$ denotes an element of a vector. Green's theorem for a one dimensional domain is simply integration by parts twice. Integrating both terms in Eqn. (E.17) by parts twice gives

$$\int_D \underline{\lambda}_d{}^T \underline{F}\underline{\upsilon}\, dx_1 = \int_D \frac{\partial^2 \lambda_{d1}}{\partial x_1^2} \upsilon_2 - \frac{EI}{\rho A} \frac{\partial^2 \lambda_{d2}}{\partial x_1^2} \upsilon_1\, dx_1$$

$$+ \left[\lambda_{d1} \frac{\partial \upsilon_2}{\partial x_1} - \frac{\partial \lambda_{d1}}{\partial x_1} \upsilon_2 - \frac{EI}{\rho A} \left[\lambda_{d2} \frac{\partial \upsilon_1}{\partial x_1} - \frac{\partial \lambda_{d2}}{\partial x_1} \upsilon_1 \right] \right]_{x_1=0}^{l} . \qquad \text{(E.18)}$$

Putting this result back into matrix form yields

$$\int_D \underline{\lambda}_d{}^T \underline{F}\underline{\upsilon}\, dx_1 = \int_D \left[\begin{bmatrix} 0 & \dfrac{-EI}{\rho A}\dfrac{\partial^2(\cdot)}{\partial x_1^2} \\ \dfrac{\partial^2(\cdot)}{\partial x_1^2} & 0 \end{bmatrix} \underline{\lambda}_d(x_1,t) \right]^T \underline{\upsilon}(x_1,t)\, dx_1$$

$$+ \underline{\lambda}_d{}^T(x_1) \begin{bmatrix} 0 & 1 \\ \dfrac{-EI}{\rho A} & 0 \end{bmatrix} \frac{\partial \underline{\upsilon}(x_1)}{\partial x_1} - \frac{\partial \underline{\lambda}_d{}^T(x_1)}{\partial x_1} \begin{bmatrix} 0 & 1 \\ \dfrac{-EI}{\rho A} & 0 \end{bmatrix} \underline{\upsilon}(x_1) \Bigg|_{x_1=0}^{l} . \qquad \text{(E.19)}$$

In Tzafestas' notation,

$$\begin{bmatrix} 0 & \dfrac{-EI}{\rho A}\dfrac{\partial^2(\cdot)}{\partial x_1^2} \\ \dfrac{\partial^2(\cdot)}{\partial x_1^2} & 0 \end{bmatrix} = \underline{F}^* \qquad \text{(E.20)}$$

which is the adjoint operator of $\underline{F}$, and

$$\begin{bmatrix} 0 & 1 \\ \dfrac{-EI}{\rho A} & 0 \end{bmatrix} = \underline{A}_\sigma . \qquad \text{(E.21)}$$

The spatial boundary conditions for the variation given in Eqn. (E.13) are applied to Eqn. (E.19). This is most easily done by expanding the matrix notation for both equations,

applying the boundary conditions, and putting the results back in matrix notation. The boundary terms in Eqn. (E.19) become

$$\left[\underline{\lambda}_d^T(x)\underline{A}_\sigma \frac{\partial \underline{v}(x)}{\partial x} - \frac{\partial \underline{\lambda}_d^T(x)}{\partial x} \underline{A}_\sigma \underline{v}(x) \right]\Big|_{x_1=0}^{l} \tag{E.22}$$

$$= \underline{\lambda}_d^T(x) \begin{bmatrix} 0 & \delta(x-l) \\ \frac{-EI}{\rho A}\delta(x) & 0 \end{bmatrix} \frac{\partial \underline{v}(x)}{\partial x} - \frac{\partial \underline{\lambda}_d^T(x)}{\partial x} \begin{bmatrix} 0 & \delta(x-l) \\ \frac{-EI}{\rho A}\delta(x) & 0 \end{bmatrix} \underline{v}(x) \Big|_{x=0}^{l} .$$

Substitute Eqns. (E.16), (E.19), and (E.22) into the variation of the cost function, Eqn. (E.15). Using the fact that the fourth term in the variation must be zero and rearranging yields

$$\frac{\partial J_1}{\partial \varepsilon \underline{Y}} = \int_{t_i}^{t_f} \left[\int_D \left(\int_D \underline{Y}^T(x_2)\underline{Q}(x_1,x_2)\, dx_2 + \frac{\partial \underline{\lambda}_d^T(x_1)}{\partial x_1} + \underline{\lambda}_d^T(x_1)\underline{F}^{*T} \right) \underline{v}(x_1)\, dx_1 \right.$$

$$+ \underline{\lambda}_d^T(x_1) \begin{bmatrix} 0 & \delta(x_1-l) \\ \frac{-EI}{\rho A}\delta(x_1) & 0 \end{bmatrix} \frac{\partial \underline{v}(x_1)}{\partial x_1} - \frac{\partial \underline{\lambda}_d^T(x_1)}{\partial x_1} \begin{bmatrix} 0 & \delta(x_1-l) \\ \frac{-EI}{\rho A}\delta(x_1) & 0 \end{bmatrix} \underline{v}(x_1) \Big|_{x_1=0}^{l} \Bigg] dt \tag{E.23}$$

$$= 0$$

where $\underline{F}^{*T}$ operates to the left. Since the variation v is assumed arbitrary, $\frac{\partial \underline{v}(x_1)}{\partial x_1}$ is also assumed to be arbitrary, subject to the boundary conditions which have already been applied. Applying the fundamental theorem of calculus of variations to Eqn. (E.23) then

$$\frac{\partial \underline{\lambda}_d(x_1)}{\partial x_1} + \underline{F}^* \underline{\lambda}_d(x_1) + \int_D \underline{Q}(x_1,x_2)\underline{Y}(x_2)\, dx_2 = \underline{0} \qquad \text{for } x_1 \in D \tag{E.24}$$

using the assumption that $\underline{Q}$ is symmetric, and the boundary terms give

$$\begin{bmatrix} \delta(x_1-l) & \frac{EI}{\rho A}\delta(x_1) \\ \frac{\partial(\cdot)}{\partial x_1}\delta(x_1-l) & \frac{EI\partial(\cdot)}{\rho A \partial x_1}\delta(x_1) \end{bmatrix} \underline{\lambda}_d(x) = \underline{0} = \underline{\beta}^* \underline{\lambda}_d(x) \tag{E.25}$$

$$\text{for } x \in B$$

where $\underline{\beta}^*$ represents the adjoint boundary operator. In applying the fundamental theorem to the boundary terms, the matrix notation was first expanded, the fundamental theorem was

applied, and then the results were recombined back into matrix notation. Eqns. (E.24) and (E.25) are the canonical relations needed to minimize J_1 with respect to the state vector, $\underline{Y}$.

Now proceed to find the canonical relations for all the other variables in J_1; $\underline{\lambda}_d$, $\underline{\lambda}_b$, and T. This yields:

$\underline{\lambda}_d$: Allow a variation $\delta\underline{\lambda}_d$

$$\frac{\partial J_1}{\partial \delta \underline{\lambda}_d} = \int_{t_i}^{t_f} \int_D \left(\frac{-\partial \underline{Y}(x)}{\partial t} + \underline{F}\ \underline{Y}(x) \right)^T \delta\underline{\lambda}_d(x)\ dx\ \ dt$$

$$= 0$$

or

$$\frac{-\partial \underline{Y}(x)}{\partial t} + \underline{F} = \underline{0} \quad \text{for } x \in D \ . \tag{E.26}$$

$\underline{\lambda}_b$: Allow a variation $\delta\underline{\lambda}_b$,

$$\frac{\partial J_1}{\partial \delta \underline{\lambda}_b} = \int_{t_i}^{t_f} \int_B [\ \underline{\beta Y}(x) - \underline{B}_b T(x)\ ]^T\ \delta\underline{\lambda}_b(x)\ dx\ \ dt$$

$$= 0$$

or

$$\underline{\beta Y}(x) - \underline{B}_b T(x) = \underline{0} \quad \text{for } x \in B \ . \tag{E.27}$$

T: Allow a variation δT,

$$\frac{\partial J_1}{\partial \delta T} = \int_{t_i}^{t_f} \int_B \left(\int_B \gamma_b\ \underline{R}_b(x_1,x_2)\underline{U}_b(x_2)\ dx_2 \ - \underline{B}_b{}^T(x_1)\underline{\lambda}_b(x_1) \right)^T \delta T(x_1)\ \ dx_1\ \ dt$$

$$= 0$$

or

$$\int_B \gamma_b\ \underline{R}_b(x_1,x_2)\underline{U}_b(x_2)\ dx_2 \ - \underline{B}_b{}^T(x_1)\underline{\lambda}_b(x_1) = \underline{0} \qquad \text{for } x_1 \in B \tag{E.28}$$

where $\underline{B}_b$ is assumed to be purely algebraic operator.

Tzafestas introduces the concept of a generalized inverse matrix as defined by

$$\int_D \underline{C}(x_1,x_2,t)\ \underline{C}^{\dagger}(x_2,x_3,t)\ dx_2 \ = \underline{I}\ \delta(x_1-x_3) \tag{E.29}$$

where $\underline{C}^{\dagger}$ is the inverse of $\underline{C}$ and $\underline{I}$ is the identity matrix [11]. This is used to solve Eqn. (E.28) for the optimal control torque, T^{o}, which is given by

$$T^{o}(x_2) = \frac{1}{\gamma_b} \int_B \underline{R}^{\dagger}(x_1,x_2)\ \underline{B}_b{}^{T}(x_1)\underline{\lambda}_b(x_1)\ dx_1 \qquad \text{for } x_2 \in B \ . \tag{E.30}$$

Eqns. (E.24), (E.25), (E.26), (E.27), and (E.30) are the independent canonical relations needed to solve the control problem. However, there is not an independent relation for $\underline{\lambda}_b$. As Tzafestas notes, an independent equation for $\underline{\lambda}_b$ is not expected because the governing equation and boundary conditions for the original problem, Eqns. (E.4) and (E.5), are not independent. At this point Tzafestas determines a 'compatibility factor', $\underline{K}(x)$, such that

$$\underline{\lambda}_b(x) = \underline{K}(x)\ \underline{\lambda}_d(x) \quad \text{for } x \in B \ . \tag{E.31}$$

Again, one cannot follow Tzafestas' formulation exactly due to the singular matrices, but may do something similar. Using Eqn. (E.13)

$$\underline{\lambda}_b{}^{T}(x)\ \beta\underline{\upsilon}(x) = \underline{0} \qquad \text{for } x \in B \ . \tag{E.32}$$

An equation involving $\underline{\lambda}_d$ on the boundary is found from Eqn. (E.23). The boundary terms in Eqn. (E.23) must be zero to minimize J_1, or

$$\underline{\lambda}_d{}^{T}(x) \begin{bmatrix} 0 & \delta(x-l) \\ \dfrac{-EI}{\rho A}\,\delta(x) & 0 \end{bmatrix} \frac{\partial \underline{\upsilon}(x)}{\partial x} - \frac{\partial \underline{\lambda}_d{}^{T}(x)}{\partial x} \begin{bmatrix} 0 & \delta(x-l) \\ \dfrac{-EI}{\rho A}\,\delta(x) & 0 \end{bmatrix} \underline{\upsilon}(x) \Big|_{x_1=0}^{l} \tag{E.33}$$

$$= 0 \qquad \text{for } x \in B \ .$$

Applying the adjoint boundary conditions from Eqn. (E.25), expanding the matrix notation of Eqns. (E.32) and (E.33), and comparing like terms of υ_1 and υ_2, the elements of the variation vector, yields

$$\left.\begin{aligned} EI\,\lambda_{b1}\upsilon_1 &= \frac{EI}{\rho A}\frac{\partial\lambda_{d2}}{\partial x}\upsilon_1 \\ EI\,\lambda_{b2}\frac{\partial\upsilon_1}{\partial x} &= \frac{-EI}{\rho A}\lambda_{d2}\frac{\partial\upsilon_1}{\partial x} \end{aligned}\right] \quad x=l$$

$$\left.\begin{aligned} \lambda_{b1}\upsilon_2 &= \frac{\partial\lambda_{d1}}{\partial x}\upsilon_2 \\ \lambda_{b2}\frac{\partial\upsilon_2}{\partial x} &= -\lambda_{d1}\frac{\partial\upsilon_2}{\partial x} \end{aligned}\right] \quad x=0 \quad . \tag{E.34}$$

Canceling like terms and rewriting this result in matrix form gives

$$\underline{\lambda}_b(x) = \begin{bmatrix} \frac{\partial(\cdot)}{\partial x}\delta(x) & \frac{1}{\rho A}\frac{\partial(\cdot)}{\partial x}\delta(x-l) \\ -\delta(x) & \frac{-1}{\rho A}\delta(x-l) \end{bmatrix} \underline{\lambda}_d(x) \tag{E.35}$$

$$= \underline{K}(x)\,\underline{\lambda}_d(x) \qquad \text{for } x\in B$$

which is the desired compatibility factor. This completes the set of required canonical relations.

E.4 Forming the Distributed-Parameter Riccati Equation

Collected together, the canonical equations are:

$$\frac{\partial \underline{\lambda}_d(x_1)}{\partial t} + \underline{F}^* \underline{\lambda}_d(x_1) + \int_D \underline{Q}(x_1,x_2)\underline{Y}(x_2)\, dx_2 = \underline{0} \qquad \text{for } x_1 \in D\ , \tag{E.24}$$

$$\underline{\beta}^* \underline{\lambda}_d(x) = \underline{0} \qquad \text{for } x \in B\ , \tag{E.25}$$

$$\frac{-\partial \underline{Y}(x)}{\partial t} + \underline{F}\ \underline{Y}(x) = \underline{0} \qquad \text{for } x \in D\ , \tag{E.26}$$

$$\underline{\beta Y}(x) - \underline{B}_b T(x) = \underline{0} \qquad \text{for } x \in B\ , \tag{E.27}$$

$$T^o(x_2) = \frac{1}{\gamma_b} \int_B \underline{R}^\dagger(x_1,x_2)\ \underline{B}_b{}^T(x_1)\ \underline{\lambda}_b(x_1)\, dx_1 \qquad \text{for } x_2 \in B\ , \tag{E.30}$$

$$\underline{\lambda}_b(x) = \underline{K}(x)\ \underline{\lambda}_d(x) \qquad \text{for } x \in B\ . \tag{E.35}$$

Assume a feedback solution of the form

$$\underline{\lambda}_d(x_1,t) = \int_D \underline{S}(x_1,x_2,t)\ \underline{Y}(x_2,t)\, dx_2 \qquad \text{for } x_1 \in D \tag{E.36}$$

where $\underline{S}$ is a feedback gain matrix and is assumed to be symmetric, as in lumped-parameter control theory. Taking the time derivative of this assumed solution gives

$$\frac{\partial \underline{\lambda}_d(x_1)}{\partial t} = \int_D \frac{\partial \underline{S}(x_1,x_2)}{\partial t}\ \underline{Y}(x_2)\, dx_2 + \int_D \underline{S}(x_1,x_2)\ \frac{\partial \underline{Y}(x_2)}{\partial t}\, dx_2 \qquad \text{for } x_1 \in D\ . \tag{E.37}$$

Substituting from Eqn. (E.26) into the second integral in Eqn. (E.37) yields

$$\frac{\partial \underline{\lambda}_d(x_1)}{\partial t} = \int_D \frac{\partial \underline{S}(x_1,x_2)}{\partial t}\ \underline{Y}(x_2)\, dx_2 + \int_D \underline{S}(x_1,x_2)\ \underline{F}\ \underline{Y}(x_2)\, dx_2 \qquad \text{for } x_1 \in D\ . \tag{E.38}$$

The goal is to manipulate this equation into a form that can be compared with Eqn. (E.24). To do this, one must use Green's theorem on the second integral in Eqn. (E.38) so that there are no operators on the state vector, $\underline{Y}$.

The most straightforward way of doing this is to expand the matrix notation of the second term and apply a one dimensional Green's theorem to each equation, as was done when reducing the variation of the cost function, Eqn. (E.18). This yields

$$\int_D \underline{S}(x_1,x_2)\,\underline{F}\,\underline{Y}(x_2)\,dx_2 = \int_D \begin{bmatrix} \frac{\partial^2 S_{11}}{\partial x_2^2}\,Y_2(x_2) - \frac{EI}{\rho A}\frac{\partial^2 S_{12}}{\partial x_2^2}\,Y_1(x_2) \\ \frac{\partial^2 S_{21}}{\partial x_2^2}\,Y_2(x_2) - \frac{EI}{\rho A}\frac{\partial^2 S_{22}}{\partial x_2^2}\,Y_1(x_2) \end{bmatrix} dx_2$$

$$+ \int_B \begin{bmatrix} S_{11}\frac{\partial Y_2(x_2)}{\partial x_2} - \frac{\partial S_{11}}{\partial x_2}\,Y_2(x_2) - \frac{EI}{\rho A}\left[S_{12}\frac{\partial Y_1(x_2)}{\partial x_2} - \frac{\partial S_{12}}{\partial x_2}\,Y_1(x_2)\right] \\ S_{21}\frac{\partial Y_2(x_2)}{\partial x_2} - \frac{\partial S_{21}}{\partial x_2}\,Y_2(x_2) - \frac{EI}{\rho A}\left[S_{22}\frac{\partial Y_1(x_2)}{\partial x_2} - \frac{\partial S_{22}}{\partial x_2}\,Y_1(x_2)\right] \end{bmatrix} (\delta(x_2-l) - \delta(x_2))\,dx_2 \tag{E.39}$$

for $x_1 \in D$ where S_{ij} are the elements of the gain matrix and the boundary terms are subject to both the state and adjoint boundary conditions, Eqns. (E.6) and (E.25), respectively.

Substituting the assumed solution for $\underline{\lambda}_d$ into the adjoint boundary condition, Eqn. (E.25), gives

$$\underline{\beta}^*\underline{\lambda}_d(x_1) = \int_D \underline{\beta}^*(x_1)\underline{S}(x_1,x_2)\underline{Y}(x_2)\,dx_2 \tag{E.40}$$

$$= 0 \qquad \text{for } x_1 \in B \ .$$

Since this integral must equal zero and there is no constraint on the state vector to insure this, it must be that

$$\underline{\beta}^*(x_1)\underline{S}(x_1,x_2) = \begin{bmatrix} S_{11}\delta(x_1-l) + S_{21}\delta(x_1) & S_{12}\delta(x_1-l) + S_{22}\delta(x_1) \\ \frac{\partial S_{11}}{\partial x_1}\,\delta(x_1-l) + \frac{\partial S_{21}}{\partial x_1}\,\delta(x_1) & \frac{\partial S_{12}}{\partial x_1}\,\delta(x_1-l) + \frac{\partial S_{22}}{\partial x_1}\,\delta(x_1) \end{bmatrix} \tag{E.41}$$

$$= \underline{0} \qquad \text{for } x_1 \in B,\ x_2 \in D \ .$$

These are the adjoint boundary conditions to be applied to Eqn. (E.39). Doing so and rewriting the integral in matrix form yields

$$\int_D \underline{S}(x_1,x_2)\,\underline{F}\,\underline{Y}(x_2)\,dx_2 = \int_D \underline{S}(x_1,x_2)\,\underline{F}\,\underline{Y}(x_2)\,dx_2$$

$$+ \int_B \begin{bmatrix} -\left(S_{11}\dfrac{\partial Y_2(x_2)}{\partial x_2} - \dfrac{\partial S_{11}}{\partial x_2} Y_2(x_2) \right) \delta(x_2) \\ \dfrac{-EI}{\rho A}\left(S_{22}\dfrac{\partial Y_1(x_2)}{\partial x_2} - \dfrac{\partial S_{22}}{\partial x_2} Y_1(x_2) \right) \delta(x_2-l) \end{bmatrix} dx_2 \quad . \tag{E.42}$$

Expanding the state vector boundary conditions, Eqn. (E.6) becomes

$$Y_2(x) = \frac{\partial Y_2(x)}{\partial x} = 0 \qquad \text{for } x=0,$$

$$\left.\begin{aligned} EI\ Y_1(x) &= T(x) \\ EI\ \frac{\partial Y_1(x)}{\partial x} &= 0 \end{aligned}\right] \quad \text{for } x=l \quad . \tag{E.43}$$

Substituting these boundary conditions into Eqn. (E.42) gives

$$\int_D \underline{S}(x_1,x_2)\,\underline{F}\,\underline{Y}(x_2)\,dx_2 = \int_D \underline{S}(x_1,x_2)\,\underline{F}^{*T}\,\underline{Y}(x_2)\,dx_2$$

$$+ \int_B \begin{bmatrix} 0 \\ \dfrac{1}{\rho A}\dfrac{\partial S_{22}(x_1,x_2)}{\partial x_2}\,\delta(x_2-l) \end{bmatrix} T(x_2)\,dx_2 \qquad \text{for } x_1 \in D \quad . \tag{E.44}$$

The integral over the boundary terms is included for completeness only. There are no nonzero terms at x=0. This completes the application of Green's theorem to the second integral in Eqn. (E.38).

Substituting this result back into Eqn. (E.38) and substituting for the optimal control torque from Eqn. (E.30) yields

$$\frac{\partial \underline{\lambda}_d(x_1)}{\partial t} = \int_D \frac{\partial \underline{S}(x_1,x_2)}{\partial t}\,\underline{Y}(x_2)\,dx_2 + \int_D \underline{S}(x_1,x_2)\,\underline{F}^{*T}\,\underline{Y}(x_2)\,dx_2$$

$$+ \int_B \int_B \begin{bmatrix} 0 \\ \dfrac{1}{\rho A}\dfrac{\partial S_{22}(x_1,x_2)}{\partial x_2}\,\delta(x_2-l) \end{bmatrix} \frac{1}{\gamma_b}\,\underline{R}_b^{\dagger}(x_3,x_2)\,\underline{B}_b^{T}(x_3)\,\underline{\lambda}_b(x_3)\,dx_2\,dx_3 \tag{E.45}$$

for $x_1 \in D$. Substituting for $\underline{\lambda}_b$ from Eqn. (E.35) and for $\underline{\lambda}_d$ from Eqn. (E.36) gives

$$\frac{\partial \underline{\lambda}_d(x_1)}{\partial t} = \int_D \frac{\partial \underline{S}(x_1,x_2)}{\partial t} \underline{Y}(x_2)\, dx_2 + \int_D \underline{S}(x_1,x_2)\, \underline{F}^{*T}\, \underline{Y}(x_2)\, dx_2$$

$$+ \int_D \int_B \int_B \begin{bmatrix} 0 \\ \frac{1}{\rho A} \frac{\partial S_{22}(x_1,x_2)}{\partial x_2} \delta(x_2 - l) \end{bmatrix} \frac{1}{\gamma_b} \underline{R}_b^{\dagger}(x_3,x_2)\, \underline{B}_b^{T}(x_3)\, \underline{K}(x_3)\, \underline{S}(x_3,x_4) \cdot \underline{Y}(x_4)\, dx_2\, dx_3\, dx_4 \quad \text{for } x_1 \in D . \tag{E.46}$$

Now one can compare Eqn. (E.46) with Eqn. (E.24). Substituting the assumed solution for l_d into Eqn. (E.24), comparing the kernels of the outermost integrals over the interior domain, and rearranging yields

$$\frac{-\partial \underline{S}(x_1,x_2)}{\partial t} = \underline{F}^{*}\underline{S}(x_1,x_2) + \underline{S}(x_1,x_2)\underline{F}^{*T} + \underline{Q}(x_1,x_2)$$

$$+ \int_B \int_B \begin{bmatrix} 0 \\ \frac{1}{\rho A} \frac{\partial S_{22}(x_1,x_4)}{\partial x_4} \delta(x_4 - l) \end{bmatrix} \frac{1}{\gamma_b} \underline{R}_b^{\dagger}(x_3,x_4)\, \underline{B}_b^{T}(x_3)\, \underline{K}(x_3)\, \underline{S}(x_3,x_2)\, dx_3\, dx_4 \tag{E.47}$$

for x_1, $x_2 \in D$ where the dummy variables for integration in the boundary term have been changed. This is a distributed-parameter Riccati equation. It is very similar to Tzafestas' result but is not quite the same due to the differences in the derivation because of the singular matrices in the boundary operator, $\underline{\beta}(x)$. For example, the kernel for the boundary integrals here does not have the symmetry of that in Tzafestas' Riccati equation. After solving the Riccati equation for $\underline{S}(x_1,x_2,t)$ then Eqns. (E.36), (E.35), and (E.30) are used to determine the overall gains for the optimal feedback torque. No dedicated attempt was made to solve this Riccati equation.

E.5 Possible Weighting Matrices

In this section, one set of possible weighting matrices is described. Let the state weighting matrix, $\underline{Q}$, be given by

$$\underline{Q}(x_1,x_2) = \begin{bmatrix} Q_{11}\delta(x_1-x_2) & 0 \\ 0 & Q_{22}\delta(x_1-x_2) \end{bmatrix} \qquad \text{for } x_1,\ x_2 \in D \tag{E.48}$$

which weights the square of the states without any spatial crossweighting. Q_{11} and Q_{22} are scalars. Let the boundary control weighting matrix, $\underline{R}_b$, be given by

$$R_b(x1,x2) = [\ R_1\delta(x_1-x_2)\ ] \qquad \text{for } x_1,\ x_2 \in B \tag{E.49}$$

which weights the square of the torque at the boundary without any spatial crossweighting. R_1 is a scalar. Both $\underline{Q}$ and $\underline{R}_b$ are time invariant.

E.6 Possible Problems with this Formulation

Several questions were raised during this derivation. The first question arose while finding the Riccati equation. When applying Green's theorem to the second integral in Eqn. (E.38) while finding the Riccati equation, the Green's theorem yielded boundary terms like

$$\frac{\partial S_{11}(x_1,x_2)}{\partial x_2}\, Y_2(x_2) \qquad \text{for } x_1 \in D,\ x_2 \in B \tag{E.50}$$

which is taken from Eqn. (E.39). The adjoint boundary conditions applied to Eqn. (E.39) had terms like

$$\frac{\partial S_{11}(x_1,x_2)}{\partial x_1}\, \delta(x_1-l) = 0 \qquad \text{for } x_1 \in B,\ x_2 \in D\ . \tag{E.51}$$

which is taken from Eqn. (E.41). Note that the derivatives are with respect to different dummy variables, although the domains for the derivative variables are the same. Was it allowable to use such boundary conditions in Eqn. (E.51) to cancel the boundary terms in Eqn. (E.50)?

The second question concerns the general properties of $\underline{S}$. Although it is assumed that $\underline{S}$ is symmetric, does this imply anything about the spatial symmetry of its elements, i.e., $\underline{S}(x_1,x_2)$ vs. $\underline{S}(x_2,x_1)$. Any additional information about $\underline{S}$ may help in solving the Riccati equation, and may give the answer to the first question.

References

1. Kelley, M. G., "Mechanical Design and Dynamic Scaling Considerations of a Flexible Spacecraft Test Model", Combined Bachelor's and Master's thesis, Massachusetts Institute of Technology, June, 1983, Also Draper Laboratory report CDSL-T-815.

2. "Kynar Piezo Film", Product information from the Pennwalt Corp., King of Prussia, PA., 1983.

3. Kelley, M. G., W. Podgorski, and J. E. Hubbard, Jr., Mechanical Design of a Flexible Spacecraft Test Model for Active Vibration Control, AIAA preprint no. AIAA-84-1048-CP.

4. Balas, M., "Feedback Control of Flexible Systems", *IEEE Transactions Automatic Control*, Vol. AC-23, August, 1978, pp. 673-679.

5. Ahmed, N. U., and K. L. Teo, *Optimal Control of Distributed Parameter Systems*, Elsevier North Holland, New York, 1981.

6. Franke, D., "Distributed Parameter Systems", *Advances in Control Systems and Signal Processing, Vol. 1*, I. Hartmann, ed., Friedr. Vieweq & Sohn, Wiesbaden, Germany, 1980.

7. Komkov, V., *Optimal Control Theory for Damping of Vibrations of Simple Elastic Systems*, Springer-Verlag, Berlin, 1972.

8. Lions, J. L., "Some Aspects of the Optimal Control of Distributed Parameter Systems", *Society for Industrial and Applied Mathematics*, 1972.

9. Stavroulakis, P., editor, *Distributed System Theory*, Benchmark Papers in Electrical Engineering and Computer Science, Vol. 26, Hutchinson Ross Publ. Co., Stroudsburg, PA., 1983.

10. *Control of Distributed Parameter Systems, 1982*, International Federation of Automatic Control, Pergamon Press, New York, 1983, Proceedings of the IFAC Symposium on the Control of Distributed Parameter Systems.

11. Tzafestas, S. G., and J. M. Nightingale, "Optimal Control of a Class of Linear Stochastic Distributed- Parameter Systems", *Proc. IEE*, Vol. 115, No. 8, August, 1968.

12. Tzafestas, S. G., and J. M. Nightingale, "Differential Dynamic-Programming Approach to Optimal Nonlinear Distributed-Parameter Control Systems", *Proc. IEE*, Vol. 116, No. 6, June, 1969.

13. Tzafestas, S. G., "Optimal Distributed-Parameter Control using Classical Variational Theory", *Int. J. Control*, Vol. 12:593-608, 1970.

14. Tzafestas, S. G., *Distributed Parameter Control Systems: Theory and Applications*, Pergamon Press, Elmsford, New York, 1982.

15. Toda, M., and S. Osaka, "Electromotional Device Using PVF2 Multilayer Bimorph", *Transactions of the IECE of Japan*, Vol. E61, No. 7, July, 1978, pp. 507-512.

16. Toda, M., S. Osaka, and E. O. Johnson, "A New Electromotional Device", *RCA Engineer*, Vol. 25-1, June/July, 1979, pp. 24-27.

17. Tamura, M., T. Yamaguchi, T. Oyaba, and T. Yoshimi, "Electroacoustic Transducers with Piezoelectric High Polymer Films", *Journal of the Audio Engineering Society*, Vol. 23, No. 1, Jan/Feb, 1975, pp. 21-26.

18. Gallantree, H. R., "Ultrasonic Applications of PVDF Transducers", *The Marconi Review*, First Quarter, 1982.

19. Toda, M., "Design of Piezo-electric Polymer Motional Devices with Various Structures", *Transactions of the IECE of Japan*, Vol. E61, No. 7, July, 1978, pp. 513-518.

20. Pearman, G. T., J. L. Hokanson, and T. R. Meeker, "Design and Evaluation of a Contactless Piezoelectric Keyboard using Polyvinylidene Fluoride as the Active Element", *Ferroelectrics*, Vol. 28, 1980, pp. 311-314.

21. Gallantree, H. R., and R. M. Quilliam, "Polarized Poly(Vinylidene Fluoride)-Its Application to Pyroelectric and Piezoelectric Devices", *The Marconi Review*, Fourth Quarter, 1976.

22. "Flexible PVF Film, An Exceptional Polymer for Transducers", *Science*, Vol. 100, No. 23, June, 1978.

23. Lovinger, A. J., "Ferroelectric Polymers", *Science*, Vol. 220, No. 4602, June 10, 1983.

24. Ferroelectrics, Vol. 32, Nos. 1-4, Special Edition on Polyvinylidene Fluoride and Associated Piezoelectric Polymers, 1981.

25. Lang, S. B, "Literature Guide to Piezo- and Pyro-electricity", *Ferroelectrics*, Vol. 45:3-4, 46:1-2, 1981-82.

26. White, F. M., *Fluid Mechanics*, McGraw-Hill Book Company, New York, 1979.

27. Kalmann, R. E., and J. E. Bartram, "Control System Analysis and Design via the 'Second' Method of Lyapunov", *ASME J. of Basic Eng.*, 1960, pp. 371-400.

28. Notes from the Vibration Damping Seminar , University of Dayton Research Institute, June 1983.

29. Crandall, S., N. Dahl, and Lardner, *Introduction to the Mechanics of Solids*, McGraw-Hill Book Company, New York, 1978.

30. Crandall, S., D. Karnopp, E. Kurtz, and D. Pridmore-Brown, *Dynamics of Mechanical and Electromechanical Systems*, McGraw-Hill, New York, 1968.

31. Koehne, M., "Optimal Feedback Control of Flexible Mechanical Systems", *IFAC Symposium on the Control of Distributed Parameter Systems*, 1971.

32. Crandall, S. H., *Engineering Analysis, A Survey of Numerical Procedures*, McGraw-Hill Book Company, New York, 1956.

33. Hildebrand, F. B., *Advanced Calculus for Applications*, Prentice-Hall, Inc., Englewood, New Jersey, 1976.